

ELECTRONIC STRUCTURE OF DISORDERED ALLOYS USING MUFFIN-TIN POTENTIALS

by

SURENDRA SINGH RAJPUT

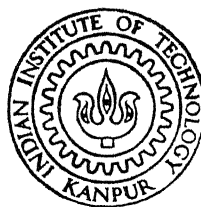
PHY

1990

D

RAJ

ELE



DEPARTMENT OF PHYSICS

INDIAN INSTITUTE OF TECHNOLOGY, KANPUR

July, 1990

ELECTRONIC STRUCTURE OF DISORDERED ALLOYS USING MUFFIN-TIN POTENTIALS

A Thesis Submitted
in Partial Fulfilment of the Requirements
for the Degree of
DOCTOR OF PHILOSOPHY

by
SURENDRA SINGH RAJPUT

to the
DEPARTMENT OF PHYSICS
INDIAN INSTITUTE OF TECHNOLOGY, KANPUR
July, 1990



CERTIFICATE

It is certified that the work contained in the thesis entitled "Electronic Structure of Disordered Alloys Using Muffin-Tin Potentials" by 'Surendra Singh Rajput' has been carried out under my supervision and that this work has not been submitted elsewhere for a degree.

R. Prasad

(R. Prasad)

Thesis Supervisor

July, 1990

DEDICATED TO
MY PARENTS
AND
MY DAUGHTER 'RINKY'

ACKNOWLEDGEMENTS

I am grateful to Dr. R. Prasad for suggesting me the problem and for his valuable guidance throughout the course of my research work.

I express my gratitude to Professor A. Mookerjee and Professor A. Bansil for valuable discussions.

I am thankful to Dr. G. Barua and Dr. N. Chakrabarty for allowing me to test my computer program on their computers.

Thanks are also due to Professor A. K. Majumdar and Dr. V. A. Singh for reading the thesis and helpful suggestions.

I am thankful to Mr. S. S. A. Razee for stimulating discussions and his help in various matters during my stay at I. I. T. Kanpur. I am also thankful to Dr. R. R. Mishra and Dr. A. K. Mishra for their help during my stay at I. I. T. Kanpur. I am also thankful to Mr. R. B. Yadava for his help in the preparation of this thesis.

No words can truly express my feeling of gratitude to my parents. I thank my wife Usha for her patience and understanding.

Surendra Singh Rajput

CONTENTS

	Page
LIST OF TABLES AND CHARTS	vi
LIST OF FIGURES	vii
SYNOPSIS	ix
CHAPTER 1 INTRODUCTION	1
CHAPTER 2 CHARGE SELF-CONSISTENT KKR-CPA AND ITS APPLICATION TO Nb-Mo ALLOYS	12
2.1 Introduction	12
2.2 Korringa-Kohn-Rostoker Coherent- Potential-Approximation (KKR-CPA)	14
2.3 Charge Self-consistent KKR-CPA	20
2.4 Computational Details	22
2.5 Results and Discussion	28
2.6 Conclusions	47
CHAPTER 3 FORMULATION OF KORRINGA-KOHN-ROSTOKER CLUSTER- COHERENT-POTENTIAL-APPROXIMATION (KKR-CCPA)	49
3.1 Introduction	49
3.2 Augmented Space Formalism	51
3.3 Tight-Binding Coherent-Potential- Approximation (TB-CPA)	54
3.4 Tight-Binding Cluster-Coherent-Potential- Approximation (TB-CCPA)	58
3.5 Two-Impurity Problem	63

	Page
3.6 Korrिंगa-Kohn-Rostoker Cluster-Coherent-Potential-Approximation (KKR-CCPA)	64
3.7 Conclusions	70
CHAPTER 4 APPLICATION OF KORRINGA-KOHN-ROSTOKER CLUSTER-COHERENT-POTENTIAL-APPROXIMATION	71
4.1 Introduction	71
4.2 s-Phase Shift Semicircular Model	73
4.3 Bethe Lattice Model	81
4.4 Comparison of KKR-CCPA and TB-CCPA Equations	82
4.5 Results and Discussion	85
4.6 Conclusions	98
CHAPTER 5 SUMMARY AND CONCLUSIONS	99
References	104

LIST OF TABLES AND CHARTS

	Page
Table 2.1 Lattice Constants of Nb-Mo Alloys	22
Table 2.2 Density of States at Fermi Energy for Nb-Mo Alloys	36
Table 4.1 Comparison of KKR-CCPA and TB-CCPA Equations	86
Chart 2.1 Flow Chart of Charge Self-Consistent KKR-CPA	25

LIST OF FIGURES

Figure No.	Caption	Page
2.1	Radial parts of total and valence charge densities ($\equiv r^2 \rho(r)$) vs \sqrt{r} for Nb.	29
2.2	Potential ($\equiv -r v(r)$) vs r for Nb.	30
2.3	Radial parts of total and valence charge densities ($\equiv r^2 \rho(r)$) vs \sqrt{r} for Mo.	31
2.4	Potential ($\equiv -r v(r)$) vs r for Mo.	32
2.5	Averaged density of states by using charge self-consistent KKR-CPA method and obtained by Nb-based rigid band model for Nb_xMo_y alloys.	34
2.6	Density of states at Fermi energy vs concentration of Mo in the Nb_xMo_y alloys.	37
2.7	Density of states using the charge self-consistent KKR-CPA and the density of states reported by using the non-charge self-consistent KKR-CPA for $\text{Nb}_{.50}\text{Mo}_{.50}$ alloy.	39
2.8	Component density of states of Nb and Mo in the $\text{Nb}_{.50}\text{Mo}_{.50}$ alloy.	40
2.9	L-decomposition of component density of states of Nb (in $\text{Nb}_{.25}\text{Mo}_{.75}$ alloy) and pure Nb.	41
2.10	L-decomposition of component density of states of Nb (in $\text{Nb}_{.50}\text{Mo}_{.50}$ alloy) and pure Nb.	42
2.11	L-decomposition of component density of states of Nb (in $\text{Nb}_{.75}\text{Mo}_{.25}$ alloy) and pure Nb.	43

Figure No.	Caption	Page
2.12	L-decomposition of component density of states of Mo (in $\text{Nb}_{.25}\text{Mo}_{.75}$ alloy) and pure Mo.	44
2.13	L-decomposition of component density of states of Mo (in $\text{Nb}_{.50}\text{Mo}_{.50}$ alloy) and pure Mo.	45
2.14	L-decomposition of component density of states of Mo (in $\text{Nb}_{.75}\text{Mo}_{.25}$ alloy) and pure Mo.	46
4.1	Averaged density of states using the CPA and CCPA for the parameters $K=2$, $\delta=1$ and $x=.05$.	88
4.2	(a) Averaged density of states using the CPA and CCPA for parameters $K=2$, $\delta=1$ and $x=0.5$. (b) Local density of states for two impurities pairs embedded in the CPA medium for the same parameters.	89
4.3	Averaged density of states using the CPA and CCPA for parameters $K=2$, $\delta=1.7$ and $x=0.5$.	90
4.4	Averaged density of states using the CPA and CCPA for parameters $K=10$, $\delta=1$ and $x=0.05$.	92
4.5	Same as in figure 4.2 but with parameters $K=10$, $\delta=1$ and $x=0.5$.	93
4.6	Averaged density of states using the CPA and CCPA for parameters $K=2$, $\delta=1.7$ and $x=0.5$.	94
4.7	Change in averaged density of states using the KKR-CPA and KKR-CCPA.	97

SYNOPSIS

ELECTRONIC STRUCTURE OF DISORDERED ALLOYS .
USING MUFFIN-TIN POTENTIALS

By

S. S. RAJPUT

Department of Physics,
Indian Institute of Technology, Kanpur, India

Disordered alloys lack the translational invariance and therefore, the electronic structure of these systems can not be studied by using standard methods of the band theory. However, a great deal of progress in this regard has been made using the coherent potential approximation (CPA) to the realistic muffin-tin potentials. The CPA is a mean field approximation in which the disordered alloy is replaced by an effective medium which is determined by a self-consistent condition. This theory when applied to the muffin-tin model of disordered alloys, is known as Korringa-Kohn-Rostoker coherent-potential-approximation (KKR-CPA). This theory reduces to the standard Korringa-Kohn-Rostoker (KKR) band theory in the perfect crystal limit. The KKR-CPA offers a parameter-free first-principles calculation of the electronic structure of substitutional disordered alloys within the local density approximation of the density functional theory.

In chapter 2, a brief discussion of the KKR-CPA theory using the multiple scattering formalism is presented. The solution of the multiple scattering equations is greatly facilitated by the muffin-tin approximation of the constituent potentials. The charge self-consistent KKR-CPA is then derived using the Green's function approach. This is then applied to study the electronic structure of $\text{Nb}_x\text{Mo}_{1-x}$ alloys for various concentrations ($x = 0.25, 0.50$ and 0.75). Results of the self-consistent potentials, charge densities and density of states are presented and studied as a function of Nb concentration in the alloy. It is seen that the calculation of the density of states is very sensitive to slight changes in the potentials. The density of states at Fermi energy as a function of Mo concentration has been compared with experimental data obtained by the analysis of specific heat data and a good overall agreement is found between the two. The results of the density of states for $\text{Nb}_{.5}\text{Mo}_{.5}$ have been compared with soft x-ray spectra (SXS) curves and a very good agreement has been found between the experimental and fully charge self-consistent KKR-CPA results. Our results of the density of states for $\text{Nb}_{.5}\text{Mo}_{.5}$ have also been compared with earlier non-charge self-consistent KKR-CPA calculations and are found to be quite different in certain energy range. This underlines the importance of full charge self-consistency. We have also found some deviations from Nb-based rigid band model

of Nb-Mo alloy. These deviations decrease with increasing Nb concentration.

The KKR-CPA is a single-site approximation and does not include the correlated scattering from clusters of atoms. This may be important in systems having clustering tendencies and short-range order or in magnetic systems where magnetic moment of an atom is sensitive to the local environment. There have been many attempts to generalize the CPA to include correlated scattering from clusters, but these have been mainly focused on simple tight-binding models. One aim of this work is to achieve this objective using the muffin-tin model. This has been done by using the augmented space formalism of Mookerjee, which guarantees the herglotz properties of the average Green's function. In chapter 3, the augmented space formalism is first applied to the tight-binding Hamiltonian and tight-binding cluster CPA (TB-CCPA) equations are derived. The generalization of the tight-binding method then forms the basis for extension of this method to the KKR framework and KKR cluster CPA (KKR-CCPA) equations are derived. We have also solved the two-impurity problem in the tight-binding framework to explain the structure in the cluster CPA (CCPA) density of states.

In chapter 4, we have applied the KKR-CCPA formulation to the s-phase shift semicircular model, which has an analogue in the tight-binding framework. A one-to-one correspondence has been established between the KKR-CCPA equations for this model

and the TB-CCPA equations for the analogous semicircular model. This is one of the main results of our work. The TB-CCPA formulation is then applied to a Bethe lattice model which in certain limit reduces to the tight-binding semicircular model. We found that the difference in the CPA and CCPA density of states is appreciable only when number of nearest neighbours Z is small and decreases as Z increases. Also in the CPA the minority band is smooth where as in the CCPA it gains structure. The structure in the CCPA density of states is seen at energies close to the impurity levels. This clearly indicates that the structure appears due to the correlated scattering from the clusters embedded in an effective medium. For a large value of Z , there is a little difference in the CPA and CCPA density of states for this model and s-phase shift semicircular model. This is expected because of their equivalence in this limit.

In chapter 5, the main conclusions are summarized. The various shortcomings and limitations of the present work are discussed. Some suggestions for further work in this direction are also given.

CHAPTER-1

INTRODUCTION

Nature has provided us with a rich variety of disordered alloys having diverse electrical, magnetic, transport, optical and superconducting properties, which make them very useful for technological applications. To understand these properties a knowledge of their electronic structure is essential. The disordered alloys lack the translational invariance which is a characteristic of ordered solids. As a result the Bloch's theorem, which greatly simplifies the electronic structure calculation of ordered solids, is inapplicable to these systems. In other words, the standard band theory methods developed for ordered solids can not be applied to disordered alloys.

Substitutional random binary alloys are the simplest kind of disordered systems and will be the main subject of this thesis. In such alloys there exists a lattice structure but each lattice point can be occupied by either of the constituent atoms. Examples of such systems are α -brass Cu-Zn, Cu-Ge, Cu-Pd, Cu-Ni, Cu-Au, Ag-Pd, Nb-Mo etc. Such an alloy will be denoted by A_xB_y , where x and y are concentrations of A and B atoms in the alloy, respectively.

During the last two decades, a great progress has been made in understanding the electronic structure of the

disordered alloys, by the application of coherent potential approximation (CPA)¹⁻³. The CPA is a mean-field approximation, which for the sake of configurational averaging, replaces a disordered alloy $\langle A_x B_y \rangle$ by an ordered solid of effective atoms. These effective atoms are determined by using the self-consistent condition that if an A(B) atom is embedded in this effective medium, the average scattering with respect to the medium is zero i.e.

$$x t_{\mathbf{A}}^{\text{CPA}} + y t_{\mathbf{B}}^{\text{CPA}} = 0 \quad (1.1)$$

where $t_{\mathbf{A(B)}}^{\text{CPA}}$ is atomic scattering operator for an A or B atom embedded in the effective medium. A simpler approximation is average t-matrix approximation (ATA)¹ in which the t-matrix corresponding to the effective atom is

$$t^{\text{ATA}} = x t_{\mathbf{A}} + y t_{\mathbf{B}} \quad (1.2)$$

where $t_{\mathbf{A(B)}}$ is atomic scattering operator for an isolated A(B) atom. Another simple approximation is virtual crystal approximation (VCA)⁴ in which the potential corresponding to the effective atoms is assumed to be

$$v^{\text{VCA}} = x v_{\mathbf{A}} + y v_{\mathbf{B}} \quad (1.3)$$

where $v_{\mathbf{A(B)}}$ is the potential of A(B) atom. This approximation

is good only when the difference between the two constituent potentials is small. Note that all these approximations (CPA, ATA, VCA) are single-site approximations; i.e. they neglect correlated scattering from clusters of atoms. The CPA has been found to be the best single-site approximation for calculation of electronic structure of disordered alloys.

A frequently quoted model in alloy theory is the rigid band model⁵. In this model the potentials of the constituent atoms are assumed to be the same. However, Fermi energy (E_F) is adjusted to give the required number of valence electrons (N^V) per atom in the alloy as

$$N^V = \int_{-\infty}^{E_F} \rho(E) dE \quad (1.4)$$

where $\rho(E)$ is the density of states (DOS) per atom of the host system. The rigid band model is a crude approximation and does not explain many experimental results. But because of its simplicity, it is frequently used as a first step to get an idea of the electronic structure of the alloy.

A solid contains a large number of interacting electrons ($\approx 10^{23}$) interacting with nuclear potentials. Therefore, the calculation of energy levels of such a system is a many-body problem, which can not be solved exactly. However, this problem can be solved to a great degree of accuracy by using the one electron approximation. In this approximation, the many-body problem is reduced to a problem of one electron moving in some

effective potential which is determined self-consistently. Muffin-tin approximation is further used to simplify the calculation of this potential. In this approximation, the potential is assumed to be spherically symmetric within a sphere of radius r_m and constant in the space between this sphere and Wigner-Seitz cell as

$$v(\vec{r}) = \begin{cases} v_{A(B)}(r) & \text{for } r < r_m \\ v_{A(B)}^I & \text{for } r > r_m \end{cases} \quad (1.5)$$

The v^I is a constant interstitial potential as⁶

$$v_{A(B)}^I = 3 \int_{r_m}^{r_{WS}} v(r) r^2 dr / (r_{WS}^3 - r_m^3), \quad (1.6)$$

where $v(r)$ is a spherically symmetric potential which, it is hoped, will be slowly varying in the region between the muffin tin sphere and the Wigner-Seitz sphere of radius r_{WS} . For a pure A(B) solid, $v_{A(B)}^I$ defines muffin-tin zero, i.e. this constant is subtracted from the potential (1.5) making interstitial potential zero. For the alloy, this is calculated as

$$v_{ALLOY}^I = x v_A^I + y v_B^I. \quad (1.7)$$

Note that muffin-tin potentials are non-overlapping. The muffin-tin approximation is a reasonably good approximation for the potential as can be seen by referring to the book by

Moruzzi et al⁷. Using this approximation, they have calculated various properties such as cohesive energy, bulk modulus, density of states and Fermi energy. They got very good agreements with experimental results and were able to explain general trends. Recent experience with alloys shows that the muffin-tin approximation is also a good approximation for metallic alloys^{1-3,8-14}.

The muffin-tin potentials for the constituent atoms are constructed by using the local density approximation (LDA) of the density functional theory¹⁵. The potential can be written as³

$$v_{A(B)}(\vec{r}) = v_{\text{COUL}}^{A(B)}(\vec{r}) + v_{\text{NUC}}^{A(B)}(\vec{r}) + v_{\text{XC}}^{A(B)}(\vec{r}) \quad (1.8)$$

where Coulomb, nuclear and exchange-correlation contributions are

$$v_{\text{COUL}}^{A(B)}(\vec{r}) = \int_{\Omega} d\vec{r}' \frac{\rho_{A(B)}(\vec{r}')}{|\vec{r} - \vec{r}'|} \quad (1.9)$$

$$v_{\text{NUC}}^{A(B)}(\vec{r}) = -e^2 z_{A(B)} / r \quad (1.10)$$

$$v_{\text{XC}}^{A(B)}(\vec{r}) = \frac{\delta E_{\text{XC}}[\rho_{A(B)}(\vec{r})]}{\delta \rho_{A(B)}(\vec{r})} \quad (1.11)$$

where $\rho_{A(B)}$ is the electron charge density in A(B) cell, z is the atomic number and Ω denotes the integral over the Wigner-Seitz unit cell. Here, E_{XC} is the exchange-correlation energy functional which in the local density approximation is

given by¹⁵

$$E_{xc}[\rho] \approx \int \rho(r) \epsilon_{xc}(\rho(\vec{r})) d\vec{r} , \quad (1.12)$$

where $\epsilon_{xc}(\rho)$ is the contribution of exchange and correlation to the total energy (per electron) in a homogeneous but interacting electron gas of density ρ . For paramagnetic case, von Barth-Hedin form of ϵ_{xc} is¹⁶

$$\epsilon_{xc}^B(r_s) = - \frac{0.91633}{r_s} - 0.045 F(r_s/21) , \quad (1.13)$$

where r_s is given by

$$\frac{4\pi}{3} (r_s)^3 = (1/\rho) \quad (1.14)$$

and function

$$F(x) = (1 + x^3) \ln(1 + \frac{1}{x}) - x^2 + \frac{x}{2} - \frac{1}{3} . \quad (1.15)$$

Gunnarsson and Lundqvist form of ϵ_{xc} is¹⁷

$$\epsilon_{xc}^G(r_s) = - \frac{0.458}{r_s} - 0.0333 F(r_s/11.4) . \quad (1.16)$$

Vosko et al. form of ϵ_{xc} for paramagnetic case is¹⁸

$$\begin{aligned} \epsilon_{xc}^V(r_s) = & \frac{-0.91633}{r_s} + A \left[\ln \left[\frac{x^2}{X(x)} \right] + \frac{2b}{Q} \tan^{-1} \left[\frac{Q}{2x+b} \right] \right. \\ & \left. - \frac{b x_o}{X(x_o)} \left[\ln \left[\frac{(x-x_o)^2}{X(x)} \right] + \frac{2(b+2x_o)}{Q} \tan^{-1} \left[\frac{Q}{2x+b} \right] \right] \right] , \end{aligned}$$

where

$$X(x) = x^2 + b x + c, Q = (4c - b^2)^{1/2} \text{ and } x = (r_{\bullet})^{1/2}. \quad (1.17)$$

Here, $A = 0.0621814$, $x_0 = -0.10498$, $b = 3.72744$ and $c = 12.9352$.

It has been seen that use of different exchange-correlation potentials does not give large differences in the calculation of various properties¹⁵. For example differences in cohesive energies in Li, Na, K and Rb were found to be less than 8 mRy¹⁸. Because Moruzzi et al.⁷ have found good agreement between theory and experiment for several metals including Nb and Mo, using von Barth-Hedin form of the exchange-correlation potential, we have used this form in our calculations as will be discussed in chapter 2.

In the last decade, the CPA theory has been very successful as a single-site approximation to calculate the electronic structure of random substitutional disordered alloys. This theory when applied to muffin-tin model of disordered alloys, is known as Korringa-Kohn-Rostoker-CPA (KKR-CPA) theory¹. In the perfect crystal limit, the KKR-CPA theory reduces to the standard KKR band theory¹. In earlier stage of application, potentials v_A and v_B were not determined self-consistently. In the most sophisticated application of the KKR-CPA, v_A and v_B are determined self-consistently within the framework of the local density approximation described in chapter 2. This fully charge self-consistent KKR-CPA theory is a first-principles parameter-free theory of the electronic structure of random alloys.

The KKR-CPA is a single-site approximation and it does not include correlated scattering from clusters of atoms. This could play an important role in systems having short-range order and clustering tendencies¹⁹⁻²¹ such as Cu-Pt and Cu-Pd. There have been many attempts to generalize the CPA to include the correlated scattering from clusters of atoms²²⁻²⁴ but these have been mainly focused on simple tight-binding models. One aim of this work is to achieve this objective using muffin-tin potentials. This has been done by using the augmented space formalism of Mookerjee²³ which preserves the herglotz properties of Green's function. The augmented space formalism has been successfully applied to generalize the CPA theory in the tight-binding framework. Therefore, we first apply the augmented space formalism to the tight-binding Hamiltonian and tight-binding cluster CPA (TB-CCPA) equations are derived. For deriving the KKR cluster CPA (KKR-CCPA) equations we have shown that the Green's function $\langle G_{ij} \rangle$ in the tight-binding framework and the path operator $\langle T_{ij} \rangle$ in the KKR framework are structurally similar. This similarity shows a one-to-one correspondence between the variables of tight-binding framework and the variables of KKR framework as shown in section 3.6. By using this correspondence we have derived the KKR-CCPA equations.

Implementation of the KKR-CCPA to realistic system is difficult due to its complexity and involvement of lengthy computation. So as a test case, we have applied the KKR-CCPA

using two-atom clusters to s-phase shift semicircular model. This model has the following advantages (i) The KKR-CPA theory has been applied to this model in 1970 by Soven²⁵ (ii) The model has an analogue in the tight-binding framework (tight-binding semicircular model). A one-to-one correspondence has been established between the KKR-CCPA equations for s phase shift semicircular model and TB-CCPA equations for the analogous tight-binding semicircular model. This is one of the main results of our work. The tight-binding semicircular model is a limiting case of the Bethe lattice model, for the limit of large number of nearest neighbours. Therefore, the TB-CCPA formulation is applied to the Bethe lattice model and the structure of the CCPA density of states is explained on the basis of clusters of two atoms embedded in the effective medium.

The outline of the thesis is as follows. In chapter 2, we apply the charge self-consistent KKR-CPA to Nb-Mo alloys²⁶. Section 2.1 presents the introduction to this chapter. In section 2.2, we derive the KKR-CPA equation in multiple scattering formalism. In section 2.3, we present the charge self-consistent KKR-CPA method. The Green's function method is used to calculate charge densities of constituent atoms in the alloy. In section 2.4, we present computational details of our calculations. We have chosen von Barth-Hedin exchange correlation potential to calculate the new crystal potentials of constituent atoms in the alloy. Flow chart of the charge

self-consistent KKR-CPA is also presented in this section. The mixing schemes for the CPA and charge self-consistency loop are discussed. In section 2.5, we study the charge self-consistent potentials, charge densities and the density of states as a function of Nb concentration in the Nb_xMo_y alloy for $x=0.25$, 0.50 and 0.75. We find that maximum differences in the Nb(Mo) valence charge density and potential with respect to the pure Nb(Mo) valence charge density and potential, are of the order of 10% and 5% respectively, near the muffin-tin radius. We note that these differences decrease with increasing concentration of Nb(Mo) in the alloy. In this section, we also compare the results of the charge self-consistent KKR-CPA density of states with the density of states using the Nb-based rigid band model and find differences in some energy range. For $\text{Nb}_{.5}\text{Mo}_{.5}$ alloy, we compare the results of component density of states calculated by using the charge self-consistent KKR-CPA method with the results of soft x-ray spectra curves. We find that there is a good agreement between our results and experimental results. We also compare our results with the earlier non-charge self-consistent KKR-CPA calculations. In the final section 2.6, we summarize our main conclusions.

In chapter 3, we present formulation of the CCPA. Section 3.1 gives an introduction to this chapter. In section 3.2, we discuss briefly the augmented space formalism of Mookerjee. In section 3.3, the augmented space formalism has been applied to the tight-binding Hamiltonian and tight-binding CPA (TB-CPA)

equations are derived. In section 3.4, we derive the TB-CCPA equations by application of the augmented space formalism to the tight-binding Hamiltonian. In section 3.5, the two-impurity problem is solved in the tight-binding framework. In section 3.6, the KKR-CCPA equations are derived with the help of the tight-binding CPA (TB-CCPA) equations. Finally in section 3.7, the conclusions are presented.

In chapter 4, we apply the KKR-CCPA and the TB-CCPA formulation to different models. Section 4.1 is an introduction to this chapter. In section 4.2, we discuss the s-phase shift semicircular model in the KKR framework. The path operators and formula for the KKR-CCPA density of states are derived in this section. In section 4.3, we briefly discuss the Bethe lattice model in the tight-binding framework. In section 4.4, the KKR-CCPA equations for the s-phase shift semicircular model and the TB-CCPA equations for the semicircular model are compared and a one-to-one correspondence between them is established (Table-4.1). In section 4.5, we apply the KKR-CPA and the TB-CCPA theories to the s-phase shift model and Bethe lattice model respectively. We also calculate the local density of states by embedding the two-atom cluster in the CPA medium. We give our conclusions in section 4.6.

Finally, in chapter 5 we give the summary of achievements of the present work. Some suggestion for further improvements are given and some remaining problems are mentioned.

CHAPTER-2

CHARGE SELF-CONSISTENT KKR-CPA AND ITS APPLICATION TO Nb-Mo ALLOYS

2.1 INTRODUCTION

The Korringa-Kohn-Rostoker cluster coherent potential approximation (KKR-CPA) theory has been very successful in understanding the electronic structure of disordered alloys. As was mentioned in Chapter 1, it is basically an application of the coherent potential approximation (CPA)¹⁻³ to muffin-tin model of the disordered alloys. In the CPA, one replaces a disordered alloy by an ordered array of effective atoms which are determined by a self-consistent condition. The muffin-tin approximation of the potential plays an important role in simplifying the theory. Because the constituent muffin-tin potentials are spherically symmetric within a certain radius r_m , various quantities such as t-matrices can be expressed in simple forms in the angular momentum space. The non-overlapping nature of the constituent potentials further simplifies the multiple scattering equations to tractable forms.

The KKR-CPA reduces to standard KKR band theory in the perfect crystal limit. Within the local density approximation of the density-functional theory¹⁵⁻¹⁸ (DFT), it can be made fully charge self-consistent. Thus charge self-consistent KKR-CPA provides a first-principles parameter-free theory of

electronic structure of disordered alloys. The theory rests on the same theoretical footing as the band theory of pure metals.

The aim of this chapter is to study the electronic structure of disordered Nb-Mo alloys by the application of the charge self-consistent KKR-CPA²⁶. We have chosen Nb-Mo system because it is one of the important bcc refractory alloy systems. The system has relatively high superconducting transition temperature, high melting point and shows interesting behaviour in several properties such as electronic specific heat²⁷ and thermal expansion coefficient²⁸ as a function of concentration. Also there are many experimental results²⁹⁻³⁴ available on this system. To our knowledge, no fully charge self-consistent KKR-CPA calculation has been reported on this system till now, although some non-charge self-consistent KKR-CPA calculations have been reported^{35,36}. A very interesting behaviour of $\text{Nb}_{.5}\text{Mo}_{.5}$ was noted in these calculations. The density of states below Fermi energy showed approximately the rigid band behaviour, while the density of states above Fermi energy showed large deviation from the results of the rigid band model. This is surprising because this system is regarded as a classic virtual crystal system.

The outline of this chapter is as follows. In section 2.2, the formulation of the KKR-CPA will be briefly discussed. In section 2.3, we present a brief formulation of the charge self-consistent KKR-CPA. In section 2.4, we discuss the application of this theory to Nb-Mo alloys. The computational

details are discussed in this section. In section 2.5, we have studied the charge self-consistent potentials, charge densities and the density of states as a function of Nb concentration in the alloy. Nb-Mo alloys with 25, 50 and 75% of Nb are considered. We compare our results with the results obtained by using Nb-based rigid band model and earlier non-charge self-consistent KKR-CPA calculations. We also compare the density of states with the available experimental data and find good agreement between them. The final section 2.6, gives our main conclusions.

2.2 KORRINGA-KOHN-ROSTOKER COHERENT-POTENTIAL-APPROXIMATION

Consider a disordered substitutional alloy $A_x B_y$ of A and B atoms with concentrations x and y respectively. The one electron potential in the alloy can be written as¹⁻³

$$V(\vec{r}) = \sum_{i=1}^N v_{\alpha}(\vec{r}_i) \quad (2.1)$$

where the vectors \vec{r}_i are defined by $\vec{r}_i = \vec{r} - \vec{R}_i$, \vec{R}_i are the location of the lattice points and N is the total number of sites in the solid. $v_{\alpha}(\vec{r})$ ($\alpha=A, B$) is the potential due to A or B atom and is assumed to be of the muffin-tin form and does not overlap with each other:

$$\begin{aligned}
 v_{\alpha}(\vec{r}_i) &= v_{\alpha}(r_i) , & r_i < r_m \\
 v_{\alpha}(\vec{r}_i) &= \text{constant} , & r_i > r_m .
 \end{aligned}
 \tag{2.2}$$

where r_m is the muffin-tin radius.

The Hamiltonian for a certain configuration of the alloy in atomic mass unit is

$$H = -\nabla^2 + V(\vec{r}) . \tag{2.3}$$

The Green's function in operator notation for a system of scatterers is defined as

$$G = (EI - H)^{-1} , \tag{2.4}$$

where E and I are energy and identity matrix. The equation (2.4) can be expanded using the Dyson's equation as

$$G = G_0 + G_0 T G_0 , \tag{2.5}$$

where G_0 is the free electron Green's function and

$$T = V + V G_0 T \tag{2.6}$$

is the total scattering operator. T may be written as

$$T = \sum_{i,j}^N T_{i,j} , \quad (2.7)$$

where the operators $T_{i,j}$ are called path operators and satisfy the following multiple scattering equation

$$T_{i,j} = t_i \delta_{i,j} + t_i G_0 \sum_{k \neq i} T_{k,j} . \quad (2.8)$$

Here,

$$t_i = v_i (1 + G_0 t_i) \quad (2.9)$$

is the t-matrix that describes the scattering from an isolated potential on the i -th site. Equation (2.9) in angular momentum space has on-the-energy-shell matrix elements as

$$t_{\mathbf{A}(\mathbf{B})}^l(\kappa) = -(\kappa)^{-1} \exp(i\delta_l) \sin(\delta_l) , \quad (2.10)$$

where l is the angular momentum index, $\kappa = (E)^{1/2}$ and δ_l are phase shifts.

The free electron Green's function G_0 in real space can be expressed as²

$$G_0(\vec{r}, \vec{r}') = -i\kappa \sum_{\mathbf{L}} j_l(\kappa r_<) h_l(\kappa r_>) Y_{\mathbf{L}}(\hat{\mathbf{r}}_n) Y_{\mathbf{L}}(\hat{\mathbf{r}}'_m) \delta_{nm} \\ + \sum_{\mathbf{L}\mathbf{L}'} Y_{\mathbf{L}}(\hat{\mathbf{r}}_n) j_l(\kappa r_n) B_{nm}^{\mathbf{L}\mathbf{L}'} j_{l'}(\kappa r'_m) Y_{\mathbf{L}'}(\hat{\mathbf{r}}'_m) , \quad (2.11)$$

where $\vec{r} = \vec{r}_n + \vec{R}_n$, $\vec{r}' = \vec{r}'_m + \vec{R}_m$ and $r_< (r_>)$ is the smaller

(greater) of the variable r_n and r'_m . Also $L = (l, m)$ is a composite index, $Y_L(\hat{x})$ is the real spherical harmonics and j_l and h_l are the spherical Bessel and Hankel functions respectively. The matrix B is defined as

$$B_{nm}^{LL'}(\kappa) = - \left[4\pi i \kappa \sum_{L_1} i^{l-l'-l_1} C_{LL'L_1} Y_{L_1}(\vec{R}_m - \vec{R}_n) \right. \\ \left. \times h_{l_1}^+(\kappa |\vec{R}_n - \vec{R}_m|) \right] (1 - \delta_{nm}), \quad (2.12)$$

where

$$C_{LL'L_1} = \int d\Omega_x Y_L(\hat{x}) Y_{L'}(\hat{x}) Y_{L_1}(\hat{x}) \quad (2.13)$$

and h_l^+ denotes the outgoing Hankel function.

Starting from equation (2.8) and after some algebraic manipulations, on-the-energy-shell matrix elements of the path operator can finally be expressed as

$$T_{nm}^{LL'}(\kappa) = [\{ t^{-1}(\kappa) - B(\kappa) \}^{-1}]_{nm}^{LL'}. \quad (2.14)$$

The Fourier transform of equation (2.12)

$$[B_{\vec{k}}(\kappa)]_{LL'} = (1/N) \sum_{nm} \exp[-i\vec{k} \cdot (\vec{R}_n - \vec{R}_m)] B_{nm}^{LL'}(\kappa) \quad (2.15)$$

is related to the well-known KKR structure functions³⁷. Equations (2.10) and (2.15) are very important in the KKR theory; $t(\kappa)$ depends only on the potential while $B_{\vec{k}}(\kappa)$ depends only on the lattice structure. These two matrices play a central role in the KKR-CPA theory.

Now the Green's function G can be written as²

$$G(E, \vec{r}, \vec{r}') = \sum_{\mathbf{L}, \mathbf{L}'} Z_{\mathbf{L}}^n(E, \vec{r}_n) T_{nm}^{\mathbf{L}\mathbf{L}'}(\kappa) Z_{\mathbf{L}'}^m(E, \vec{r}_m) - \delta_{nm} \sum_{\mathbf{L}} Z_{\mathbf{L}}^n(E, \vec{r}_n) J_{\mathbf{L}}^n(E, \vec{r}_n) , \quad (2.16)$$

where \vec{r} and \vec{r}' are within n th and m th muffin-tin spheres and the wave functions $Z_{\mathbf{L}}^{n(m)}(E, \vec{r}_{n(m)})$ and $J_{\mathbf{L}}^{n(m)}(E, \vec{r}_{n(m)})$ are respectively the regular and irregular solutions of the differential equation

$$\left[-\nabla^2 + v_{n(m)}(\vec{r}_{n(m)}) - E \right] Z_{\mathbf{L}}^{n(m)}(E, \vec{r}_{n(m)}) = 0 . \quad (2.17a)$$

For spherically symmetric potentials one can write

$$\begin{aligned} Z_{\mathbf{L}}^{\mathbf{A}(\mathbf{B})}(E, \vec{r}) &= Y_{\mathbf{L}}(\hat{r}) z_{\mathbf{L}}^{\mathbf{A}(\mathbf{B})}(E, r) \\ J_{\mathbf{L}}^{\mathbf{A}(\mathbf{B})}(E, \vec{r}) &= Y_{\mathbf{L}}(\hat{r}) j_{\mathbf{L}}^{\mathbf{A}(\mathbf{B})}(E, r) . \end{aligned} \quad (2.17b)$$

where $z_{\mathbf{L}}^{\mathbf{A}(\mathbf{B})}$ and $j_{\mathbf{L}}^{\mathbf{A}(\mathbf{B})}$ are radial wave functions and are normalized such that for $r \geq r_m$ they join smoothly to

$$\begin{aligned} z_{\mathbf{L}}^{\mathbf{A}(\mathbf{B})}(\kappa, r) &= j_{\mathbf{L}}(\kappa r) \left[i_{\mathbf{L}}^{\mathbf{A}(\mathbf{B})} \right]^{-1} - \kappa h_{\mathbf{L}}(\kappa r) \\ j_{\mathbf{L}}^{\mathbf{A}(\mathbf{B})}(\kappa, r) &= j_{\mathbf{L}}(\kappa r) . \end{aligned} \quad (2.17c)$$

The regular wave function $z_{\mathbf{L}}^{\mathbf{A}(\mathbf{B})}$ can be written as³⁸

$$z_{\mathbf{L}}^{\mathbf{A}(\mathbf{B})} = \phi_{\mathbf{L}}^{\mathbf{A}(\mathbf{B})}(E) \psi_{\mathbf{L}}^{\mathbf{A}(\mathbf{B})}(r, E) \quad (2.17d)$$

where $\phi_{\mathbf{L}}^{\mathbf{A}(\mathbf{B})}(E)$ is an energy dependent renormalization factor independent of r such that $\psi_{\mathbf{L}}^{\mathbf{A}(\mathbf{B})} \rightarrow r^{\mathbf{L}}$ for $r \rightarrow 0$.³⁸

Equations (2.16) and (2.14) are exact within the muffin-tin approximation and can be used to obtain the Green's function for a cluster of atoms³⁹. However, here we are interested in an infinite system and would like to obtain ensemble average of $G(E, \vec{r}, \vec{r}')$. The ensemble averages of equation (2.16) are related to the ensemble averages of the path operators which will be determined by invoking the CPA. The CPA condition that the average scattering from each site must be zero, can be expressed in terms of Green's function operators as

$$x \langle G \rangle_{\mathbf{A}} + y \langle G \rangle_{\mathbf{B}} = G, \quad (2.18)$$

where $\langle G \rangle_{\mathbf{A(B)}}$ denotes the restricted site average of G when 0-th site is occupied by an $\mathbf{A(B)}$ atom. Equivalently this condition can be written in terms of path operators as

$$x \langle T_{nn} \rangle_{n=\mathbf{A}} + y \langle T_{nn} \rangle_{n=\mathbf{B}} = T_{nn}^{\mathbf{C}}, \quad (2.19)$$

where $\langle T_{nn} \rangle_{n=\mathbf{A}}$ and $\langle T_{nn} \rangle_{n=\mathbf{B}}$ are the restricted site averages of T_{nn} where n th site is occupied by an $\mathbf{A(B)}$ atom and $T_{nn}^{\mathbf{C}}$ is the nn path operator for the CPA medium. After solving equation (2.19), we get the KKR-CPA condition as

$$x [D_{\mathbf{A}}]_{\mathbf{LL}'} + y [D_{\mathbf{B}}]_{\mathbf{LL}'} = I_{\mathbf{LL}'}, \quad (2.20)$$

where

$$[D_{\mathbf{A(B)}}]_{\mathbf{LL}'} = [I + T_{\mathbf{OO}}^{\mathbf{C}} (t_{\mathbf{A(B)}}^{-1} - t_{\mathbf{C}}^{-1})]_{\mathbf{LL}'}^{-1}, \quad (2.21)$$

and \mathbf{c} is used to label quantities for the CPA medium. The path operator matrix is given by

$$[T_{00}^C]_{LL'} = \frac{\Omega}{(2\pi)^3} \int [t_c^{-1}(\mathbf{x}) - B_{\mathbf{k}}^{\dagger}(\mathbf{x})]^{-1}_{LL'} d\mathbf{k}, \quad (2.22)$$

where Ω is the unit cell volume. We note that T_{00}^C involves a complicated Brillouin zone integration. Though $B_{\mathbf{k}}^{\dagger}(\mathbf{x})$ is an off-diagonal matrix, for cubic symmetry the integral reduces to a diagonal matrix³ for $l \leq 2$. By simple manipulations, one can reduce the KKR-CPA equation (2.20) with the help of equation (2.21) to a computationally simpler form as

$$[t_c^{-1}]_{LL'} = \left[x t_A^{-1} + y t_B^{-1} + (t_c^{-1} - t_A^{-1}) T_{00}^C (t_c^{-1} - t_B^{-1}) \right]_{LL'}. \quad (2.23)$$

This equation can be solved only by a numerical iterative method. The input for iterating this equation are t_A^{-1} , t_B^{-1} via equation (2.10) and $B_{\mathbf{k}}^{\dagger}(\mathbf{x})$ via equation (2.15).

2.3 CHARGE SELF-CONSISTENT KKR-CPA

For full charge self-consistency, the charge densities in A and B cells are needed. These can be obtained², once the restricted site averages of the Green's function $\langle G(E, \vec{r}, \vec{r}') \rangle_{A(B)}$ are known, as

$$\rho_{A(B)}(\vec{r}) = -(1/\pi) \int_{-\infty}^{E_F} \text{Im} \langle G(E, \vec{r}, \vec{r}') \rangle_{A(B)} dE, \quad (2.24)$$

where $\rho_{A(B)}$ denotes the charge density associated with an A(B) cell. Equation (2.24) can be further rewritten as

$$\rho_{\mathbf{A}(\mathbf{B})}(\vec{r}) = -(1/\pi) \int_{-\infty}^E \text{Im tr} \left[Z^{\mathbf{A}(\mathbf{B})}(\vec{r}) Z^{\mathbf{A}(\mathbf{B})}(\vec{r}) D_{\mathbf{A}(\mathbf{B})} T_{\text{OO}}^C \right]_{\text{LL}} dE. \quad (2.25)$$

For the charge self-consistent KKR-CPA, the KKR-CPA equation (2.23) is first solved for given potentials of A and B atoms. The new charge densities $\rho_{\mathbf{A}}$ and $\rho_{\mathbf{B}}$ are calculated from equation (2.25). New potentials are then calculated by using the local density approximation of the density-functional theory as has been described in Chapter 1. The new potentials are used to solve the KKR-CPA equation and again a new set of potentials is calculated. We iterate this process until the potentials and charge densities get converged.

To calculate the density of states and component density of states, we define the matrices $F^{\mathbf{A}}$ and $F^{\mathbf{B}}$ as²

$$F_{\text{LL}'}^{\mathbf{A}(\mathbf{B})} = \int_{\Omega} Z_{\text{L}}^{\mathbf{A}(\mathbf{B})}(\vec{r}) Z_{\text{L}'}^{\mathbf{A}(\mathbf{B})}(\vec{r}) d\vec{r}, \quad (2.26)$$

where Ω denotes the integral over the unit cell. Then the component density of states for the A and B atoms can be expressed as

$$\rho_{\mathbf{A}(\mathbf{B})}(E) = -(1/\pi) \text{Im} \int_{\Omega} \langle G(E, \vec{r}, \vec{r}') \rangle_{\mathbf{A}(\mathbf{B})} d\vec{r}$$

or

$$\rho_{\mathbf{A}(\mathbf{B})}(E) = -(1/\pi) \text{Im tr} \left[F^{\mathbf{A}(\mathbf{B})} D_{\mathbf{A}(\mathbf{B})} T_{\text{OO}}^C \right]_{\text{LL}} \quad (2.27)$$

where tr denotes the trace in L space. Since equation (2.27) is diagonal in L space, it allows L decomposed symmetry components (s, p, t_{2g} and e_g) of $\rho_{\mathbf{A}(\mathbf{B})}(E)$ in the alloy. The cubic symmetry

reduces the number of distinct elements four i.e. s, p, t_{2g} and e_g . The average density of states for the alloy is calculated as

$$\rho(E) = -(1/\pi) \text{Im tr} \left[\{ x F^A D_A + y F^B D_B \} T_{00}^C \right]_{LL} . \quad (2.28)$$

2.4 COMPUTATIONAL DETAILS

We have applied the charge self-consistent KKR-CPA method to the Nb_xMo_y alloy for different concentrations of Nb ($x=0.25$, 0.50 and 0.75). These alloys have bcc structure and their lattice constants are presented⁴⁰ in Table 2.1. This systems forms a continuous solid solution in the whole concentration range.

TABLE 2.1
Lattice constants of Nb_xMo_y alloys.

S.No.	Nb concentration (x) ($y=1-x$)	Lattice constants(a.u.)
1	0.00	5.940
2	0.25	6.015
3	0.50	6.054
4	0.75	6.155
5	1.00	6.230

For the charge self-consistent KKR-CPA, we start with atomic charge densities $(\rho_{\mathbf{A}}^{\text{in}}, \rho_{\mathbf{B}}^{\text{in}})$ for Nb and Mo, and calculate the potentials $(v_{\mathbf{A}}^{\text{in}}, v_{\mathbf{B}}^{\text{in}})$ from equation (1.8) as explained in chapter 1. The $t_{\mathbf{A}}^{-1}(\kappa)$ and $t_{\mathbf{B}}^{-1}(\kappa)$ are then computed for the input potentials $(v_{\mathbf{A}}^{\text{in}}, v_{\mathbf{B}}^{\text{in}})$. The KKR-CPA equation is solved iteratively within a tolerance of 0.0001, to calculate the $t_{\mathbf{C}}^{-1}$. Note that in each KKR-CPA iteration, $T_{\infty}^{\mathbf{C}}$ has to be calculated using equation (2.22), which involves a complicated Brillouin zone integration. In the initial stages of implementation of the KKR-CPA theory, this was a major problem, which was eventually solved by using the special direction technique⁴¹. Although this technique is quite simple, it does not give as accurate results as tetrahedron technique which has been developed by Kaprzyk et al.⁴² for disordered alloys. Since, higher accuracy is essential for full charge self-consistency, we have used the tetrahedron method using 858 \vec{k} points in the irreducible part of the Brillouin zone. We have observed that it is difficult to achieve convergence if we use less number of \vec{k} points in the tetrahedron. The new charge densities $(\rho_{\mathbf{A}}^{\text{out}}, \rho_{\mathbf{B}}^{\text{out}})$ are obtained by equation (2.25). The new potentials $(v_{\mathbf{A}}^{\text{out}}, v_{\mathbf{B}}^{\text{out}})$ in the alloy are then calculated using equation (1.8) of chapter 1. Again, these new potentials are taken as input to repeat the whole process, until the difference of old and new charge densities is within a certain tolerance $(\varepsilon_{\text{CHARGE}})$. This tolerance has been defined as

$$\varepsilon_{\text{CHARGE}}^{\mathbf{A}(\mathbf{B})} = \int_0^{r_m} (\rho_{\mathbf{A}(\mathbf{B})}^{\text{out}} - \rho_{\mathbf{A}(\mathbf{B})}^{\text{in}}) r^2 dr . \quad (2.29)$$

This tolerance is taken to be 0.0001 . The flow chart of the charge self-consistent KKR-CPA has been given in Chart 2.1.

For the new charge densities, we have to calculate Fermi energy, as can be seen from equation (2.25). The Fermi energy is calculated using Lloyd formula for integrated density of states. The Lloyd formula¹ is written as

$$\begin{aligned} N^{\mathbf{I}}(E) = N_{\mathbf{O}}^{\mathbf{I}}(E) + \frac{2}{\pi} \text{Im} \left[x \ln \det | t_{\mathbf{C}}^{-1} - t_{\mathbf{B}}^{-1} | + y \ln \det | t_{\mathbf{C}}^{-1} - t_{\mathbf{A}}^{-1} | \right] \\ - \frac{2}{\pi N} \text{Im} \sum_{\vec{k}} \ln \det | t_{\mathbf{C}}^{-1} - B_{\vec{k}} | . \end{aligned} \quad (2.30)$$

where $N^{\mathbf{I}}(E)$ is the integrated density of states and $N_{\mathbf{O}}^{\mathbf{I}}(E)$ is the free electron integrated density of states. Though this formula is easy to handle, it sometimes gives unphysical jumps which can occur in \ln (logarithm) of a complex quantity, used in the formula. Kaprzyk and Bansil³⁸ have derived a generalized Lloyd formula which does not give such unphysical jump and is given below:

$$\begin{aligned} N^{\mathbf{I}}(E) = (\text{Im}/\pi) \text{tr} \left[\frac{1}{N} \sum_{\vec{k}} \ln [G_{\mathbf{O}}^{-1}(E, \vec{k}) + \beta^{\mathbf{J}} - \beta^{\mathbf{C}}]^{-1} - \ln (G_{\mathbf{C}}) \right. \\ \left. + x \ln [(\psi^{\mathbf{A}}(r_m))^{-1} G_{\mathbf{A}}] + y \ln [(\psi^{\mathbf{B}}(r_m))^{-1} G_{\mathbf{B}}] \right] , \end{aligned} \quad (2.31)$$

FLOW CHART OF CHARGE SELF-CONSISTENT KKR-CPA

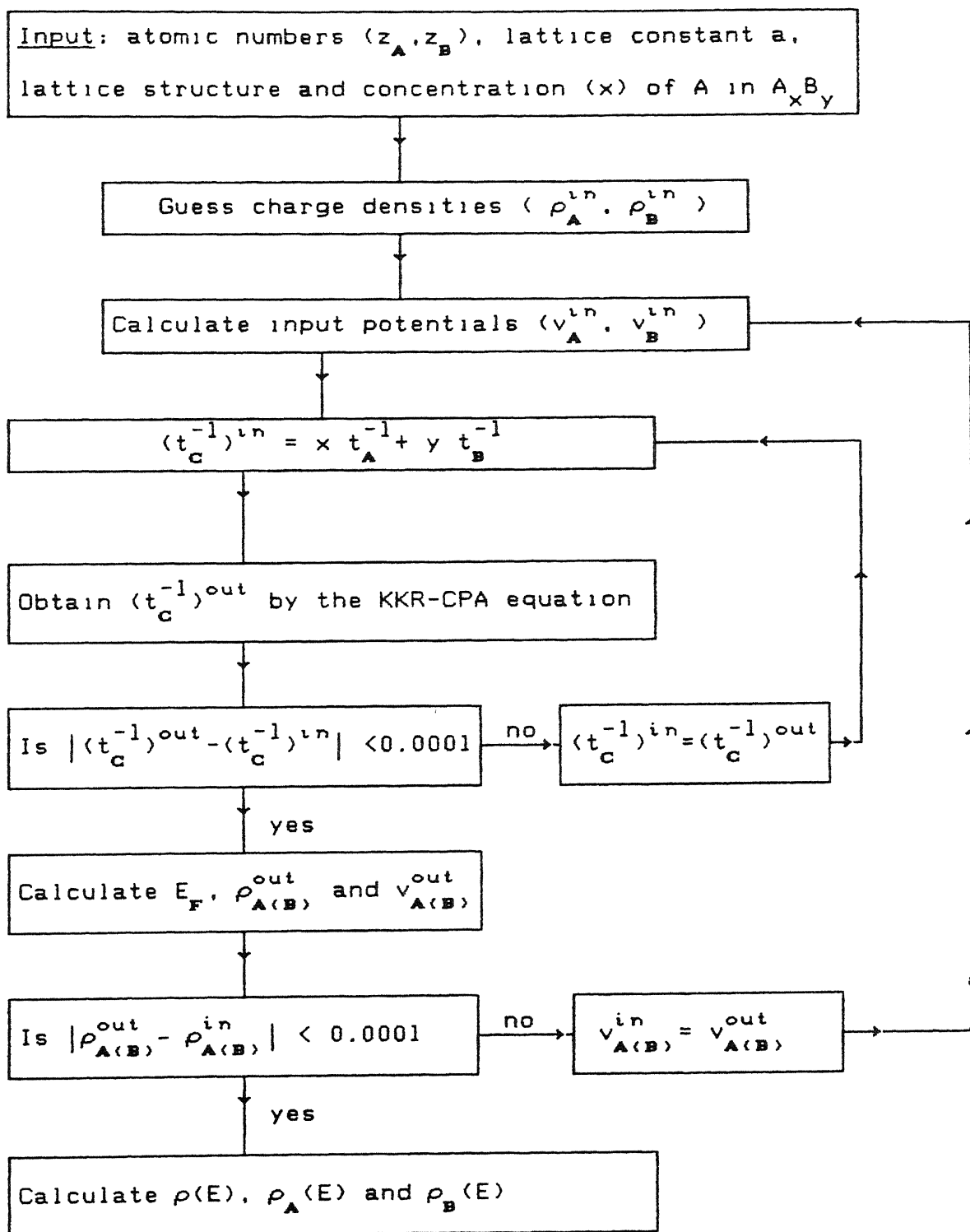


CHART 2.1

where

$$G_{A(B)} = [G_C^{-1} + \beta^C - \beta^{A(B)}]^{-1}. \quad (2.32)$$

Here, the KKR-CPA Green's function G_C and the associated log-derivative β^C are the self-consistent solutions of the CPA equation (2.18):

$$x G_A + y G_B = G_C, \quad (2.33)$$

where

$$G_C = \frac{1}{N} \sum_{\vec{k}} [G_0^{-1}(E, \vec{k}) + \beta^j - \beta^C]^{-1}, \quad (2.34)$$

$$\beta_l^{A(B)}(E) = r^2 \frac{\partial}{\partial r} \ln z_l^{A(B)}(E, r) \Big|_{r=r_m} \quad (2.35)$$

and β_l^j is the log-derivative for the spherical Bessel function. Note that $\psi_l^{A(B)}(r)$ and $z_l^{A(B)}(r)$ have been already defined in equations (2.17).

Although equation (2.31) also contains the logarithm functions, but unphysical jumps of these functions cancel with each other. The integrated density of states at the Fermi energy gives the total number of valence electrons in the alloy. Therefore, the Lloyd formula permits an evaluation of the Fermi energy without requiring an explicit computation of the density of states. We have used formula of Kaprzyk and Bansil, equation (2.31), to calculate the Fermi energy.

The calculation of charge densities from equation (2.25) using integration along real energy is very slow and time consuming. To speed up the calculations, the complex energy method^{43,44} has been used to calculate the charge densities and potentials. The \vec{k} -space integration is much faster in the complex plane because the integrand becomes smoother when the energy is complex.

To obtain full charge self-consistency it takes a large number of iterations to achieve convergence. Therefore, to facilitate both the CPA and charge self-consistency loops, we have used mixing schemes^{7,45}. In the CPA loop new t_c^{-1} is taken as

$$\begin{aligned} \left[(t_c^{-1})^{in} \right]_{ITCPA+1} = \alpha_{CPA} \left[(t_c^{-1})^{in} \right]_{ITCPA} \\ + (1-\alpha_{CPA}) \left[(t_c^{-1})^{out} \right]_{ITCPA} , \end{aligned} \quad (2.36)$$

where α_{CPA} is the mixing parameter for the CPA and $ITCPA$ is the number of iterations. In the charge self-consistency loop, the new potential is taken as

$$\begin{aligned} \left[v_{A(B)}^{in} \right]_{ITCHARGE+1} = \alpha_{A(B)}^v \left[v_{A(B)}^{in} \right]_{ITCHARGE} \\ + (1-\alpha_{A(B)}^v) \left[v_{(B)}^{out} \right]_{ITCHARGE} , \end{aligned} \quad (2.37)$$

where $\alpha_{A(B)}^v$ is the mixing parameter for $A(B)$ potential and

ITCHARGE is the number of iteration in charge density loop. We have taken $\alpha_{A(B)}^V$, between 0.90 to 0.98 for all concentrations of Nb in the alloy. The CPA mixing α_{CPA} is taken as 0.05.

The CPU time on HP-9000/850 system for running single charge self-consistency loop, is about 10 hours. The required number of iterations for the convergence of the charge densities in the charge self-consistency loop is about 25 for all concentrations of Nb in the Nb-Mo alloys. The final calculation of density of states and component density of states is done along the real energy axis and takes about another 15 hours of CPU time on this machine.

2.5 RESULTS AND DISCUSSION

Figure 2.1(a) shows the radial parts of the total and valence charge densities of pure Nb in good agreement with the calculations of Moruzzi et al.⁷. Note that there is slight difference in the value of the lattice constant used in the two calculations. We get excellent agreement with their calculation if we take the same value of the lattice constant. Figures 2.1(b), (c) and (d) show changes in the valence charge densities of Nb in the alloy with respect to pure Nb valence charge density for $x=0.25$, 0.50 and 0.75 respectively. As expected the maximum difference (of the order of 10% near muffin-tin radius) occurs for $x=0.25$, which decreases with the increase in x .

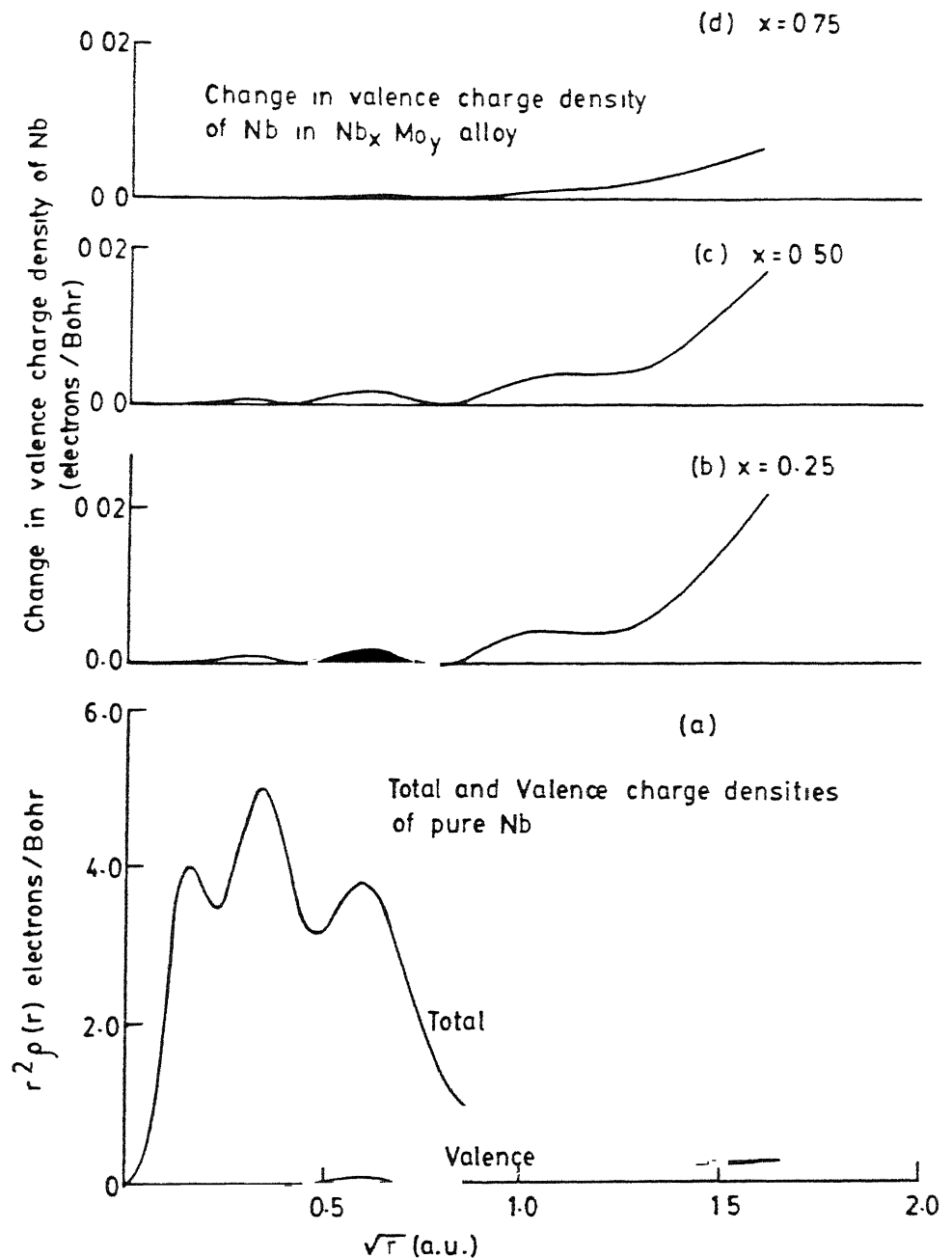


Figure-2.1 (a) The radial parts of total and valence charge densities ($\equiv r^2 \rho(r)$) vs \sqrt{r} for pure Nb. Figures (b), (c) and (d) show changes in the Nb valence charge density in the Nb_xMo_y alloys with respect to the pure Nb valence charge density for $x=0.25$, 0.50 and 0.75 respectively. ($y = 1-x$)

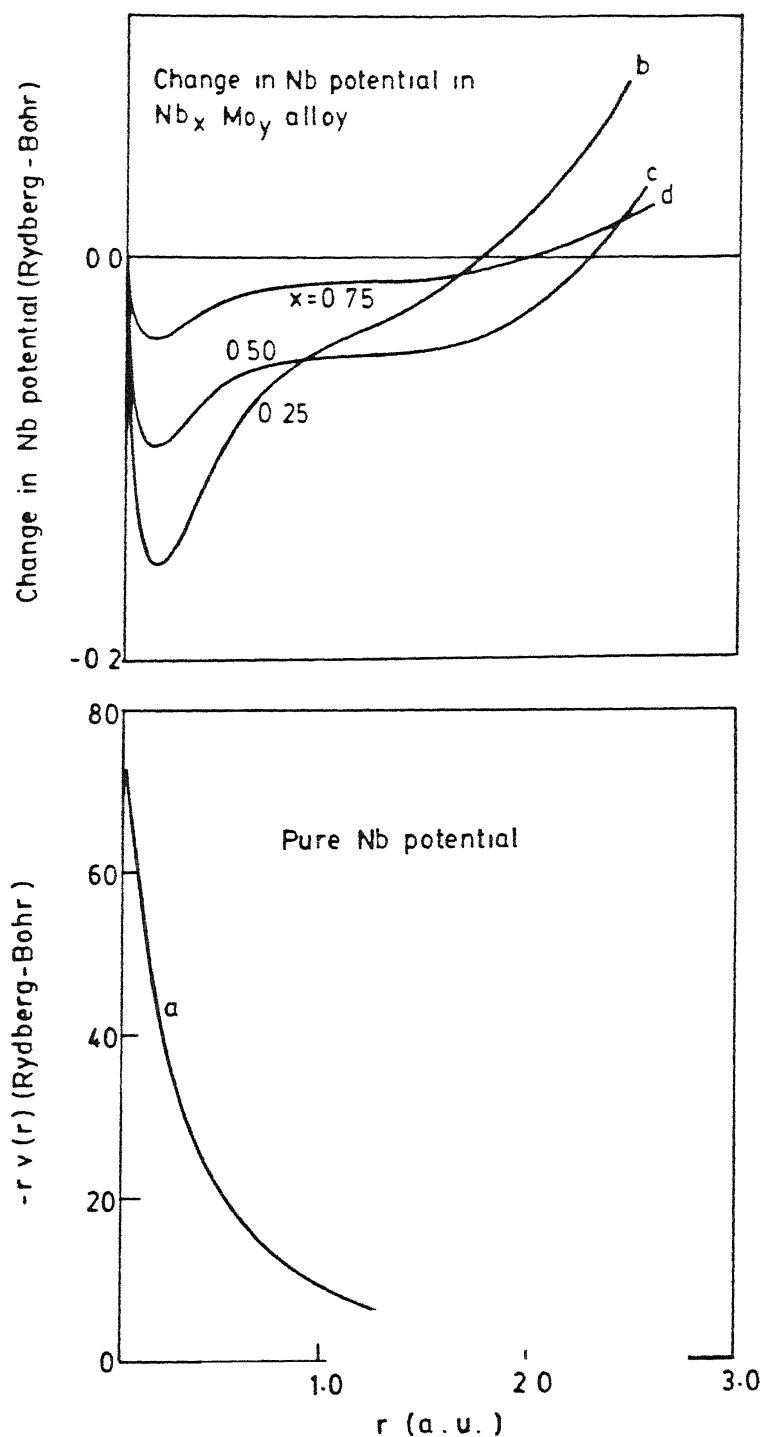


Figure-2.2 (a) The potential ($\equiv -r v(r)$) vs radial distance r for pure Nb. Figures (b), (c) and (d) show changes in the Nb potential in the $Nb_x Mo_y$ alloys with respect to the pure Nb potential for $x = 0.25$, 0.50 and 0.75 respectively. ($y = 1 - x$)

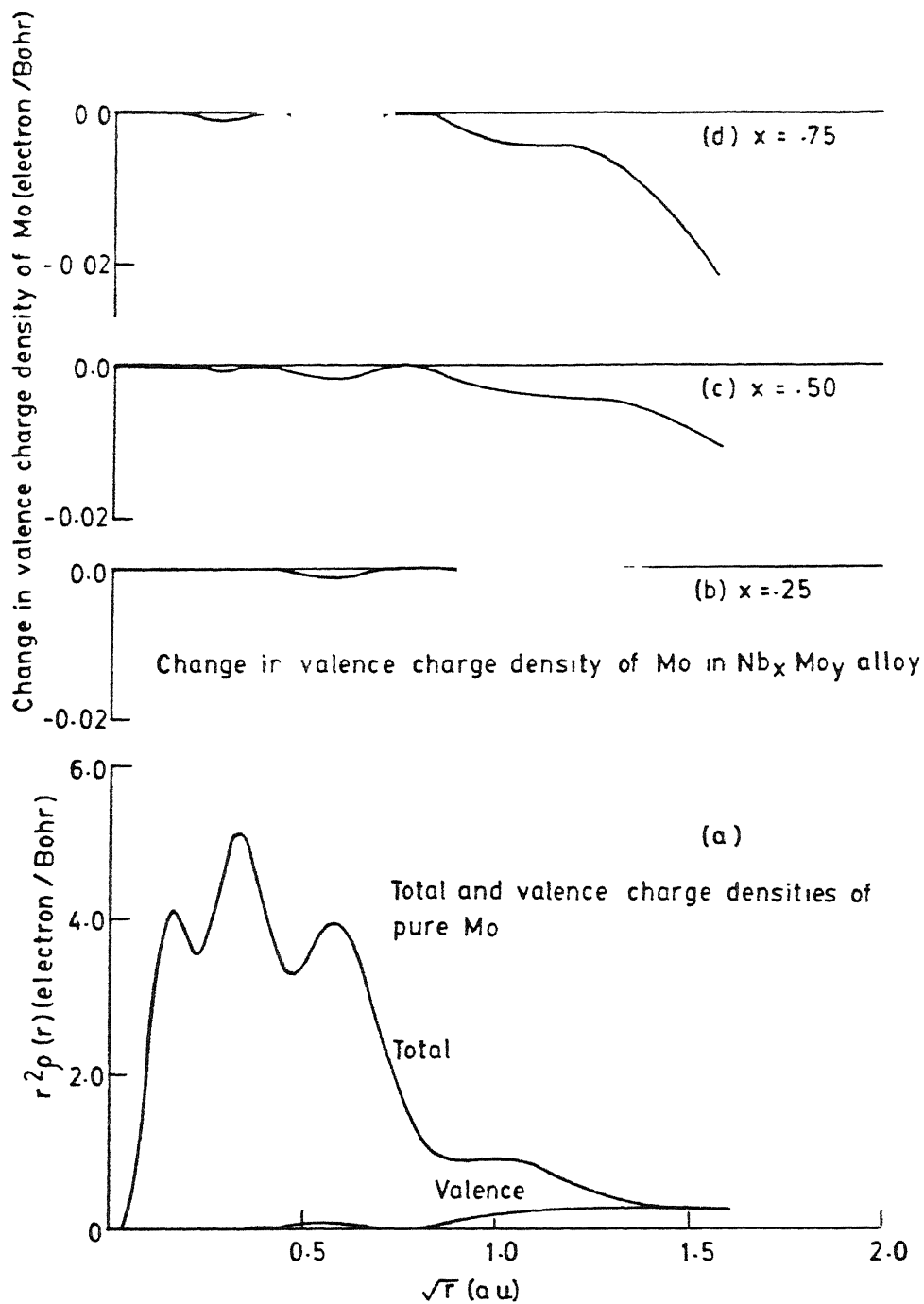


Figure-2.3 (a) The radial parts of total and valence charge densities ($\equiv r^2 \rho(r)$) vs \sqrt{r} for pure Mo. Figures (b), (c) and (d) show changes in the Mo valence charge density in the Nb_xMo_y alloys with respect to the pure Mo valence charge density for $x=0.25$, 0.50 and 0.75 respectively. ($y=1-x$)

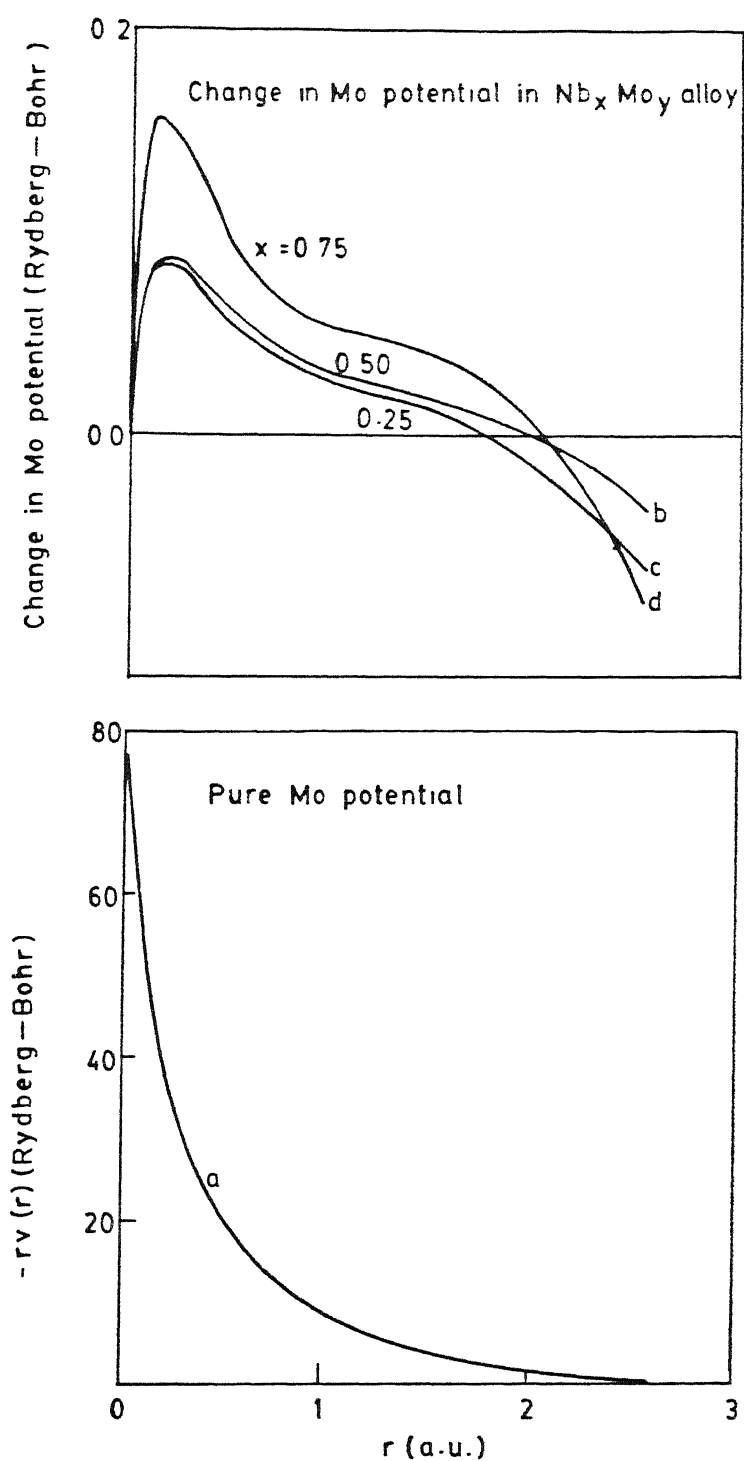


Figure-2.4 (a) The potential ($\equiv -r v(r)$) vs radial distance r for pure Mo. Figures (b), (c) and (d) show changes in the Mo potential in the $Nb_x Mo_y$ alloys with respect to the pure Mo potential for $x = 0.25$, 0.50 and 0.75 respectively. ($y = 1 - x$)

Figure 2.2(a) shows the self-consistent muffin-tin potential of pure Nb used in our calculation. Figures 2.2(b), (c) and (d) show changes in the self-consistent Nb potentials in the alloy with respect to the pure Nb potential for $x=0.25$, 0.5 and 0.75. This difference is maximum for $x=0.25$ and is of the order of 5% near the muffin-tin radius and it decreases with the increase in concentration x .

Figure 2.3(a) shows the radial parts of the total and valence charge densities of pure Mo in good agreement with the calculation of Moruzzi et al.⁷. Figures 2.3(b), (c) and (d) show how the Mo valence charge density changes in the alloy as a function of Nb concentration. The maximum change which is of the order of 10% near the muffin-tin radius is observed for $x=0.75$, as is expected. This change decreases with increase in the concentration of Mo in the alloy.

Figure 2.4(a) shows the muffin-tin potential of pure Mo. Figures 2.4(b), (c) and (d) show how the Mo potential in the alloy changes as a function of Nb concentration. The maximum change which is of the order of 5% near the muffin-tin radius occurs for $x=0.75$. This change decreases with the increase in the concentration of Mo (y) in the alloy. Thus, we find that the maximum difference in the valence charge densities of Nb and Mo in the alloy with respect to the pure Nb and Mo values, are of the order of 10% near the muffin-tin radius. The maximum difference in the potentials of Nb and Mo in the alloy with respect to the potentials of pure Nb and Mo, are of the order

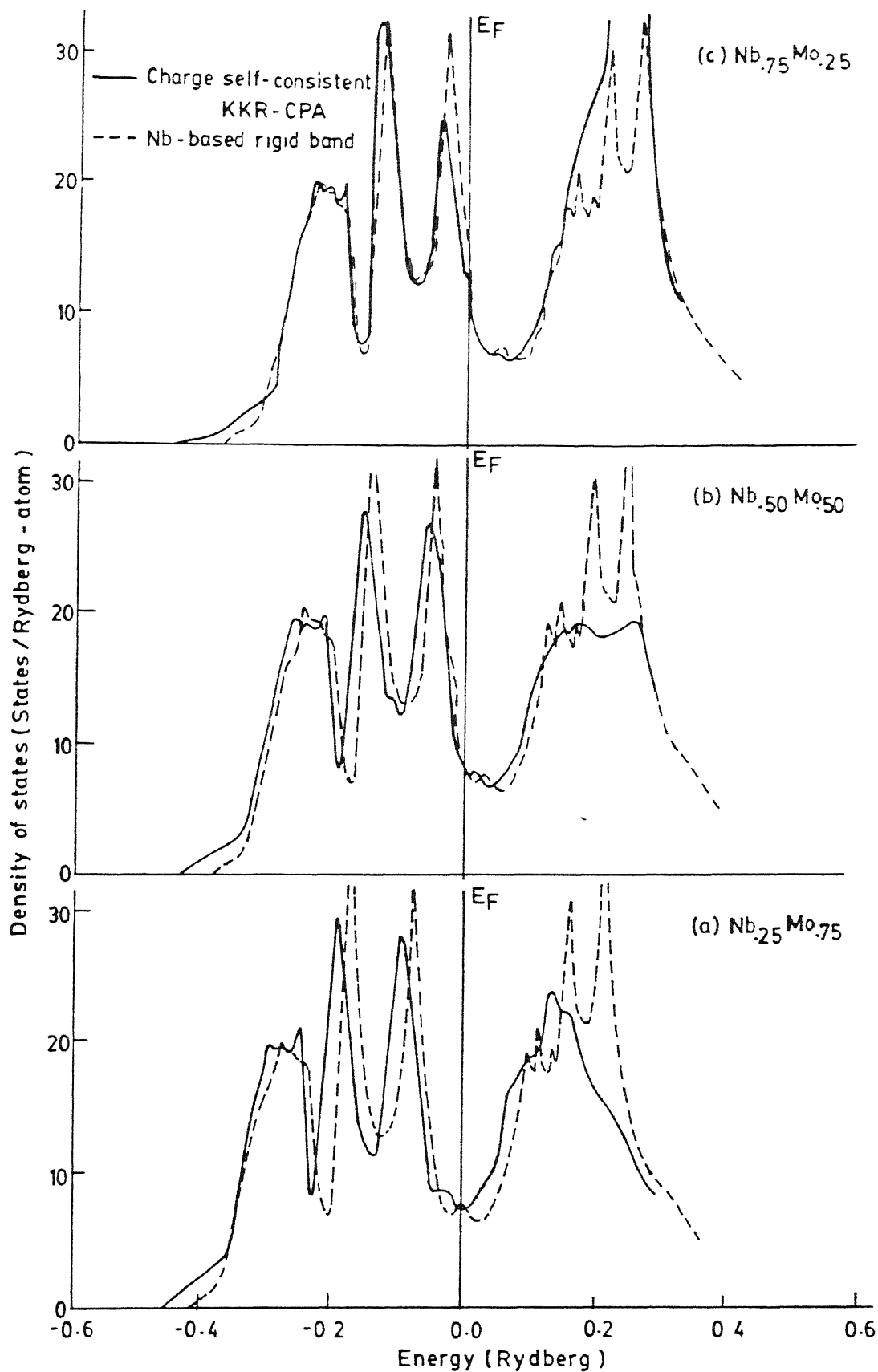


Figure-2.5 The average density of states by using the charge self-consistent KKR-CPA (full curves) and the density of states obtained by Nb-based rigid band model (broken curves) for the Nb_xMo_y alloys for (a) $x=0.25$, (b) $x=0.50$ and (c) $x=0.75$. The energy is measured with respect to the Fermi energy. ($y=1-x$)

of 5% near the muffin-tin radius. Also, we find that, these differences for Nb (or Mo) decrease with the increase in the concentrations of Nb (or Mo) in the alloy. We also find that charge transfer from Mo to Nb, is of the order of 1%.

Figures 2.5(a), (b) and (c) show the comparison of the average density of states (DOS) calculated using the charge self-consistent KKR-CPA, with those of Nb-based rigid band model for $x=0.25$, 0.50 and 0.75 respectively. We find that below the Fermi energy, there is no qualitative difference between the two results for all concentrations. However, there is a shift in the charge self-consistent KKR-CPA density of states towards the lower energy region with respect to the Nb-based rigid band density of states. This shift of density of states decreases with the increase in the concentration of Nb in the alloy. In the region above the Fermi energy, there is a marked difference between the charge self-consistent KKR-CPA density of states and the Nb-based rigid band density of states for all concentrations. This has also been observed by Giuliano et al.³⁵ when they compared their non-charge self-consistent KKR-CPA calculation with the results of the rigid band model. However, the deviation from Nb-based rigid band density of states is less in our calculations.

Table 2.2 gives the Fermi energies (E_F) for various alloy compositions and alloy density of states (DOS) at the Fermi energies calculated within the charge self-consistent KKR-CPA (present calculations) and non-charge self-consistent KKR-CPA

methods^{36,40}. We see that the Fermi energies and the density of states at E_F in the two calculations are not very different. However, we shall see below that the full density of states curves show substantial difference in the two calculations.

TABLE 2.2

Density of states (DOS) at Fermi energy (E_F) for Nb_xMo_y alloys.

S.No.	x ($y=1-x$)	Present calculations		Results of ref 40	
		E_F (Ry)	DOS at E_F St/(Ry.atom)	E_F (Ry)	DOS at E_F St/(Ry.atom)
1	0.00	0.8114	8.9	0.826	10.7
2	0.25	0.7650	7.1	0.764	8.6
3	0.50	0.7483	7.8	0.749	9.6
4	0.75	0.7052	11.4	0.709	14.8
5	1.00	0.6880	19.2	0.682	19.5

Figure 2.6 shows comparison of the density of states (DOS) at Fermi energies. The two theoretical curves are quite similar. These results are compared with experimental results²⁷ obtained

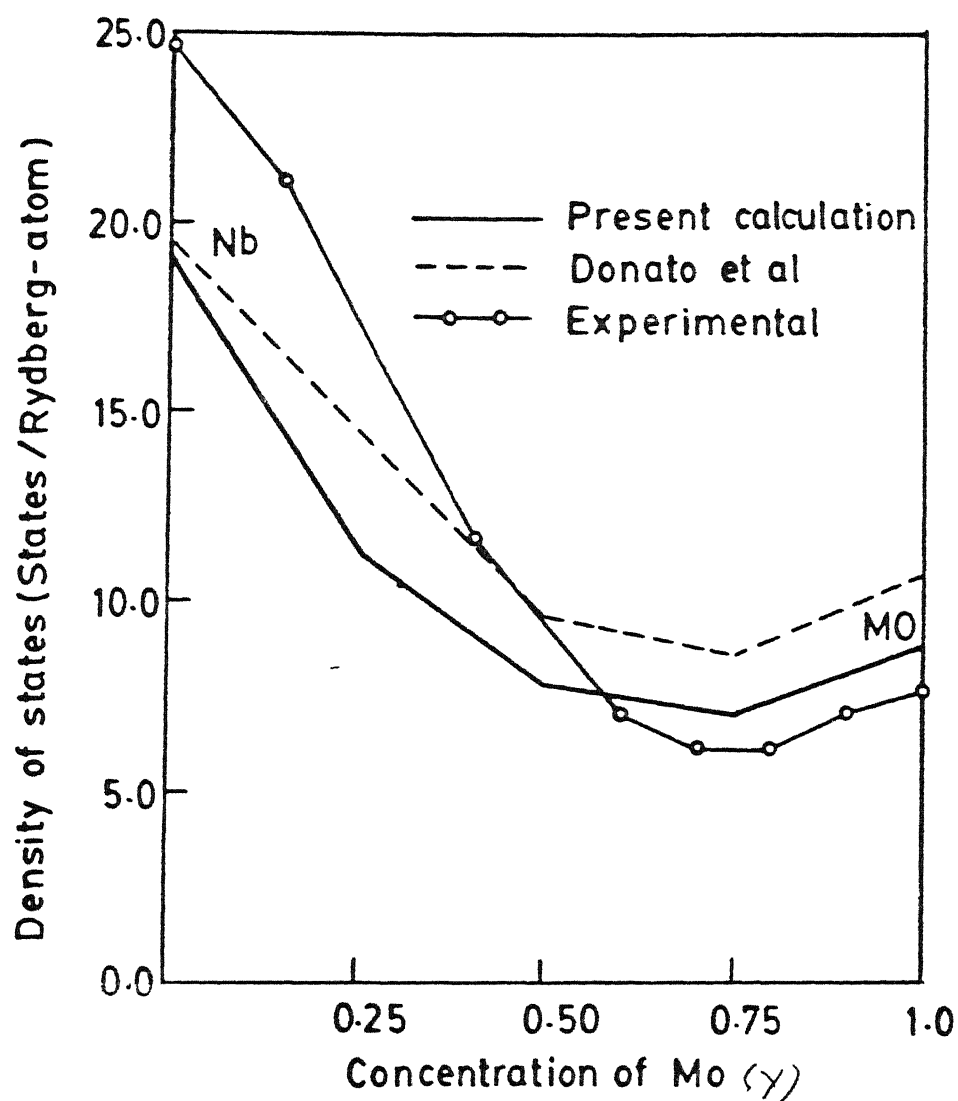


Figure-2.6 Density of states at Fermi energy vs concentration of Mo in the Nb_xMo_y alloys: present results (full curve), results of reference (40) (broken curve) and experimental results of reference (27) (solid curve with circles). ($\gamma = 1 - X$)

by the analysis of the specific heat data. Our theoretical results are in good agreement with the experimental results and show the correct trend as a function of Mo concentration.

Figures 2.7(a) and (b) show comparison of the charge self-consistent KKR-CPA density of states with two different non-charge self-consistent KKR-CPA results^{35,36} for $x=0.50$. The results of references 35 and 36 are different due to their different choice of input potentials for Nb and Mo. There are large differences between our results and the previous calculations. Though the potential differences of the Nb and Mo in the alloy with respect to the pure Nb and Mo potentials are small, yet there is substantial difference in the results of charge self-consistent and non-charge self-consistent calculations. This implies that the density of states is very sensitive to the changes in the potentials. These facts underline the importance of full charge self-consistency.

In figures 2.8(a) and (b), we show the comparison of our calculated component density of states for Nb and Mo with soft x-ray (emission and absorption) spectra curves³⁶ and non-charge self-consistent results of Donato et al.³⁶ for $x=0.50$. Above the Fermi energy, our results are very close to the results of Donato et al.. But there are some differences below the Fermi energy. Our results are in better agreement with the experimental results.

Figures 2.9(a, b, c, d, e), 2.10(a, b, c, d, e) and 2.11(a, b, c, d, e) show the comparisons of s, p, t_{2g} , e_g and

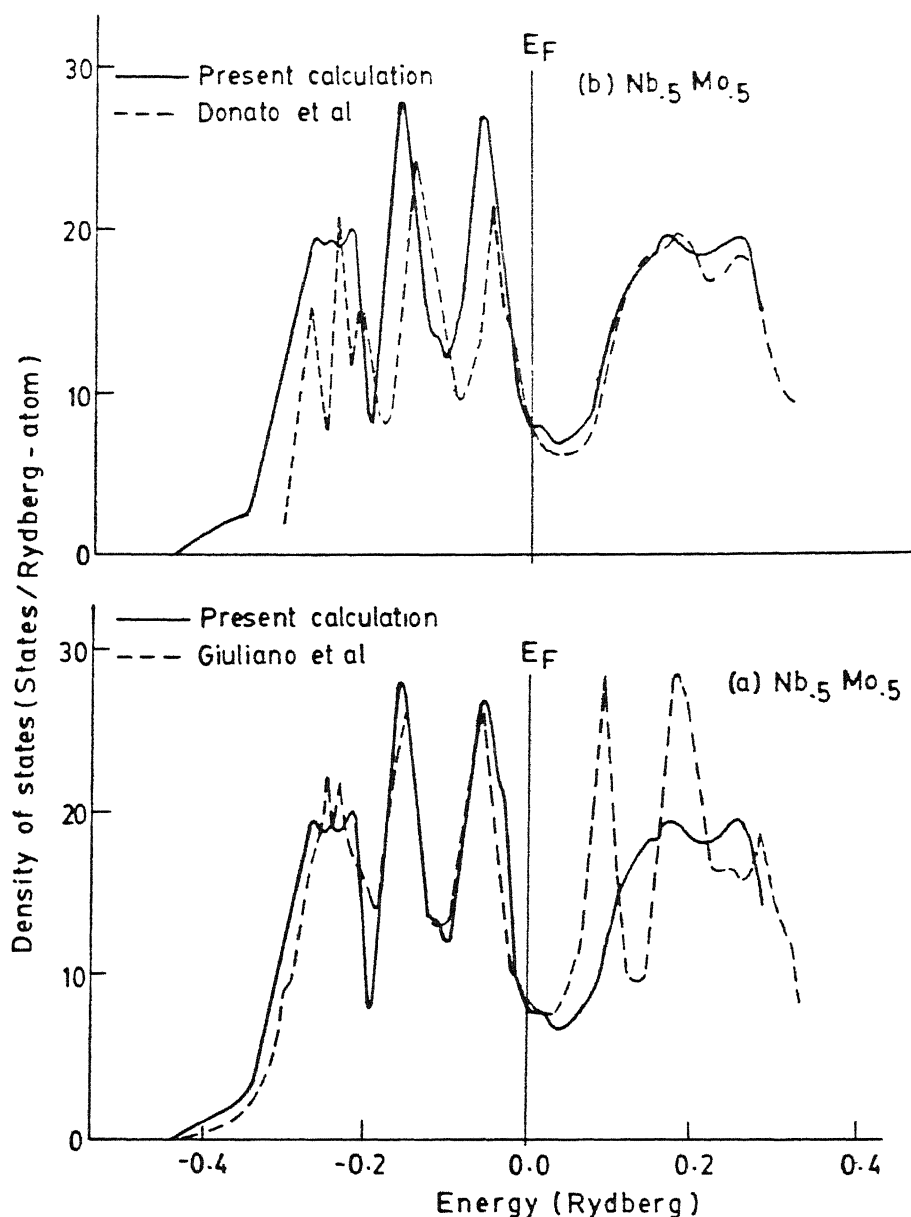


Figure-2.7 The density of states, using the charge self-consistent KKR-CPA (full curve) and the density of states reported by using the non-charge self-consistent KKR-CPA (broken curve), (a) from reference (35) and (b) from reference (36) for $\text{Nb}_{0.5}\text{Mo}_{0.5}$ alloy. The energy is measured with respect to the Fermi energy.

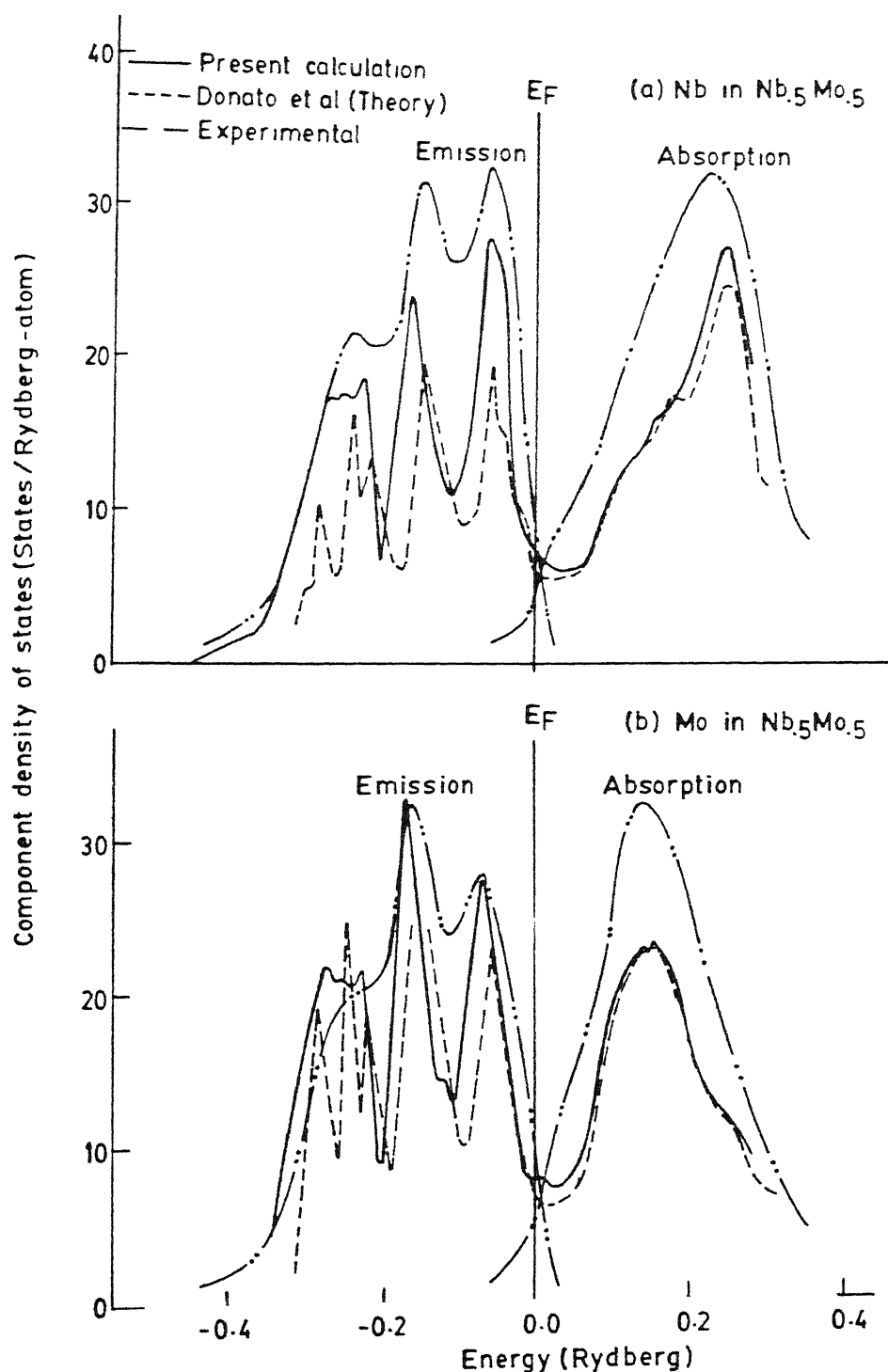


Figure-2.8 (a) The component density of states of Nb and (b) the component density of states of Mo in the $\text{Nb}_{50}\text{Mo}_{50}$ alloy: present calculation (full curve), earlier non-charge self-consistent calculation of reference (36) (dashed curve) and experimental results of reference (36) (dashed-dot curve). The energy is measured with respect to the Fermi energy.

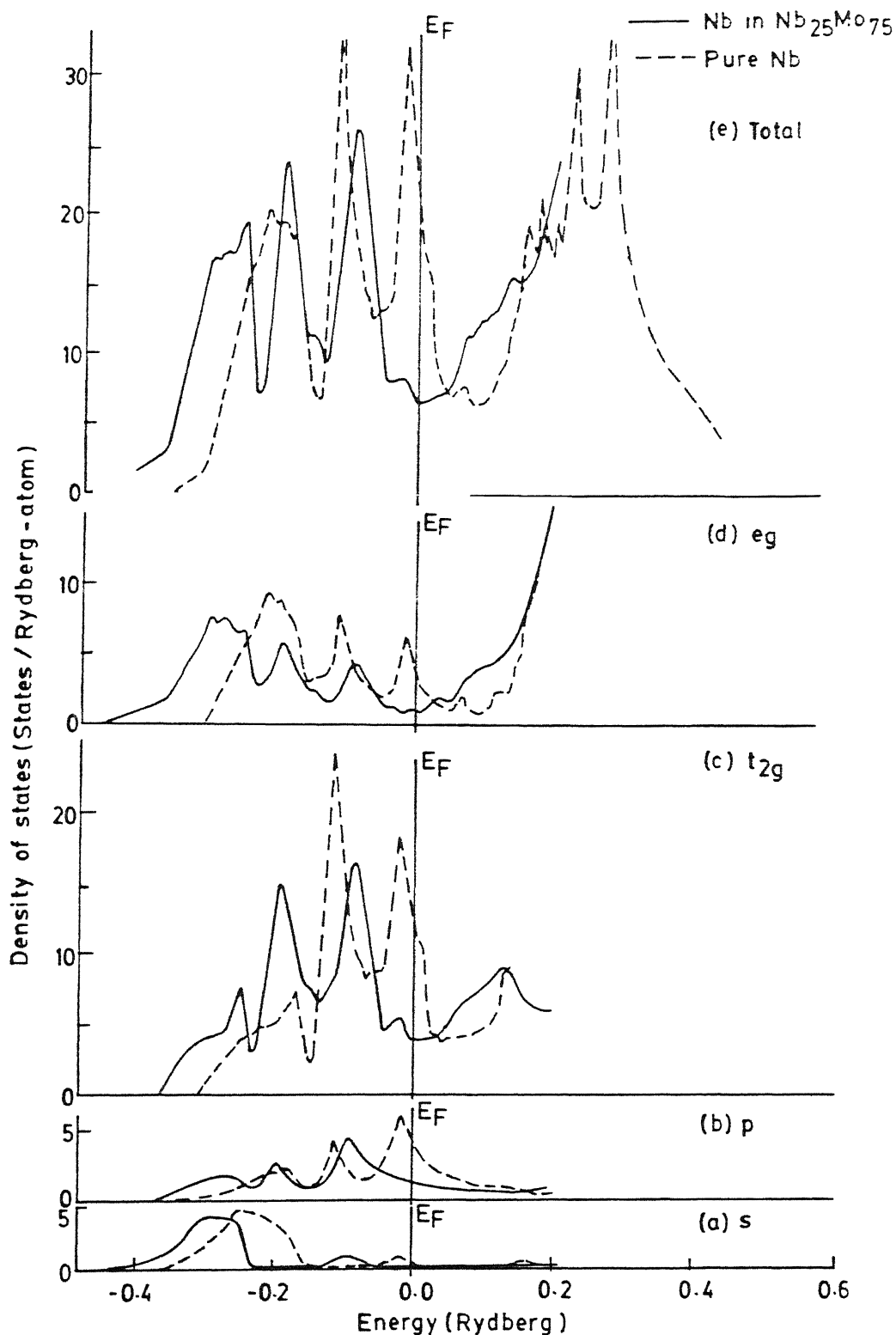


Figure-2.9 L-decomposition of the component density of states of Nb in the $\text{Nb}_{25}\text{Mo}_{75}$ alloy (full curves) and pure Nb (broken curves). The s, p, t_{2g} , e_g and total components are shown in figures (a), (b), (c), (d) and (e) respectively. The energy is measured with respect to the Fermi energy.

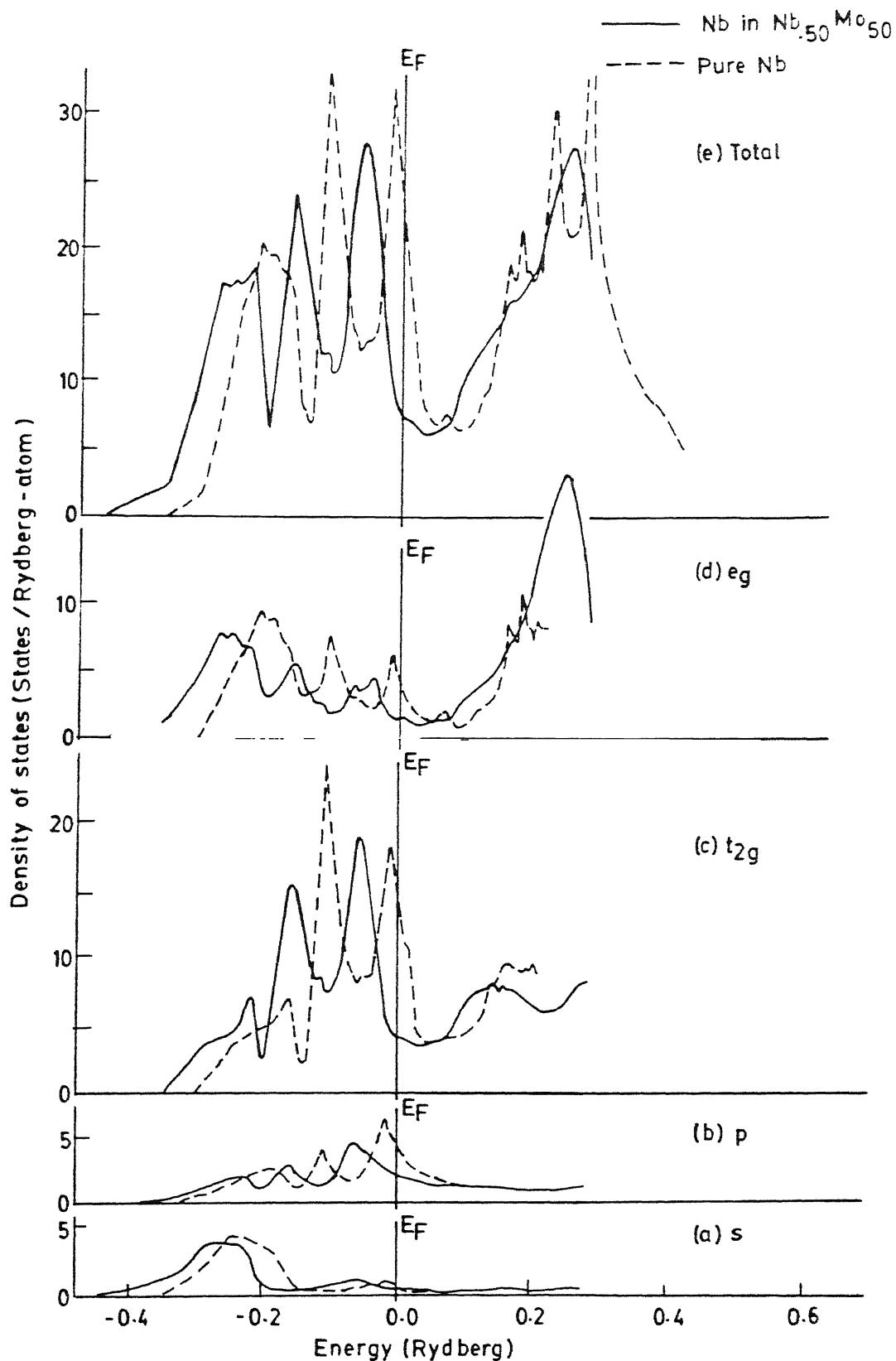


Figure-2.10 L-decomposition of the component density of states of Nb in the $\text{Nb}_{.50}\text{Mo}_{.50}$ alloy (full curves) and pure Nb (broken curves). The s, p, t_{2g} , e_g and total components are shown in figures (a), (b), (c), (d) and (e) respectively. The energy is measured with respect to the Fermi energy.

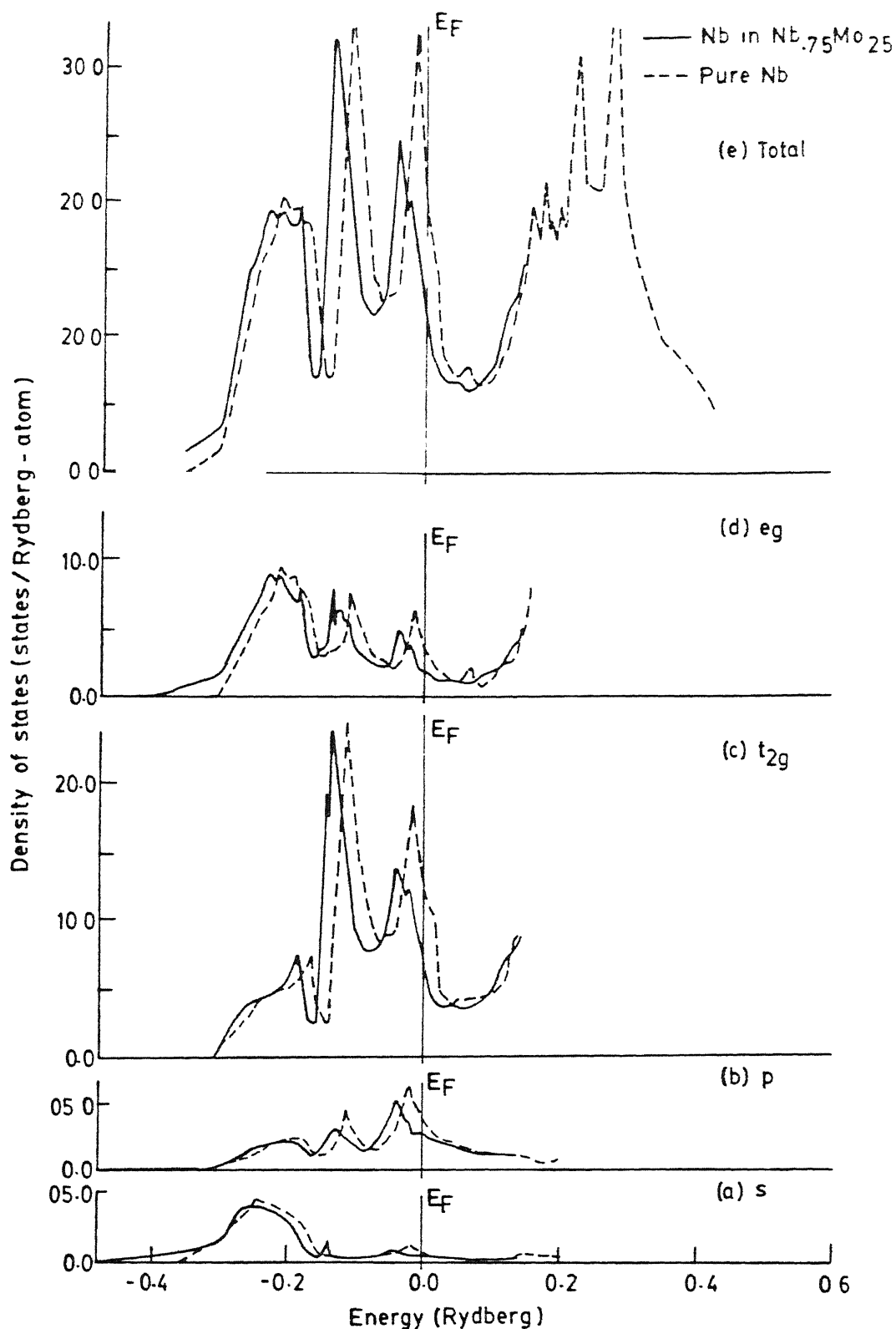


Figure-2.11 L-decomposition of the component density of states of Nb in the $\text{Nb}_{0.75}\text{Mo}_{0.25}$ alloy (full curves) and pure Nb (broken curves). The s, p, t_{2g} , e_g and total components are shown in figures (a), (b), (c), (d) and (e) respectively. The energy is measured with respect to the Fermi energy.

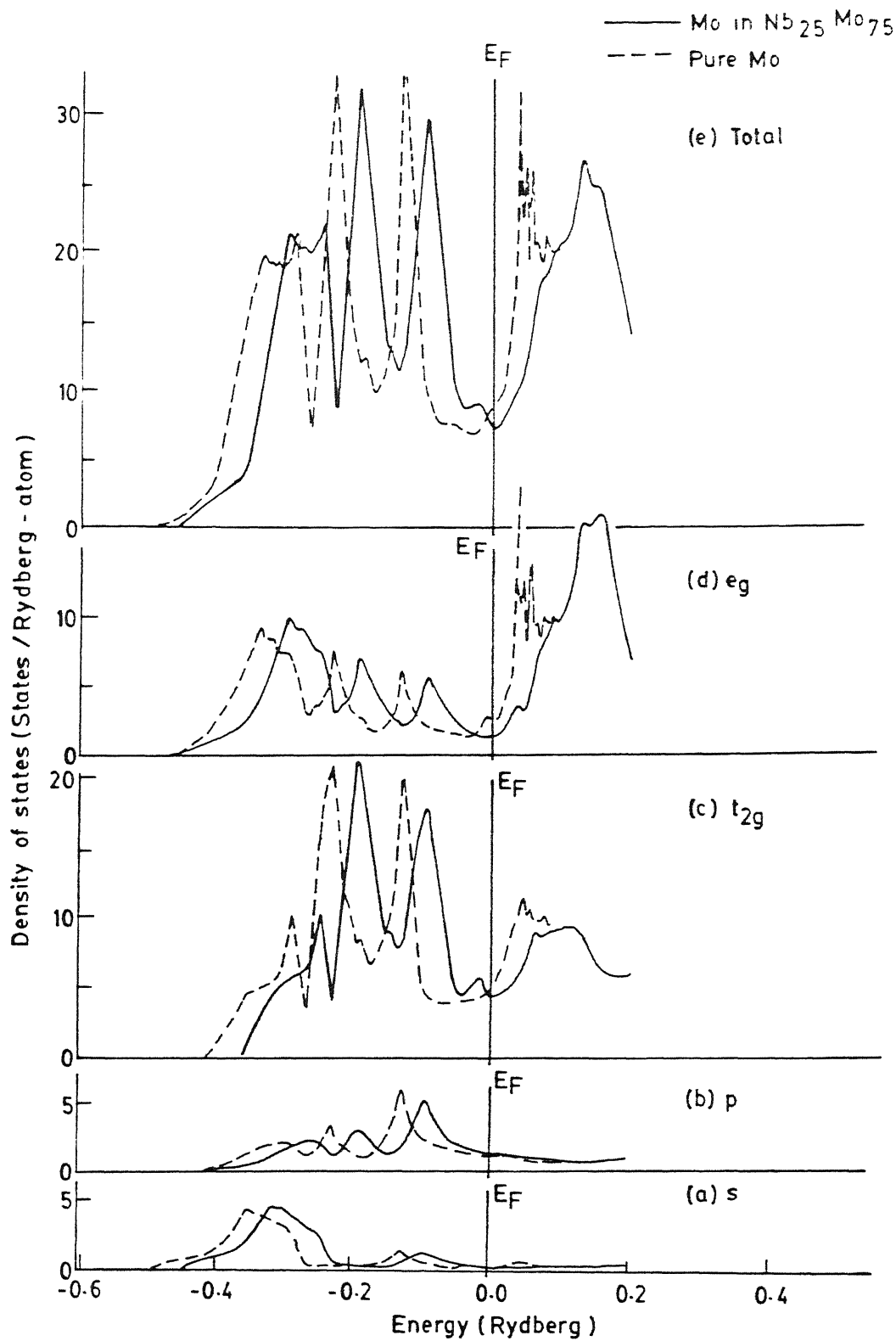


Figure-2.12 L-decomposition of the component density of states of Mo in the Nb_{0.25}Mo_{0.75} alloy (full curves) and pure Nb (broken curves). The s, p, t_{2g} , e_g and total components are shown in figures (a), (b), (c), (d) and (e) respectively. The energy is measured with respect to the Fermi energy.

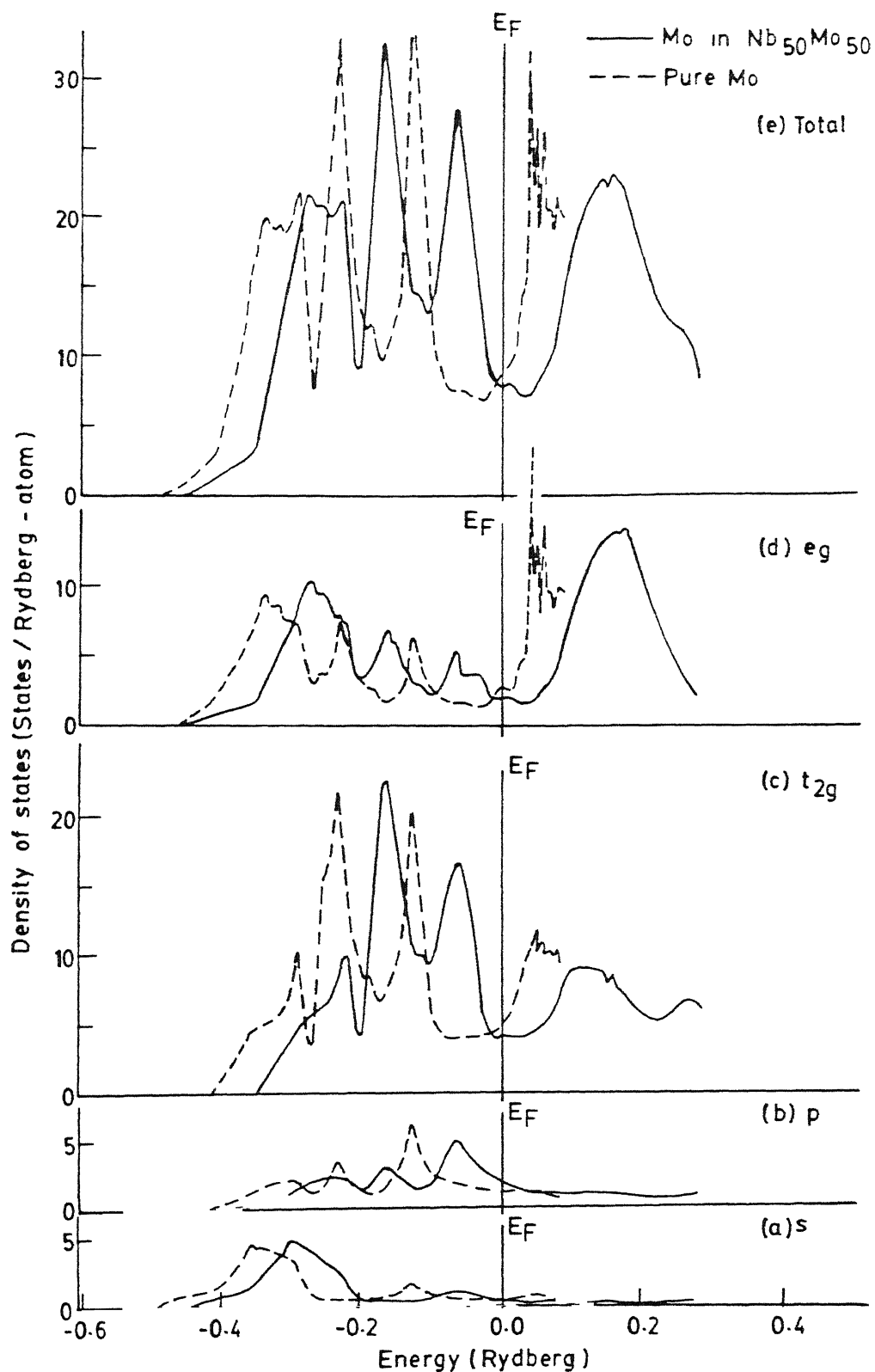


Figure-2.13 L-decomposition of the component density of states of Mo in the $\text{Nb}_{.50}\text{Mo}_{.50}$ alloy (full curves) and pure Nb (broken curves). The s, p, t_{2g} , e_g and total components are shown in figures (a), (b), (c), (d) and (e) respectively. The energy is measured with respect to the Fermi energy.

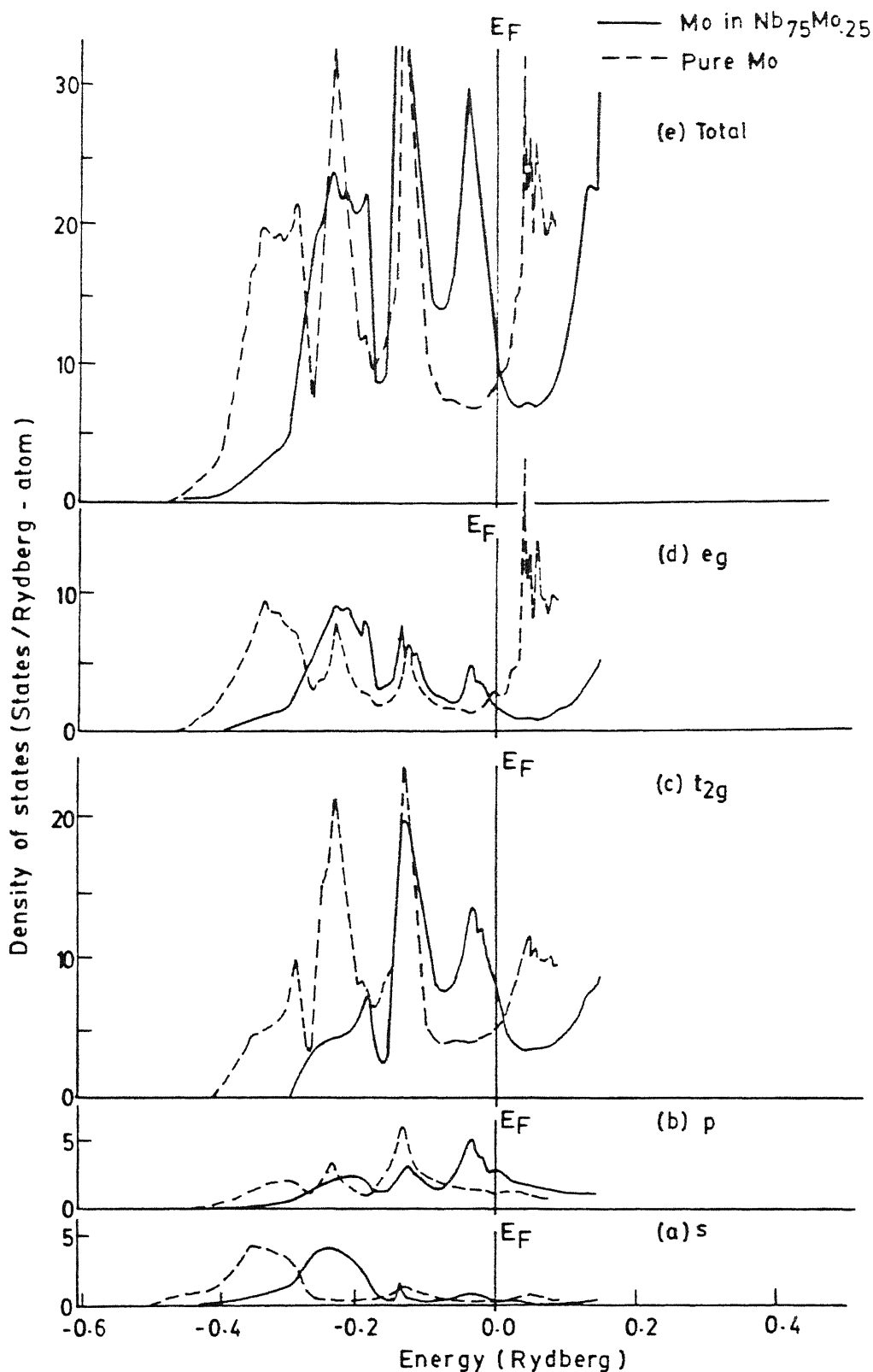


Figure-2.14 L-decomposition of the component density of state of Mo in the $\text{Nb}_{.75}\text{Mo}_{.25}$ alloy (full curves) and pure Nb (broke curves). The s, p, t_{2g} , e_g and total components are shown in figures (a), (b), (c), (d) and (e) respectively. The energy is measured with respect to the Fermi energy.

Nb component density of states in the alloy with pure Nb results, for the concentrations $x=0.25$, 0.50 and 0.75 respectively. All curves of Nb component density of states in the alloy shift towards the low energy regions. This shifting of curves decreases with the increase in the concentration x . This is because the change in Nb potential in figure 2.2, also decreases with increasing Nb concentration in the alloy.

Figures 2.12(a, b, c, d, e), 2.13(a, b, c, d, e) and 2.14(a, b, c, d, e) show the comparisons of s, p, t_{2g} , e_g and component density of states of Mo in the alloy with pure Mo results, for the concentrations $x=0.25$, 0.50 and 0.75 respectively. All curves of component density of states of Mo in the alloy shift towards the high energy regions. But this shifting of curves decreases with the increase in the concentration of Mo (y) in the alloy. This also reflects the same trend as observed in figure 2.4.

2.6 CONCLUSIONS

We have calculated the self-consistent charge densities, self-consistent potentials, density of states and component density of states of the Nb_xMo_y alloy for $x=0.25$, 0.50 and 0.75 by using the charge self-consistent KKR-CPA method. It is found that the maximum difference in the Nb (Mo) valence charge densities in the alloy with respect to pure Nb (Mo) is of the order of 10% near the muffin-tin radius. Also, the maximum

difference in the Nb (Mo) potentials in the alloy with respect to pure Nb (Mo) is of the order of 5% near the muffin-tin radius. The differences decrease with the increase in the concentration of Nb(Mo) in the alloy. The results of charge self-consistent KKR-CPA, show deviations from the density of states (DOS) of Nb-based rigid band model, in some energy ranges. It is also found that there are significant differences between the charge self-consistent density of states and the density of states reported by non-charge self-consistent KKR-CPA methods. This implies that the density of states is very sensitive to the Nb and Mo potentials. Our calculated density of states for the alloy at E_F is in good agreement with the experimental result obtained from the analysis of specific heat data. There is a good agreement between our results (component density of states) and soft x-ray spectra curves for $Nb_{.5}Mo_{.5}$ alloy.

CHAPTER 3

FORMULATION OF KORRINGA-KOHN-ROSTOKER CLUSTER-COHERENT- POTENTIAL-APPROXIMATION*

3.1 INTRODUCTION

During the last decade, the coherent potential approximation (CPA) has emerged as the most successful single-site approximation for calculating electronic structure of random substitutional binary alloys, both in the empirical tight-binding and first principles Korringa-Kohn-Rostoker (KKR) frameworks. Despite its success, the CPA, being a single site approximation, does not include correlated scattering from neighbouring sites. This could play an important role in systems having short range order and clustering tendencies¹⁹⁻²¹. To study the effect of correlated scattering, Gonis et al.⁴⁶ proposed the idea of an embedded cluster method. In this method, a cluster consisting of a central site and its shell of nearest neighbours was embedded in an effective medium determined within the Korringa-Kohn-Rostoker coherent-potential-approximation (KKR-CPA). However this method is not fully self-consistent. The idea of self consistent

*This work is already published in J. Phys.: Condensed Matter 2, 2653 (1990).

cluster CPA (CCPA) was proposed by some workers within the framework of some new approaches, like travelling cluster approximation²² and Augmented space formalism^{23,24} which preserve the herglotz properties of the Green's function^{47,48}. The augmented space formalism has been successfully applied to the calculation of electronic properties of binary alloys by several workers in the tight-binding framework^{49,50}.

One can use augmented space formalism to go beyond the single site approximation within the conventional KKR method⁵¹⁻⁵³. The aim of this chapter is to present this formulation, which will be called Korringa-Kohn-Rostoker cluster-coherent-potential-approximation (KKR-CCPA). Since there is a structural similarity between the tight-binding Green's function and KKR path operator, we shall first discuss augmented space formalism in the tight-binding framework and then discuss generalization to KKR framework. In section 3.2, we start with a brief discussion of the augmented space formalism in the tight-binding framework. This is first applied to a tight-binding Hamiltonian and tight-binding CPA (TB-CPA) equations are derived in section 3.3. We derive the tight-binding CCPA (TB-CCPA) equations by application of the augmented space formalism to the tight-binding Hamiltonian in section 3.4. Here, for simplicity, we limit our cluster size to two-atom only. In the tight-binding framework we have refined the technique such that various quantities appearing in the CCPA equations are calculated exactly. Till now these

quantities were being calculated by summing over an infinite series^{49,50}.

One of the features of the CPA is that in the low concentration limit it gives the features of a single impurity¹. In the same spirit, we want to examine whether CCPA density of states in the low concentration limit reduces to the two-impurity local density of states. The formulation of the two-impurity problem is given in section 3.5. In some earlier works on the CCPA^{49,50} as well as in the present work, we note rich structure in the CCPA density of states. We also wish to understand the structure in the CCPA density of states in the light of the two impurities local density of states. These structure have been explained by calculating the two-impurity local density of states in the tight-binding framework in chapter 4.

The derivation of the TB-CCPA equations forms the basis for extension of this method to the KKR framework. By using the correspondence between variables in the tight-binding and KKR frameworks, we derive the KKR-CCPA equations with the help of the TB-CCPA equations in section 3.6. Finally, conclusions are given in section 3.7.

3.2 THE AUGMENTED SPACE FORMALISM

CENTRAL LIBRARY
doc No. A.114032

The augmented space formalism is a technique of configuration averaging where configuration fluctuations are

systematically taken into account. The augmented space formalism was first introduced by Mookerjee²³ and later Gray and Kaplan²⁴ provided a detailed exposition. It has been successfully used for averaging one particle Green's function and functions related to two-particle Green's function. We will discuss this formulation in the tight-binding framework.

We consider the following tight-binding Hamiltonian with no off-diagonal disorder:

$$H = \sum_i E_i \mathcal{P}_i + \sum_{i \neq j} \sum V_{ij} \mathcal{T}_{ij}, \quad (3.1a)$$

where E_i is the site-energy corresponding to site i , and V_{ij} is hopping integral. $\mathcal{P}_i (= |i\rangle\langle i|)$ and $\mathcal{T}_{ij} (= |i\rangle\langle j|)$ are respectively projection and transfer operators in the Hilbert space \mathcal{H} spanned by the site labelled basis $\{|i\rangle\}$. The elements of Green's function for this system are

$$G_{ij} = \langle i | (E I - H)^{-1} | j \rangle. \quad (3.1b)$$

For a random binary alloy $A_x B_y$, the random site energy E_i can be written in terms of a random occupation parameters n_i as,

$$E_i = E_A n_i + E_B (1 - n_i),$$

where

$$n_i = \begin{cases} 1 & \text{if } i = A \\ 0 & \text{if } i = B \end{cases} \quad (3.1c)$$

with a probability distribution

$$P_i(n_i) = x \delta(n_i - 1) + y \delta(n_i)$$

which satisfies

$$P_i(n_i) \geq 0$$

$$\int P_i(n_i) dn_i = 1.$$

We may express $P_i(n_i)$ as²³

$$P_i(n_i) = -(1/\pi) \operatorname{Im} \langle f_i^0 | (n_i I - M_i)^{-1} | f_i^0 \rangle$$

where M_i is an operator in the configuration space θ_i of rank 2 spanned by $|f_i^0\rangle$ and $|f_i^1\rangle$ with a representation

$$M_i = x \mathcal{P}_{f_i^0} + y \mathcal{P}_{f_i^1} + (x y)^{1/2} (\mathcal{T}_{f_i^0} f_i^1 + \mathcal{T}_{f_i^1} f_i^0). \quad (3.2)$$

The augmented space theorem²³ then tells us that configuration average of a function is

$$\langle f[\{n_i\}] \rangle = \langle \phi | \tilde{f}[\{M_i\}] \phi \rangle, \quad (3.3)$$

where $|\phi\rangle = \prod_i |f_i^0\rangle$, is a member of the basis $|\phi_p\rangle = \prod_i |f_i^{s_i}\rangle$, ($s_i = 0, 1$ and $p = 1, 2 \dots 2^N$) belonging to the configuration space $\Phi = \prod_i \theta_i$ of rank 2^N . The function $\tilde{f}[\{M_i\}]$ is an operator in the augmented space $\psi = \mathcal{X} \otimes \Phi$ of rank $N \times 2^N$.

By the augmented space theorem, the elements of configuration averaged Green's function are

$$\langle G_{ij}(E) \rangle = \langle \psi_i | (E I - \tilde{H})^{-1} | \psi_j \rangle. \quad (3.4a)$$

The augmented space Hamiltonian \tilde{H} , is given by,

$$\tilde{H} = E_B \otimes \mathcal{I} + \delta E \sum_i \mathcal{P}_i \otimes M_i + \sum_i \sum_{i \neq j} V_{ij} \mathcal{T}_{ij} \otimes \mathcal{I}, \quad (3.4b)$$

where $\delta E = E_A - E_B$ and \mathcal{I} is the identity operator in the configuration space. Note that equation (3.4a) is exact, but cannot be evaluated because of the large dimensionality of the augmented space. Therefore, we look for some approximation which will reduce the size of the augmented space. For this purpose, we partition the augmented space into a subspace I spanned by $|\mathcal{C}, \phi_p\rangle$ and remaining subspace denoted by II. If we take a one-atom cluster, we will get the CPA equation as derived in section 3.3. For the CCPA, we have taken a two-atom cluster, as presented in section 3.4.

3.3 TIGHT-BINDING COHERENT-POTENTIAL-APPROXIMATION (TB-CPA)

In this case, we take the one-atom cluster \mathcal{C} consisting of the 0-th site. The space I is spanned by two basis vectors²³ $|0, f_0^0\rangle$ and $|0, f_0^1\rangle$.

Now we partition \tilde{H} as

$$\tilde{H} = \begin{bmatrix} H_I & H' \\ H'^T & H_{II} \end{bmatrix},$$

where

$$H_I = \begin{bmatrix} \bar{E} & W \\ W & \tilde{E} \end{bmatrix}, \quad (3.5a)$$

$$H_{II} = \left[\sigma_0 \sum_{i \neq 0} \mathcal{P}_i + \sum_{i \neq 0} \sum_{j \neq 0} V_{ij} \mathcal{T}_{ij} \right] \otimes \left[\mathcal{P}_{f_0^0} + \mathcal{P}_{f_0^1} \right], \quad (3.5b)$$

$$H' = \left[\sum_{j \neq 0} V_{0j} \mathcal{T}_{0j} \right] \otimes \left[\mathcal{P}_{f_0^0} + \mathcal{P}_{f_0^1} \right],$$

where

$$\bar{E} = x E_A + y E_B, \quad \tilde{E} = x E_B + y E_A \quad \text{and} \quad W = (x \ y) \frac{1}{2} (E_A - E_B).$$

By the partition theorem, $\langle G_{ij} \rangle$ may be written as the representation of the resolvent of an operator \hat{H} in the subspace I where

$$\hat{H} = H_I + H' (E \mathcal{P} - H_{II})^{-1} H'^T.$$

With the help of equation (3.5), we get

$$\hat{H} = H_I + A (\mathcal{P}_{f_0^0} + \mathcal{P}_{f_0^1}),$$

where

$$A = \sum_{j \neq 0} \sum_{k \neq 0} V_{0j} G_{jk}^0 V_{ko} . \quad (3.6)$$

Since we need only the $\langle 0, f_0^0 | \quad | f_0^0, 0 \rangle$ element of $(E\mathcal{G} - \hat{H})^{-1}$, we again partition \hat{H} as

$$\hat{H} = \begin{bmatrix} H_1 & H_{12} \\ H_{12}^T & H_2 \end{bmatrix} ,$$

where

$$H_1 = (\bar{E} + A) \mathcal{P}_0 \mathcal{P}_{f_0^0}^0 , \quad (3.7a)$$

$$H_{12} = W \mathcal{P}_0 \mathcal{T}_{f_0^0 f_0^1} , \quad (3.7b)$$

$$H_2 = (\tilde{E} + A) \mathcal{P}_{f_0^1}^1 \mathcal{P}_{f_0^1}^1 . \quad (3.7c)$$

By the partition theorem

$$\langle 0, f_0^0 | (E\mathcal{G} - \hat{H})^{-1} | f_0^0, 0 \rangle = \langle 0 | [E\mathcal{G} - H_1 - H_{12} (E\mathcal{G} - H_2)^{-1} H_{21}]^{-1} | 0 \rangle . \quad (3.8)$$

Let the coherent-potential Hamiltonian be

$$H_{eff} = \sum_i \sigma_i \mathcal{P}_i + \sum_{i \neq j} V_{ij} \mathcal{T}_{ij} , \quad (3.9)$$

then the Green's function for the coherent-potential medium

$$\langle G \rangle = \langle (E\mathcal{G} - H_{\text{eff}})^{-1} \rangle. \quad (3.10)$$

The matrix element G_{oo} of $\langle G \rangle$ is given by

$$G_{oo} = (E - \sigma_o - A)^{-1} \quad (3.11)$$

and

$$G_2 = (E I - H_2)^{-1} = (E I - \tilde{E} - A)^{-1}.$$

Putting the value of A from equation (3.11), we get

$$G_2 = (G_{oo}^{-1} - \tilde{E} + \sigma_o) . \quad (3.12)$$

By comparing equations (3.8) and (3.9), and eliminating G_2 with the help of equation (3.12) we get self consistent CPA equation in terms of the self energy:

$$\sigma_o = \bar{E} + \frac{W^2}{G_{oo}^{-1} + \sigma_o - \tilde{E}} . \quad (3.13)$$

This is identical to the CPA equations generated from more conventional methods. Note that this confirms the uniqueness of the CPA (in a single site case) as derived from various approaches such as multiple-scattering, embedding approaches etc.^{1,54}

3.4 TIGHT-BINDING CLUSTER-COHERENT-POTENTIAL APPROXIMATION (TB-CCPA)

We shall take, as an example, the cluster \mathcal{C} consisting of sites 0 and 1; i.e. we will include correlated scattering from two sites only.

The subspace I is spanned by eight basis vectors²³ $|0, \phi\rangle$, $|0, \phi_0\rangle$, $|0, \phi_1\rangle$, $|0, \phi_{01}\rangle$, $|1, \phi\rangle$, $|1, \phi_0\rangle$, $|1, \phi_1\rangle$ and $|1, \phi_{01}\rangle$, where $\phi = |f_0^0 f_1^0\rangle$, $\phi_1 = |f_0^0 f_1^1\rangle$, $\phi_0 = |f_0^1 f_1^0\rangle$ and $\phi_{01} = |f_0^1 f_1^1\rangle$. Now we partition \tilde{H} as

$$\tilde{H} = \begin{bmatrix} H_I & H' \\ H'^T & H_{II} \end{bmatrix},$$

where

$$\begin{aligned} H_I = & \bar{E} \left[\mathcal{P}_0 \otimes (\mathcal{P}_\phi + \mathcal{P}_{\phi_1}) + \mathcal{P}_1 \otimes (\mathcal{P}_{\phi_0} + \mathcal{P}_\phi) \right] \\ & + \tilde{E} \left[\mathcal{P}_1 \otimes (\mathcal{P}_{\phi_1} + \mathcal{P}_{\phi_{01}}) + \mathcal{P}_0 \otimes (\mathcal{P}_{\phi_{01}} + \mathcal{P}_{\phi_0}) \right] \\ & + (V_{01} \mathcal{T}_{01} + V_{10} \mathcal{T}_{10}) \otimes (\mathcal{P}_\phi + \mathcal{P}_{\phi_{01}} + \mathcal{P}_{\phi_0} + \mathcal{P}_{\phi_1}) \\ & + W \left[\mathcal{P}_0 \otimes (\mathcal{T}_{\phi_1 \phi_{01}} + \mathcal{T}_{\phi_{01} \phi_1} + \mathcal{T}_{\phi_0 \phi} + \mathcal{T}_{\phi \phi_0}) \right] \\ & + W \left[\mathcal{P}_1 \otimes (\mathcal{T}_{\phi \phi_1} + \mathcal{T}_{\phi_1 \phi} + \mathcal{T}_{\phi_{01} \phi_0} + \mathcal{T}_{\phi_0 \phi_{01}}) \right]. \end{aligned} \quad (3.14a)$$

We now replace the Hamiltonians H_{II} and H' by translationally symmetric effective Hamiltonians H_{II}^{eff} and H'^{eff} . Their diagonal and off-diagonal elements are σ_0 and σ_{ij} respectively. Thus

$$H_{II} = \left[\alpha_0 \sum_{i \neq 0,1} \mathcal{P}_i + \sum_{i,j \neq 0,1} \alpha_{ij} \mathcal{T}_{ij} \right] \otimes (\mathcal{P}_\phi + \mathcal{P}_{\phi_0} + \mathcal{P}_{\phi_1} + \mathcal{P}_{\phi_{01}}) ,$$

$$H' = \left[\sum_{i,j \neq 0,1} \alpha_{ij} \mathcal{T}_{ij} \right] \otimes (\mathcal{P}_\phi + \mathcal{P}_{\phi_0} + \mathcal{P}_{\phi_1} + \mathcal{P}_{\phi_{01}}) , \quad (3.14b)$$

$$\bar{E} = x E_A + y E_B, \quad \tilde{E} = x E_B + y E_A \text{ and } W = (x y)^{1/2} (E_A - E_B) .$$

By the partition theorem, $\langle G_{ij} \rangle$ may be written as the representation of the resolvent of an operator \hat{H} in the subspace I where

$$\hat{H} = H_I + H' (E \mathcal{P} - H_{II})^{-1} H'^T .$$

With the help of equations (3.14), we get

$$\hat{H} = H_I + \left[\xi_{00} (\mathcal{P}_0 + \mathcal{P}_1) + (\xi_{01} \mathcal{T}_{01} + \xi_{10} \mathcal{T}_{10}) \right] \otimes (\mathcal{P}_\phi + \mathcal{P}_{\phi_0} + \mathcal{P}_{\phi_1} + \mathcal{P}_{\phi_{01}}) ,$$

where

$$\xi_{00} = \sum_{j,k \neq 0,1} \alpha_{0j} G_{jk}^{\text{eff}(0,1)} \alpha_{ko} ,$$

$$\xi_{01} = \sum_{j,k \neq 0,1} \alpha_{0j} G_{jk}^{\text{eff}(0,1)} \alpha_{k1}$$

and

$$\xi_{10} = \sum_{j,k \neq 0,1} \alpha_{1j} G_{jk}^{\text{eff}(0,1)} \alpha_{ko} . \quad (3.15)$$

Since we need only the $\langle \psi, \phi | \dots | \phi, j \rangle$ element of $(E \mathcal{D} - \hat{H})^{-1}$, we again partition \hat{H} as

$$\hat{H} = \begin{bmatrix} H_1 & H_{12} \\ H_{12}^T & H_2 \end{bmatrix},$$

where

$$H_1 = \begin{bmatrix} \bar{E} + \xi_{00} & V_{01} + \xi_{01} \\ V_{10} + \xi_{10} & \bar{E} + \xi_{00} \end{bmatrix},$$

$$H_{12} = \begin{bmatrix} 0 & 0 & 0 & 0 & 0 & W \\ W & 0 & 0 & 0 & 0 & 0 \end{bmatrix}. \quad (3.16a)$$

The matrix H_2 is of rank 6 and can be obtained from equations (3.15). By the partition theorem,

$$\langle \psi, \phi | (E \mathcal{D} - \hat{H})^{-1} | \phi, j \rangle = \langle \psi | [E \mathcal{D} - H_1 - H_{12} (E \mathcal{D} - H_2)^{-1} H_{12}^T]^{-1} | j \rangle. \quad (3.16b)$$

Here,

$$H_{12} (E \mathcal{D} - H_2)^{-1} H_{12}^T = \begin{bmatrix} W Q_{00} W & W Q_{01} W \\ W Q_{10} W & W Q_{11} W \end{bmatrix},$$

where

$$Q_{ij} = [(E \mathcal{D} - H_2)^{-1}]_{ij}.$$

We define a translationally symmetric effective Hamiltonian H^{eff} such that its resolvent is the average Green's function $\langle G_{ij} \rangle$:

$$H^{eff} = \sigma_0 \sum_i \mathcal{P}_i + \sum_{i \neq j} \sigma_{ij} \mathcal{T}_{ij} . \quad (3.17)$$

Here σ_0 and σ_{ij} are diagonal and off-diagonal elements of H^{eff} . By comparing equations (3.16b) and (3.17), we get

$$\sigma_0 = \bar{E} + W Q_{00} W ,$$

$$\sigma_{01} = V_{01} + W Q_{01} W ,$$

$$\sigma_{10} = V_{10} + W Q_{10} W . \quad (3.18)$$

Here

$$Q_{00} = R_0^{-1} ,$$

$$Q_{10} = R_1^{-1} \gamma_{10} R_2^{-1} W R_3^{-1} \gamma_{01} R_4^{-1} W R_5^{-1} \gamma_{10} R_6^{-1} ,$$

$$Q_{01} = R_6^{-1} \gamma_{01} R_5^{-1} W R_4^{-1} \gamma_{10} R_3^{-1} W R_2^{-1} \gamma_{01} R_1^{-1} , \quad (3.19)$$

with

$$\gamma_{01} = V_{01} + \xi_{01} ,$$

$$\gamma_{10} = V_{10} + \xi_{10} ,$$

and

$$R_1 = E - \tilde{E} - \xi_{00} .$$

$$R_2 = E - \bar{E} - \xi_{00} - \gamma_{01} R_1^{-1} \gamma_{10} ,$$

$$R_3 = E - \tilde{E} - \xi_{00} - W R_2^{-1} W ,$$

$$R_4 = E - \bar{E} - \xi_{00} - \gamma_{10} R_3^{-1} \gamma_{01} ,$$

$$R_5 = E - \bar{E} - \xi_{00} - W R_4^{-1} W ,$$

$$R_6 = E - \tilde{E} - \xi_{00} - \gamma_{01} R_5^{-1} \gamma_{10} . \quad (3.20)$$

We have calculated ξ_{00} , ξ_{01} and ξ_{10} analytically by using the partition theorem on H^{eff} . The G^{eff} is given as

$$G^{eff} = (E I - H^{eff})^{-1} .$$

By partitioning this in 2×2 cluster subspace, we get

$$\begin{pmatrix} G_{00}^{eff} & G_{01}^{eff} \\ G_{10}^{eff} & G_{00}^{eff} \end{pmatrix} = \left[\begin{pmatrix} E - \sigma_0 & -\sigma_{01} \\ -\sigma_{10} & E - \sigma_0 \end{pmatrix} - \begin{pmatrix} \xi_{00} & \xi_{10} \\ \xi_{10} & \xi_{00} \end{pmatrix} \right]^{-1} . \quad (3.21)$$

Equation (3.21) then gives,

$$\xi_{00} = E - \sigma_0 - \left[G_{00}^{eff} - G_{01}^{eff} \left\{ G_{00}^{eff} \right\}^{-1} G_{10}^{eff} \right]^{-1} ,$$

$$\xi_{01} = -\sigma_{01} + \left[G_{00}^{eff} - G_{01}^{eff} \left\{ G_{00}^{eff} \right\}^{-1} G_{10}^{eff} \right]^{-1} G_{01}^{eff} \left\{ G_{00}^{eff} \right\}^{-1} ,$$

$$\xi_{10} = -\sigma_{10} + \left\{ G_{00}^{eff} \right\}^{-1} G_{10}^{eff} \left[G_{00}^{eff} - G_{01}^{eff} \left\{ G_{00}^{eff} \right\}^{-1} G_{10}^{eff} \right]^{-1} . \quad (3.22)$$

Note that ξ_{00} , ξ_{01} and ξ_{10} as given by (3.22) are exact. The earlier workers^{49,50} used to calculate these quantities approximately from (3.15) by recursion method.

3.5 TWO-IMPURITY PROBLEM

The study of the two impurity-problem is important while examining the structures in the CCPA density of states. Let us embed two impurities A and B at the sites labelled as 0 and 1 in the CPA effective medium. Then the Hamiltonian is

$$H^I = \sigma_0 \sum_{i \neq 0,1} \mathcal{P}_i + \sum_{i,j \neq 0,1} \sigma_{ij} \mathcal{T}_{ij} + E_A \mathcal{P}_0 + E_B \mathcal{P}_1 + V(\mathcal{T}_{01} + \mathcal{T}_{10}) . \quad (3.23)$$

The Hamiltonian for effective medium is given by

$$H^{eff} = \sigma_0^{eff} \sum_i \mathcal{P}_i + \sigma_1^{eff} \sum_{i \neq j} \mathcal{T}_{ij} . \quad (3.24)$$

σ_1^{eff} is only for nearest neighbours and for no off-diagonal disorder, $\sigma_{01} = \sigma_{10} = \sigma_1^{\text{eff}}$. The effective medium may be pure solid or the CPA medium and the corresponding values of diagonal self energies σ_0^{eff} are $E_{\text{A(B)}}$ or σ_0^{CPA} respectively. The value of σ_1^{eff} is equal to V for both cases. The impurity and the medium Green's functions are

$$G^{\text{I}} = \begin{pmatrix} \psi^{\text{I}} & G \\ G^{\text{T}} & \theta \end{pmatrix}, \quad (3.25a)$$

$$G^{\text{eff}} = \begin{pmatrix} \psi^{\text{eff}} & G \\ G^{\text{T}} & \theta \end{pmatrix}, \quad (3.25b)$$

where

$$\psi^{\text{I}} = \begin{pmatrix} E - E_{\text{A}} & -V \\ -V & E - E_{\text{B}} \end{pmatrix},$$

$$\psi^{\text{eff}} = \begin{pmatrix} E - \sigma_0^{\text{eff}} & -\sigma_1^{\text{eff}} \\ -\sigma_1^{\text{eff}} & E - \sigma_0^{\text{eff}} \end{pmatrix},$$

$$G = \begin{pmatrix} 0 & 0 & 0 & \dots \\ -\sigma_1^{\text{eff}} & 0 & 0 & \dots \end{pmatrix},$$

$$\theta = \begin{bmatrix} E - \sigma_0^{eff} & -\sigma_1^{eff} & 0 & \dots\dots\dots \\ -\sigma_1^{eff} & E - \sigma_0^{eff} & 0 & \dots\dots\dots \\ 0 & 0 & 0 & \dots\dots\dots \\ \vdots & \vdots & \vdots & \dots\dots\dots \end{bmatrix}, \quad (3.26)$$

here G^T is the transpose of G .

By simple partitioning (3.25) into a space spanned by 0 and 1 and the rest, we get

$$\begin{bmatrix} G_{00}^I & G_{01}^I \\ G_{10}^I & G_{11}^I \end{bmatrix} = (\psi^I - G \theta^{-1} G^T)^{-1},$$

$$\begin{bmatrix} G_{00}^{eff} & G_{01}^{eff} \\ G_{10}^{eff} & G_{11}^{eff} \end{bmatrix} = (\psi^{eff} - G \theta^{-1} G^T)^{-1}. \quad (3.27)$$

After solving equation (3.27), we get

$$G_{00} = \frac{\beta_B G_{00}^{eff} - G_{01}^{eff} [(\sigma_0 - E_B) G_{10}^{eff} + \alpha]}{\beta_A \beta_B - [(\sigma_0 - E_A) G_{01}^{eff} + \alpha] [(\sigma_0 - E_B) G_{10}^{eff} + \alpha]}, \quad (3.28a)$$

$$G_{11} = \frac{\beta_A G_{00}^{eff} - G_{10}^{eff} [(\sigma_0 - E_A) G_{01}^{eff} + \alpha]}{\beta_A \beta_B - [(\sigma_0 - E_B) G_{10}^{eff} + \alpha] [(\sigma_0 - E_A) G_{01}^{eff} + \alpha]}, \quad (3.28b)$$

where G_{ij}^{eff} is the Green's function for the effective medium, and

$$\alpha = (\sigma_1^{eff} - V) G_{00}^{eff} ,$$

$$\beta_A = 1 + (\sigma_0 - E_A) G_{00}^{eff} + (\sigma_1^{eff} - V) G_{10}^{eff} ,$$

and

$$\beta_B = 1 + (\sigma_0 - E_B) G_{00}^{eff} + (\sigma_1^{eff} - V) G_{01}^{eff} . \quad (3.28c)$$

The local density of states (LDOS) ρ_i on the i -th site is then obtained by

$$\rho_i = -(1/\pi) \operatorname{Im} (G_{ii}^{eff}) \quad \left\{ i = 0 \text{ or } 1 \right\} .$$

Equation (3.28) reduces in the single impurity limit for $E_B = \sigma_0$ as $(\sigma_1 = V, \alpha = 0, \beta_B = 1)$

$$G_{00} = D_A G_{00}^{eff} ,$$

where

$$D_A = [1 + (\sigma_0 - E_A) G_{00}^{eff}]^{-1} .$$

3.6 KORRINGA-KOHN-ROSTOKER CLUSTER-COHERENT-POTENTIAL-APPROXIMATION

In the KKR framework, an alloy is modeled by a random array of muffin-tin potentials of A or B type. The on-the-shell matrix elements of single muffin-tin t -matrices are¹⁻³

$$t_l^{A(B)}(\kappa) = -\frac{1}{\kappa} \exp(i\delta_l) \sin(\delta_l) , \quad (3.29)$$

where $\kappa = (|E|)^{1/2}$ and δ_l are phase shifts. The path operator matrices are given by

$$T_{ij} = \left\{ [C - B(\kappa)]^{-1} \right\}_{ij}, \quad (3.30)$$

where $C = t^{-1}$ and $B(\kappa)$ is the matrix of real space structure function¹ $B_{ij}(\kappa)$. Here, we have suppressed the angular momentum indices. We note that $B(\kappa)$ depends only on the lattice structure and does not contain any disorder while $C(\kappa)$ has a binary distribution. For a random binary alloy the random variable C can be written in terms of the random parameter n_i as

$$C_i = C_A n_i + C_B (1 - n_i),$$

where n_i is given by equation (3.1c). Also we define an operator D as

$$\begin{aligned} D &= T^{-1} = C - B \\ &= \sum_i C_i \mathcal{P}_i - \sum_{i \neq j} B_{ij} \mathcal{T}_{ij} = C_B + \delta C \sum_i \mathcal{P}_i n_i - \sum_{i \neq j} B_{ij} \mathcal{T}_{ij}, \end{aligned}$$

and

$$\delta C = C_A - C_B.$$

A comparison of equations (3.30) and (3.1b) shows that T_{ij} is structurally similar to G_{ij} and hence the augmented space formulation developed in section 3.4 for the tight-binding-CCPA, can straightforwardly be applied to derive the KKR-CCPA equations⁵¹⁻⁵³. The relationship between

tight-binding and KKR formulations becomes clear if we note the following correspondence.

$$\begin{aligned}
 G &\longleftrightarrow T \\
 E_i &\longleftrightarrow C_i \\
 V &\longleftrightarrow -B \\
 H_I, H_{II} &\longleftrightarrow D_I, D_{II}. \\
 E &\longleftrightarrow 0
 \end{aligned} \tag{3.31}$$

The procedure for generating the CCPA by partitioning of the augmented space is identical to that described in section 3.4. By using equation (3.31), we get the KKR-CCPA equations as

$$C = \bar{C} - W'Q'_{\sigma\sigma}W' ,$$

$$\mathcal{B}_{01} = B_{01} + W'Q'_{\sigma 1}W' ,$$

$$\mathcal{B}_{10} = B_{10} + W'Q'_{1\sigma}W' . \tag{3.32}$$

Here,

$$\mathcal{B}_{ij} = B_{ij} + b_{ij} ,$$

$$Q'_{\sigma\sigma} = R'^{-1}_{\sigma} ,$$

$$Q'_{1\sigma} = R'^{-1}_1 \gamma'_{10} R'^{-1}_2 W' R'^{-1}_3 \gamma'_{01} R'^{-1}_4 W' R'^{-1}_5 \gamma'_{10} R'^{-1}_{\sigma} ,$$

$$Q'_{\sigma 1} = R'^{-1}_{\sigma} \gamma'_{01} R'^{-1}_5 W' R'^{-1}_4 \gamma'_{10} R'^{-1}_3 W' R'^{-1}_2 \gamma'_{01} R'^{-1}_1 . \tag{3.33}$$

And

$$\gamma'_{01} = B_{01} + \xi'_{01} \quad ,$$

$$\gamma'_{10} = B_{10} + \xi'_{10} \quad ,$$

$$R'_1 = \tilde{C} - \xi'_{00} \quad ,$$

$$R'_2 = \bar{C} - \xi'_{00} - \gamma'_{01} R'^{-1}_1 \gamma'_{10} \quad ,$$

$$R'_3 = \tilde{C} - \xi'_{00} - W' R'^{-1}_2 W' \quad ,$$

$$R'_4 = \tilde{C} - \xi'_{00} - \gamma'_{10} R'^{-1}_3 \gamma'_{01} \quad ,$$

$$R'_5 = \bar{C} - \xi'_{00} - W' R'^{-1}_4 W' \quad ,$$

$$R'_6 = \tilde{C} - \xi'_{00} - \gamma'_{01} R'^{-1}_5 \gamma'_{10} \quad , \quad (3.34)$$

where

$$\bar{C} = x C_A + y C_B, \quad \tilde{C} = x C_B + y C_A \quad \text{and} \quad W' = (x \ y)^{1/2} (C_A - C_B).$$

Also,

$$\xi'_{00} = C - \left[T^{eff}_{00} - T^{eff}_{01} \left\{ T^{eff}_{00} \right\}^{-1} T^{eff}_{10} \right]^{-1} \quad ,$$

$$\xi'_{01} = -\mathcal{B}_{01} + \left[T^{eff}_{00} - T^{eff}_{01} \left\{ T^{eff}_{00} \right\}^{-1} T^{eff}_{10} \right]^{-1} T^{eff}_{01} \left\{ T^{eff}_{00} \right\}^{-1} \quad ,$$

$$\xi'_{10} = -\mathcal{B}_{10} + \left\{ T^{eff}_{00} \right\}^{-1} T^{eff}_{10} \left[T^{eff}_{00} - T^{eff}_{01} \left\{ T^{eff}_{00} \right\}^{-1} T^{eff}_{10} \right]^{-1} \quad . \quad (3.35)$$

Now the average electronic density of states for the alloy can be calculated by the formula¹

$$\delta \rho(E) = \rho_{\text{eff}}(E) - \rho_0(E) = \frac{-1}{N\pi} \text{Im Tr} \left[\langle T \frac{dC}{dE} \rangle - \langle T \rangle \frac{dB_q}{dE} \right], \quad (3.36)$$

where $\rho_0(E)$ is the free electron density of states, $\rho_{\text{eff}}(E)$ is the density of states for the effective medium, N is the total number of unit cells in the solid and B_q is the Fourier transform of B_{ij} . The configuration averages in equation (3.36) can be calculated using the augmented space formalism as shown in section 3.1.

3.7 CONCLUSION

We have derived the TB-CCPA equations by application of the augmented space formalism to the tight-binding Hamiltonian. We were also able to refine the TB-CCPA method such that various quantities, which were being calculated approximately so far, are calculated exactly. We have formulated the two-impurity problem to calculate the local density of states in the tight binding framework. We have derived the KKR-CCPA equations with the help of the TB-CCPA equations using the correspondence between variables in the tight-binding and KKR frameworks.

CHAPTER 4

APPLICATION OF KORRINGA-KOHN-ROSTOKER CLUSTER-COHERENT-POTENTIAL-APPROXIMATION*

4.1 INTRODUCTION

Because of its complexity, implementation of the Korringa-Kohn-Rostoker cluster-coherent-potential-approximation (KKR-CCPA) in realistic systems is difficult and involves lengthy computation. To our knowledge no successful implementation has been carried out on any realistic system to this date. In this chapter, as a test case, we have applied the KKR-CCPA to an s-phase-shift semicircular model. The model has several advantages: (i) Because of the semicircular modeling, the involved \vec{k} -space integration required to obtain the site-diagonal path operator, is bypassed. This reduces the computational effort and allows us to concentrate more on the effect of correlated scattering, which is the principal aim of this work. (ii) The Korringa-Kohn-Rostoker coherent-potential-approximation (KKR-CPA) based on this model has been tried out before by Soven²⁵. This allows us to compare the earlier work, based on conventional methods, with our augmented space

*This work is already published in J. Phys.: Condensed Matter 2, 2653 (1990).

generalization. However, the ad hoc assumption of a semicircular density of states for the structure factor, allows us only to obtain the site-diagonal path operator. It does not tell us how to obtain the off-diagonal elements, which are also necessary in the cluster-coherent-potential-approximation (CCPA). In order to circumvent this difficulty, we have first shown an exact analogy in the mathematical structure in the CCPA equations of the KKR method for this model and the tight-binding method for the semicircular model. The path operator in the KKR method has its counterpart in the Green's function in the tight-binding framework. We have also shown through the analogy, that the semicircular model is essentially a Bethe lattice approximation. This allows us to model the off-diagonal elements of the path operator. It also gives us a clear insight into the approximations involved in the model.

In section 4.2, we apply the KKR-CCPA formulation to the s-phase-shift semicircular model. The Bethe lattice model in the tight-binding framework, is examined in section 4.3. The KKR-CCPA equations for s-phase-shift semicircular model and the tight-binding CCPA (TB-CCPA) equations for the semicircular model are compared and one-to-one correspondence between them is established in section 4.4. In section 4.5, we apply the KKR-CCPA and the TB-CCPA methods to the s-phase-shift semicircular model and Bethe lattice model respectively. We also apply the formulation of two-impurity problem to calculate the local density of states, by embedding the two-atom cluster

in the coherent-potential-approximation (CPA) medium. In this way, we explain the structure of the CCPA density of states. The results of our calculations are presented in this section. Finally we give our conclusions in section 4.6.

4.2 s-PHASE SHIFT SEMICIRCULAR MODEL

We shall illustrate our KKR-CCPA formalism by applying it to a simple model. This will also bring us in contact with the single-site muffin-tin KKR-CPA work of Soven²⁵. As in that work, we shall assume that only the s-phase shift dominates, so that B , t and T become scalars in the angular momentum space. For this model, like Soven²⁵, we shall assume that the phase-shift has resonance behaviour and the cotangent of phase shift is given by

$$c_{\mathbf{A}(\mathbf{B})} = \frac{E_{\mathbf{A}(\mathbf{B})} - E}{\Gamma_{\mathbf{A}(\mathbf{B})}} \quad (4.1)$$

where $E_{\mathbf{A}(\mathbf{B})}$ is the resonant energy and $\Gamma_{\mathbf{A}(\mathbf{B})}$ is the resonance half-width.

In order to simplify the problem further, we assume that the structure function²⁵

$$\tilde{B}_{\mathbf{q}}^{\pm} = \frac{B_{\mathbf{q}}^{\pm}}{\kappa} - 1 \quad , \quad (4.2)$$

has no explicit dependence on energy. Here $B_{\mathbf{q}}^{\pm}(\kappa)$ is the Fourier transform of B_{ij} . From equation (3.29) of chapter 3 we get

$$C(x) = t^{-1}(x) = -x \cot \delta_0 + 1 = -x c + 1 \quad (4.3)$$

where c is given by equation (4.1).

The path operator

$$T_{ij} = \frac{1}{N} \sum_{\vec{q}} \exp(-i\vec{q} \cdot \vec{R}_{ij}) \frac{1}{(c - B_{\vec{q}})} \quad (4.4)$$

$$T_{00} = -\frac{1}{x N} \sum_{\vec{q}} (c + \tilde{B}_{\vec{q}})^{-1} = -\frac{1}{x} \int (c + b)^{-1} f^0(b) db \quad ,$$

where $f^0(b)$ is a distribution function given by

$$f^0(b) = \frac{1}{N} \sum_{\vec{q}} \delta(b - \tilde{B}_{\vec{q}}) \quad (4.5)$$

We choose $f^0(b)$ as²⁵

$$\left. \begin{aligned} f^0(b) &= \frac{2}{\pi} (1 - b^2)^{1/2}, & |b| \leq 1 \\ &= 0, & |b| > 1. \end{aligned} \right] \quad (4.6)$$

Then,

$$T_{00} = -\frac{1}{x} g_{00} \quad ,$$

where

$$g_{00} = 2 [c + (c^2 - 1)^{1/2}] \quad (4.7)$$

Similarly,

$$T_{01} = T_{10} = - \frac{1}{\pi} \int f'(b) (c + b)^{-1} db, \quad (4.8a)$$

where distribution function $f'(b)$ is defined as,

$$f'(b) = \frac{1}{N} \sum_{\vec{q}} \exp(-i\vec{q} \cdot \vec{R}_{01}) \delta(b - \tilde{B}_{\vec{q}}). \quad (4.8b)$$

We choose $f'(b)$ such that⁵²

$$\left. \begin{aligned} f'(b) &= - \frac{\lambda}{\pi} (1 - b^2)^{1/2} b, & |b| \leq 1 \\ &= 0, & |b| > 1 \end{aligned} \right] , \quad (4.9)$$

where λ is a constant. The validity of this choice will be discussed in section 4.4. Hence

$$T_{01} = T_{10} = - \frac{1}{\pi} \int_{-1}^{+1} \left(\frac{-\lambda}{\pi} \right) (1 - b^2)^{1/2} (c + b)^{-1} b db = - \frac{1}{\pi} g_{01},$$

where,

$$g_{01} = \frac{\lambda}{8} (g_{00})^2. \quad (4.10a)$$

From equation (4.8b) we get,

$$\tilde{B}_{01} = \int f'(b) b db = - \frac{\lambda}{8}. \quad (4.10b)$$

Taking the Fourier transform of (4.2) we get,

$$B_{01} = B_{10} = \pi \tilde{B}_{01} = - \pi \frac{\lambda}{8}.$$

From equation (3.33) of chapter 3 we get,

$$\mathcal{B}_{\mathbf{o}_1} = \mathcal{B}_{\mathbf{i}_0} = B_{\mathbf{o}_1} + b_{\mathbf{o}_1} ,$$

where,

$$b_{\mathbf{o}_1} = b_{\mathbf{i}_0} = \kappa \beta_{\mathbf{o}_1} . \quad (4.11)$$

The Fourier transform of (4.11) gives us,

$$\mathcal{B}_{\vec{q}} = B_{\vec{q}} + b_{\vec{q}}$$

and

$$b_{\vec{q}}(\kappa) = \sum_{\mathbf{j} \neq \mathbf{o}} b_{\mathbf{o}_j} \exp(i\vec{q} \cdot \vec{R}_{\mathbf{o}_j}) = b_{\mathbf{o}_1} \exp(i\vec{q} \cdot \vec{R}_{\mathbf{o}_1}) .$$

The diagonal elements of path operator within the CCPA are given as⁵²

$$T_{\mathbf{oo}}^{\text{eff}} = - \frac{1}{\kappa N} \sum_{\vec{q}} (c + \tilde{B}_{\vec{q}})^{-1} \left[1 + \frac{\beta_{\mathbf{o}_1} \exp(i\vec{q} \cdot \vec{R}_{\mathbf{o}_1})}{(c + \tilde{B}_{\vec{q}})} \right]^{-1} .$$

Expanding by Taylor expansion near $\beta_{\mathbf{o}_1} = 0$ and retaining only the first order term we get,

$$\begin{aligned} T_{\mathbf{oo}}^{\text{eff}} &= T_{\mathbf{oo}} + \frac{\beta_{\mathbf{o}_1}}{\kappa} \int_{-1}^{+1} f'(b) (c + b)^{-2} db \\ &= T_{\mathbf{oo}} - \frac{\lambda \beta_{\mathbf{o}_1}}{\kappa} \left[2c + \frac{2c^2 - 1}{(c^2 - 1)^{1/2}} \right] \end{aligned}$$

or

$$T_{00}^{eff} = - \frac{1}{\pi} g_{00}^{eff} .$$

where

$$g_{00}^{eff} = g_{00} + \lambda \beta_{01} \left[2c + \frac{2c^2 - 1}{(c^2 - 1)^{1/2}} \right] . \quad (4.12)$$

The off-diagonal elements of path operator are given by⁵²

$$\begin{aligned} T_{01}^{eff} &= - \frac{1}{\pi N} \sum_{\vec{q}} \exp(-i\vec{q} \cdot \vec{R}_{01}) (c + \tilde{B}_{\vec{q}})^{-1} \left[1 + \frac{\beta_{01} \exp(i\vec{q} \cdot \vec{R}_{01})}{(c + \tilde{B}_{\vec{q}})} \right]^{-1} \\ &= T_{01} + \frac{\beta_{01}}{\pi} \int_{-1}^{+1} f^0(b) (c + b)^{-2} db \\ &= T_{01} - \frac{2\beta_{01}}{\pi} \left[1 + \frac{c}{(c^2 - 1)^{1/2}} \right] . \end{aligned}$$

Thus

$$T_{01}^{eff} = T_{10}^{eff} = - \frac{1}{\pi} g_{01}^{eff} ,$$

where

$$g_{01}^{eff} = g_{01} + 2\beta_{01} \left[1 + \frac{c}{(c^2 - 1)^{1/2}} \right] . \quad (4.13)$$

Note that the form of the function g_{01}^{eff} retains its herglotz properties even after this additional approximation.

Finally the change in density of states (δDOS) per atom is given by the equation (3.36) of chapter 3, which is

$$\delta\rho(E) = -\frac{\text{Im}}{\pi} \left[\left\langle T_{00} \frac{dC}{dE} \right\rangle - \frac{1}{N} \sum_{\vec{q}} (C^{\text{eff}} - B_{\vec{q}} - b_{\vec{q}})^{-1} \frac{d(B_{\vec{q}} + b_{\vec{q}})}{dE} \right], \quad (4.14)$$

where

$$\left\langle T_{00} \frac{dC}{dE} \right\rangle = T_{00}^{\text{eff}} U^{\text{eff}},$$

$$U^{\text{eff}} = \bar{U} + \frac{(C^{\text{eff}} - \bar{C})}{(C_A - C_B)} (U_A - U_B), \quad (4.15)$$

$$U = \frac{dC}{dE}, \quad C^{\text{eff}} = -\kappa C + 1.$$

Here eff is used to denote the effective medium, and

$$\bar{C} = x C_A + y C_B.$$

From equation (4.15)

$$U^{\text{eff}} = \kappa \left[\frac{x}{G_A} + \frac{y}{G_B} \right] + \frac{(1-C)}{2\kappa} + \frac{(1-\bar{C})}{(C_A - C_B)} \kappa \left[\frac{1}{G_A} - \frac{1}{G_B} \right] \quad (4.16)$$

where, $\bar{C} = x C_A + y C_B$

and $c_{A(B)}$ is given by equation (4.1). Also c is the cotangent of phase shift for effective medium within the KKR-CPA or the KKR-CCPA. By equation (4.14)

$$\delta\rho(E) = -\frac{1}{\pi} \text{Im} [\text{First part} + \text{Second part}].$$

where

$$\text{First part} = T_{oo}^{eff} U^{eff} \quad (4.17)$$

$$\text{Second part} = - \frac{1}{N} \sum_{\vec{q}} (C^{eff} - B_{\vec{q}} - b_{\vec{q}})^{-1} \frac{d(B_{\vec{q}} + b_{\vec{q}})}{dE} \quad (4.18)$$

Second part can be written as

$$\text{Second part} = \frac{1}{N} \sum_{\vec{q}} f(B_{\vec{q}} + b_{\vec{q}}) \quad (4.19)$$

where function $f(B_{\vec{q}})$ is defined as

$$f(B_{\vec{q}}) = (x c - 1 + B_{\vec{q}})^{-1} \frac{d(B_{\vec{q}})}{dE} \quad (4.20)$$

Now the Taylor series expansion of $f(B_{\vec{q}})$ near $b_{\vec{q}} = 0$ (up to first order terms only) equation (4.19) gives

$$\begin{aligned} \text{Second part} = \frac{1}{2N E} \left[\sum_{\vec{q}} \left[\frac{(\tilde{B}_{\vec{q}}+1)}{(c+\tilde{B}_{\vec{q}})} - \beta_{o1}(\tilde{B}_{\vec{q}}+1) \exp(i\vec{q} \cdot \vec{R}_{o1}) \right. \right. \\ \left. \left. + \frac{\beta_{o1} \exp(i\vec{q} \cdot \vec{R}_{o1})}{(c + \tilde{B}_{\vec{q}})} \right] \right] \quad (4.21) \end{aligned}$$

Equation (4.21) can be written as

$$\text{Second part} = S_1 + S_2 + S_3 + S_4 + S_5$$

where,

$$S_1 = \frac{1}{2E} \int_{-1}^{+1} f^0(b) (c+b)^{-1} b \, db = - \frac{1}{2E} \left[2c^2 - 1 + 2c (c^2 - 1)^{1/2} \right],$$

$$S_2 = \frac{1}{2E} \int_{-1}^{+1} f^0(b) (c+b)^{-1} db = \frac{1}{E} \left[c + (c^2 - 1)^{1/2} \right],$$

$$S_3 = - \frac{1}{2E} \int_{-1}^{+1} \frac{\beta_{01} f'(b) b \, db}{(c+b)^2} = - \frac{\lambda \beta_{01}}{4E} \left[6c^2 - 1 + \frac{(6c^3 - 4c)}{(c^2 - 1)^{1/2}} \right],$$

$$S_4 = - \frac{1}{2E} \int_{-1}^{+1} \frac{\beta_{01} f'(b) \, db}{(c+b)^2} = \frac{\lambda \beta_{01}}{2E} \left[2c + \frac{(2c^2 - 1)}{(c^2 - 1)^{1/2}} \right],$$

$$S_5 = \frac{\beta_{01}}{2E} \int_{-1}^{+1} f'(b) (c+b)^{-1} db = \frac{\lambda \beta_{01}}{4E} \left[2c^2 - 1 + 2c(c^2 - 1)^{1/2} \right] \quad (4.22)$$

Substituting the values of equations (4.16), (4.17) and (4.22) in equation (4.14), we get the formula for the change in density of states as⁵²

$$\delta\rho(E) = \frac{\text{Im}}{\pi} \left[g_{00}^{\text{eff}} \left\{ \frac{x}{\Gamma_A} + \frac{y}{\Gamma_B} + \frac{(c - \bar{c})}{(c_A - c_B)} \left(\frac{1}{\Gamma_A} - \frac{1}{\Gamma_B} \right) \right\} \right] \quad (4.23)$$

Note that this formula is valid for the KKR-CCPA as well as the KKR-CPA depending upon the value of c . Here g_{00}^{eff} is given by equation (4.12).

4.3 BETHE LATTICE MODEL

Bethe lattices have no closed loops and are completely characterized by their number of nearest neighbours Z or connectivity $K = Z-1$. For the tight-binding Hamiltonian on the Bethe lattice the Green's functions for a perfect system can be calculated exactly by renormalized perturbation expansion⁵⁵ and are given by

$$G_{oo} = \frac{2K}{(K-1)(E-E_o) + (K+1)\sqrt{(E-E_o)^2 - 4KV^2}} ,$$

$$G_{o1} = G_{1o} = G_{oo} \left[\frac{2V}{(E-E_o) + \sqrt{(E-E_o)^2 - 4KV^2}} \right] , \quad (4.24)$$

where E_o and V are the diagonal and off-diagonal elements of the nearest neighbour Hamiltonian. We take $V = 0.5/\sqrt{K}$ which gives unit half band-width. For an alloy $A_x B_y$ we take the site energies E_o as $E_A = \frac{\delta}{2}$ and $E_B = -\frac{\delta}{2}$ where δ is band separation parameter. For the CPA medium, equation (4.24) reduces to,

$$G_{oo} = \frac{2K}{(K-1)(E-\sigma_o) + (K+1)\sqrt{(E-\sigma_o)^2 - 4KV^2}} ,$$

$$G_{o1} = G_{1o} = G_{oo} \left[\frac{2V}{(E-\sigma_o) + \sqrt{(E-\sigma_o)^2 - 4KV^2}} \right] , \quad (4.25)$$

where σ_0 is the diagonal element of the effective Hamiltonian within CPA. For $K \gg 1$, equations (4.25) reduce to the Green's function of the semicircular model as⁵⁶

$$G_{00} = 2 \left[(E - \sigma_0) - \sqrt{(E - \sigma_0)^2 - 1} \right],$$

$$G_{01} = G_{10} = \frac{1}{2\sqrt{K}} (G_{00})^2. \quad (4.26)$$

The Green's functions within the CCPA can be obtained from equation (4.25) by replacing V by σ_1 , where σ_1 is the off-diagonal element of the effective Hamiltonian.

4.4 COMPARISON OF KKR-CCPA AND TB-CCPA EQUATIONS

In this section, we have compared the KKR-CCPA equations for the s-phase-shift semicircular model of unit resonance half width with the TB-CCPA equations for the semicircular model of unit half band-width. Therefore, we have calculated the values of Green's functions for tight-binding semicircular model with the help of distribution functions. The Green's function within the CPA is given¹ as

$$G_{ij} = \frac{1}{N} \sum_{\vec{q}} \frac{\exp(-i \vec{q} \cdot \vec{R}_{ij})}{E - \sigma_0 - S_{\vec{q}}}, \quad (4.27)$$

where

$$S_{\vec{q}} = \frac{1}{N} \sum_{i,j} \sum_{\vec{q}} \exp(i\vec{q} \cdot \vec{R}_{ij}) V_{ij}.$$

We get diagonal element of Green's function as

$$G_{00} = - \int f^0(b) (c' + b)^{-1} db ,$$

where

$$f^0(b) = \frac{1}{N} \sum_{\vec{q}} \delta(b - S_{\vec{q}}).$$

Similarly off-diagonal elements will be

$$G_{01} = G_{10} = \int f'(b) (c' + b)^{-1} db ,$$

where

$$f'(b) = \frac{1}{N} \sum_{\vec{q}} \exp(-i\vec{q} \cdot \vec{R}_{01}) \delta(b - S_{\vec{q}}).$$

With the help of distribution functions $f^0(b)$ and $f'(b)$ as defined in equations (4.6) and (4.9), we get diagonal and off-diagonal elements of Green's function as⁵²

$$G_{00} = - \int f^0(b) (c' + b)^{-1} db = - 2[c' + (c'^2 - 1)^{1/2}] , \quad (4.28)$$

$$G_{01} = G_{10} = \int f'(b) (c' + b)^{-1} db = - \frac{\lambda}{8} (G_{00})^2 , \quad (4.29)$$

where,

$$c' = \sigma_0 - E .$$

These equations for G_{oo} and G_{o1} are analogous to the equations (4.26) which are exact and are derived by taking the large K limit of the Bethe lattice model. Since T_{ij} in equation (4.4) and G_{ij} in equation (4.27) are structurally similar, we expect T_{oo} and T_{o1} in equations (4.7) and (4.10a) respectively to have the form of equations (4.28) and (4.29). This is exactly what we get by using the distribution functions $f^o(b)$ and $f'(b)$. Therefore, we are justified in using these distribution functions. We also get

$$V_{o1} = V_{1o} = \int f'(b) b db = -\frac{\lambda}{8} . \quad (4.30)$$

The Green's function for the effective medium is given by

$$G_{ij}^{eff} = \frac{1}{N} \sum_{\vec{q}} \frac{\exp(-i\vec{q} \cdot \vec{R}_{ij})}{E - \sigma_o - \tilde{S}_{\vec{q}}} , \quad (4.31a)$$

where

$$\tilde{S}_{\vec{q}} = S_{\vec{q}} + s_{\vec{q}} ,$$

$$s_{\vec{q}} = v_{o1} \exp(i\vec{q} \cdot \vec{R}_{1j}) , \quad (4.31b)$$

$$v_{ij} = \sigma_{ij} - V_{ij} .$$

By using the distribution functions $f^o(b)$ and $f'(b)$, we have calculated the diagonal and off-diagonal elements of G^{eff} as⁵²

$$G_{00}^{eff} = G_{00} - \lambda v_{01} \left[2 c' + \frac{2c'^2 - 1}{(c'^2 - 1)^{1/2}} \right] ,$$

$$G_{01}^{eff} = G_{01} - 2 v_{01} \left[1 + \frac{c'}{(c'^2 - 1)^{1/2}} \right] .$$

Now for convenience, we define a new set of KKR variables as follows⁵²:

$$\begin{aligned} \beta'_{01} &= \beta_{01}/\kappa & , & \quad j_0 = \xi'_{00}/\kappa + 1, \\ j_1 &= \xi'_{01}/\kappa & , & \quad v' = \gamma'_{01}/\kappa , \\ r_1 &= R'_1/\kappa & , & \quad r_2 = R'_2/\kappa , \\ r_3 &= R'_3/\kappa & , & \quad r_4 = R'_4/\kappa , \\ r_5 &= R'_5/\kappa & , & \quad r_6 = R'_6/\kappa , \\ Q''_{\sigma 1} &= \kappa Q'_{\sigma 1} & , & \quad Q''_{\sigma 1} = Q''_{1\sigma} , \\ w &= W'/\kappa \end{aligned} \tag{4.32}$$

By using these variables, the KKR-CCPA equations are compared with TB-CCPA equations in Table 4.1. It is clear that there is a one-to-one correspondence between them.

4.5 RESULTS AND DISCUSSION

We have applied the KKR-CPA and KKR-CCPA theory to the s-phase-shift semicircular model. The change in density of states (δ DOS) with respect to the free electron-gas, has been calculated using these theories for this model. We have also

TABLE 4.1 COMPARISON BETWEEN KKR-CCPA AND TB-CCPA EQUATIONS

KKR-CCPA EQUATIONS	TB-CCPA EQUATIONS
$\beta'_{01} = -\frac{\lambda}{8}$	$V_{01} = -\frac{\lambda}{8}$
$w = \sqrt{\langle xy \rangle} (E_A - E_B)$	$W = \sqrt{\langle xy \rangle} (E_A - E_B)$
$\bar{c} = x E_A + y E_B - E$	$\bar{E} = x E_A + y E_B$
$\tilde{c} = y E_A + x E_B - E$	$\tilde{E} = y E_A + x E_B$
$g_{00}^{eff} = 2 [c + (c^2 - 1)^{1/2}]$ $+ \lambda \beta_{01} \left[2c + \frac{2c^2 - 1}{(c^2 - 1)^{1/2}} \right]$	$G_{00}^{eff} = -2[(c') + (c'^2 - 1)^{1/2}]$ $- \lambda V_{01} \left[2c' + \frac{2c'^2 - 1}{(c'^2 - 1)^{1/2}} \right]$
$g_{01}^{eff} = \frac{\lambda}{2} [2c^2 - 1 + 2c(c^2 - 1)^{1/2}]$ $+ 2\beta_{01} \left[1 + \frac{c}{(c^2 - 1)^{1/2}} \right]$	$G_{01}^{eff} = -\frac{\lambda}{2} [2c'^2 - 1 + 2c'(c'^2 - 1)^{1/2}]$ $- 2V_{01} \left[1 + \frac{c'}{(c'^2 - 1)^{1/2}} \right]$
$j_0 = -c + g_{00}^{eff} [(g_{00}^{eff})^2 - (g_{01}^{eff})^2]^{-1}$	$\xi_{00} = -c' - G_{00}^{eff} [(G_{00}^{eff})^2 - (G_{01}^{eff})^2]^{-1}$
$j_1 = -\beta'_{01} + g_{01}^{eff} [(g_{00}^{eff})^2 - (g_{01}^{eff})^2]^{-1}$	$\xi_{01} = -V_{01} - G_{01}^{eff} [(G_{00}^{eff})^2 - (G_{01}^{eff})^2]^{-1}$
$v' = \beta'_{01} + j_1$	$\gamma_1 = V_{01} + \xi_{01}$
$r_1 = -\tilde{c} - j_0$	$R_1 = E - \tilde{E} - \xi_{00}$
$r_2 = -\bar{c} - j_0 - (v')^2 (r_1)^{-1}$	$R_2 = E - \bar{E} - \xi_{00} - (\gamma_1)^2 (R_1)^{-1}$
$r_3 = -\tilde{c} - j_0 - (w)^2 (r_2)^{-1}$	$R_3 = E - \tilde{E} - \xi_{00} - (W)^2 (R_2)^{-1}$
$r_4 = -\tilde{c} - j_0 - (v')^2 (r_3)^{-1}$	$R_4 = E - \tilde{E} - \xi_{00} - (\gamma_1)^2 (R_3)^{-1}$
$r_5 = -\bar{c} - j_0 - (w)^2 (r_4)^{-1}$	$R_5 = E - \bar{E} - \xi_{00} - (W)^2 (R_4)^{-1}$
$r_6 = -\tilde{c} - j_0 - (v')^2 (r_5)^{-1}$	$R_6 = E - \tilde{E} - \xi_{00} - (\gamma_1)^2 (R_5)^{-1}$
$Q_{01}'' = (w^2 v'^3) / (r_1 r_2 r_3 r_4 r_5 r_6)$	$Q_{01} = (W^2 \gamma_1^3) / (R_1 R_2 R_3 R_4 R_5 R_6)$
$c = \bar{c} + (w^2) / r_6$	$\sigma_0 = \bar{E} + (W^2) / R_6$
$\beta'_{01} = \beta'_{01} + w^2 Q_{01}''$	$\sigma_1 = V_{01} + W^2 Q_{01}$
$\delta \rho(E) = \frac{1}{\pi} \text{Im}(g_{00}^{eff})$	$\rho(E) = -\frac{1}{\pi} \text{Im}(G_{00}^{eff})$

calculated density of states within the tight-binding coherent-potential-approximation (TB-CPA) and tight-binding cluster-coherent-potential-approximation (TB-CCPA) for Bethe lattice model for different K , δ and concentration x .

For convenience, we shall first present the calculations using the tight-binding method for the Bethe lattice model with $K=2$. Figure 4.1 shows the CPA and CCPA density of states for $\delta=1$ in the low concentration regime. We note that there is not much difference in the majority band between the CPA and CCPA, in contrast to considerable difference in the impurity band. Two sub-bands appear in the CCPA as compared to one in the CPA. These two sub-bands arise because of correlated scattering from the clusters of two impurities embedded in the effective medium. In the low concentration limit ($x \ll 1$), the impurity pair in the alloy is most likely to be of AA type. The energy levels for the AA impurity pair embedded in pure B are at energies 0.53 and 1.04, as shown by the solid arrows in figure 1. These two levels are close to the shoulder in CCPA density of states at about $E = 0.6$ and the peak at $E = 1.0$ respectively. The peak at about $E = 0.8$ in the CCPA density of states arises due to the single A impurity level which is at $E = 0.83$ and about which the CPA impurity band is centered. Thus, the structures in the CCPA minority band density of states are accounted for by the examination of impurity levels.

Figure 4.2(a) shows the CPA and CCPA density of states for $\delta=1$ for a concentrated alloy ($x=0.5$). We note that although CPA

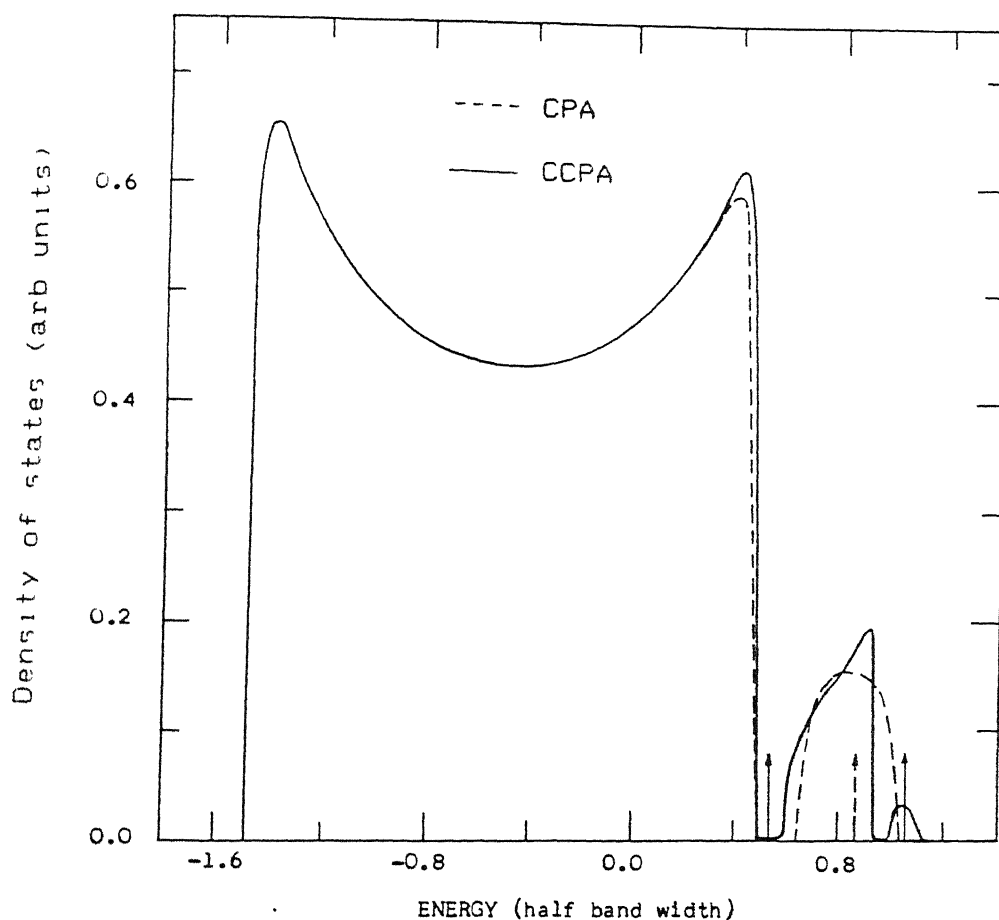


Figure 4.1 The averaged density of states using the CPA (dashed curve) and the CCPA (solid curve) for the parameters $K=2$, $\delta=1$ and $x = 0.05$. Dashed and solid arrows indicate the positions of the single and two impurities levels in a pure B medium. The energy is in units of half-band width.

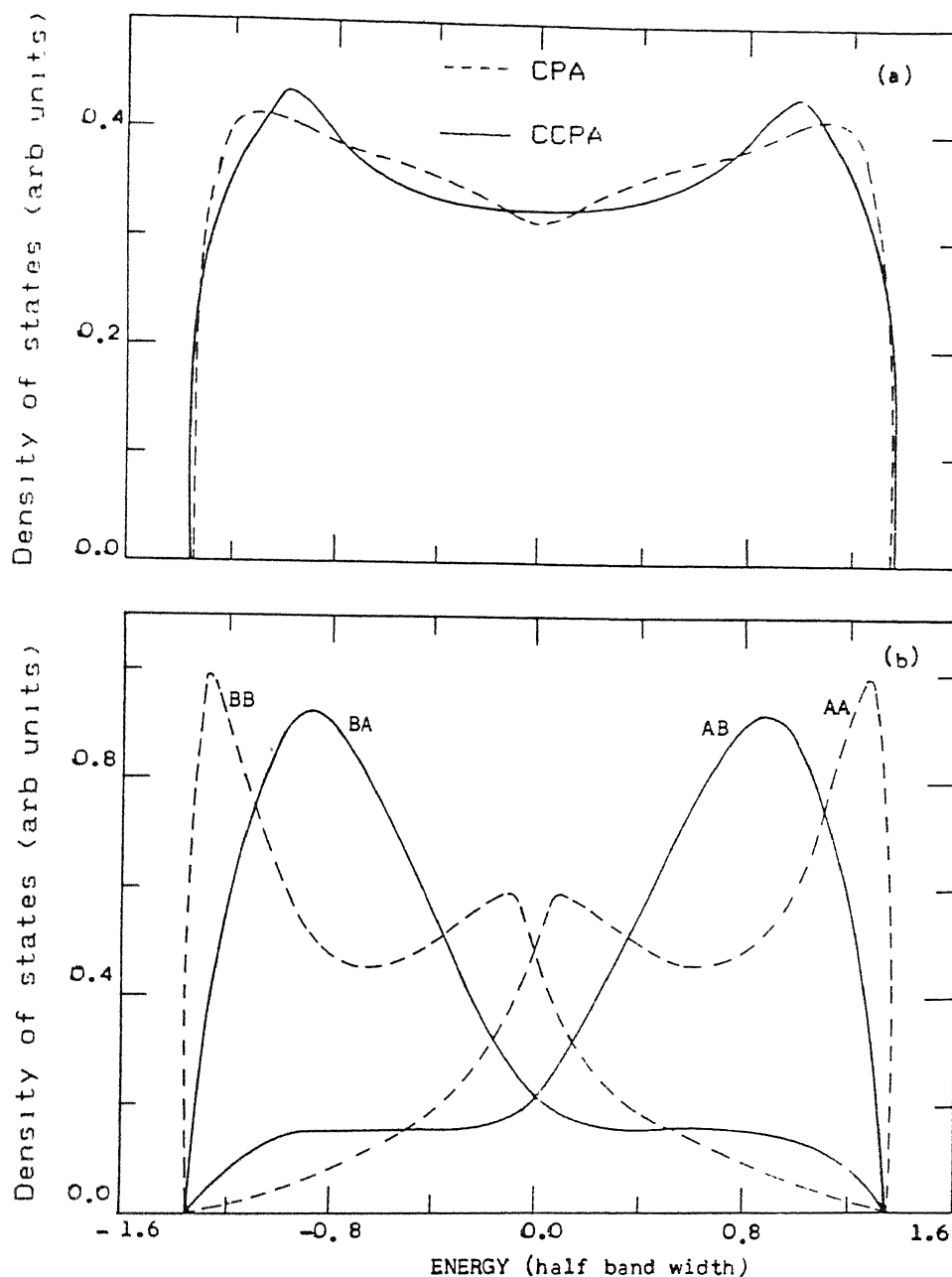


Figure 4.2 (a) The averaged density of states using the CPA (dashed curve) and the CCPA (solid curve) for parameters $K=2$, $\delta=1$ and $x=0.5$. (b) Local density of states for two impurities embedded in the CPA medium for the same parameters. Solid curves correspond to BA and AB pairs while the dashed curves correspond to BB and AA pairs.

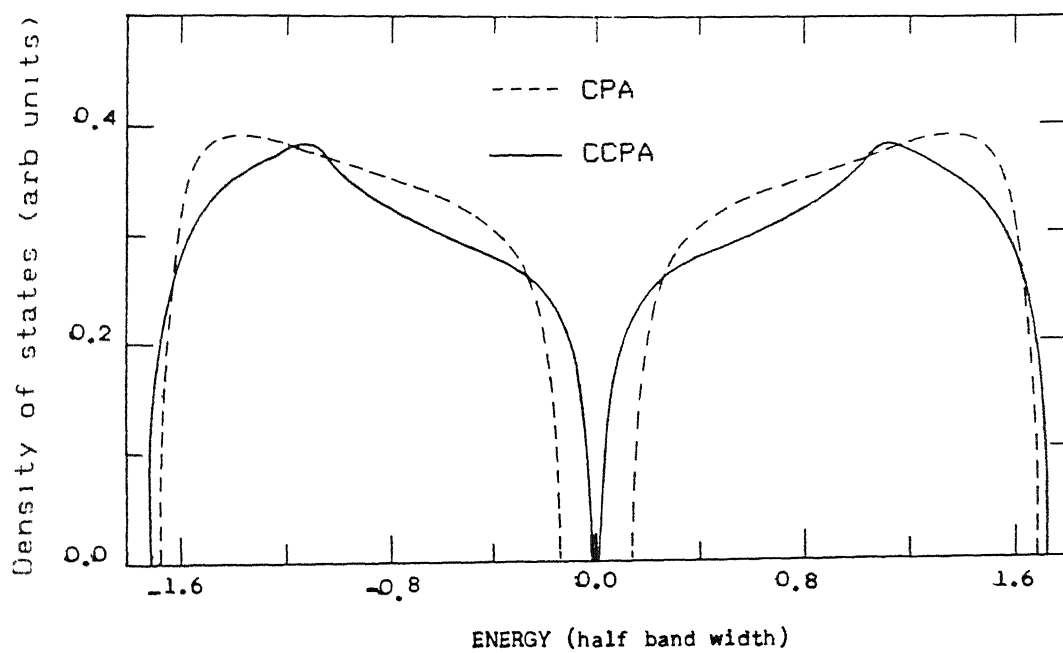


Figure 4.3 The averaged density of states using the CPA (dashed curve) and the CCPA (solid curve) for parameters $K=2$, $\delta=1.7$ and $x=0.5$.

density of states is smooth, the CCPA density of states has two peaks. We explain this on the basis of clusters of two atoms embedded in the effective medium. Unlike the low concentration limit, the probabilities of AA, AB, BA and BB pairs are identical. The peaks in CCPA around $E = -1.0$ and 1.0 appear approximately at energies close to the local density of states peaks corresponding to BA and AB pairs embedded in the CPA medium as shown figure 4.2(b). The local density of states peaks corresponding to AA and BB pairs appear near the edges of CCPA density of states. This indicates that the extra peaks arising in the CCPA density of states are due to the correlated scattering from the impurity clusters in the effective medium.

Figure 4.3 shows the density of states for $\delta=1.7$ and $x=0.5$. We note that critical value of δ for band separation in the CCPA is 1.7 while in CPA it is 1.3 . This implies that in the CCPA, the bands are less likely to be separated.

The results for the Bethe lattice model with $K=10$ are shown in figures 4.4, 4.5(a), 4.5(b) and 4.6. In figure 4.4 we show the CPA and CCPA density of states for $\delta=1$ in the dilute limit ($x=0.05$). There is no difference in the CPA and CCPA density of states in majority band. The CCPA minority band density of states has two peaks at about $E=0.6$ and 0.85 in contrast to a very smooth CPA minority band. The two peaks in the CCPA density of states are well accounted for by the energy

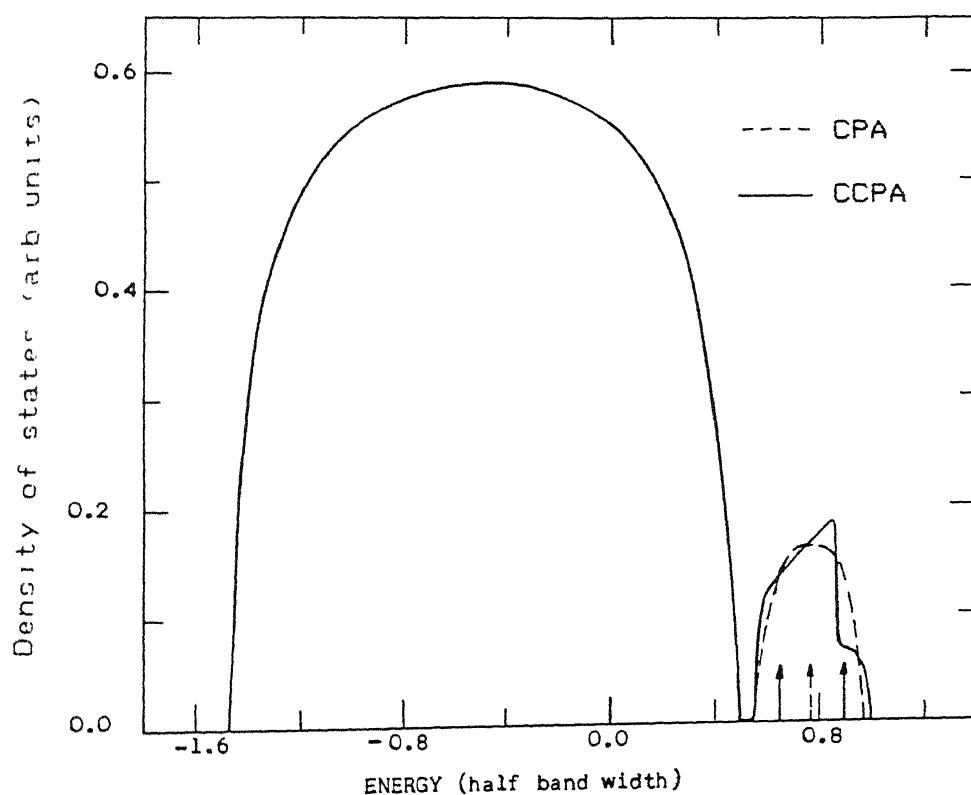


Figure 4.4 The averaged density of states using the CPA (dashed curve) and the CCPA (solid curve) for parameters $k=10$, $\delta=1$ and $x=0.05$. The dashed and solid arrows indicate the positions of the single and two impurities levels in a pure B medium.

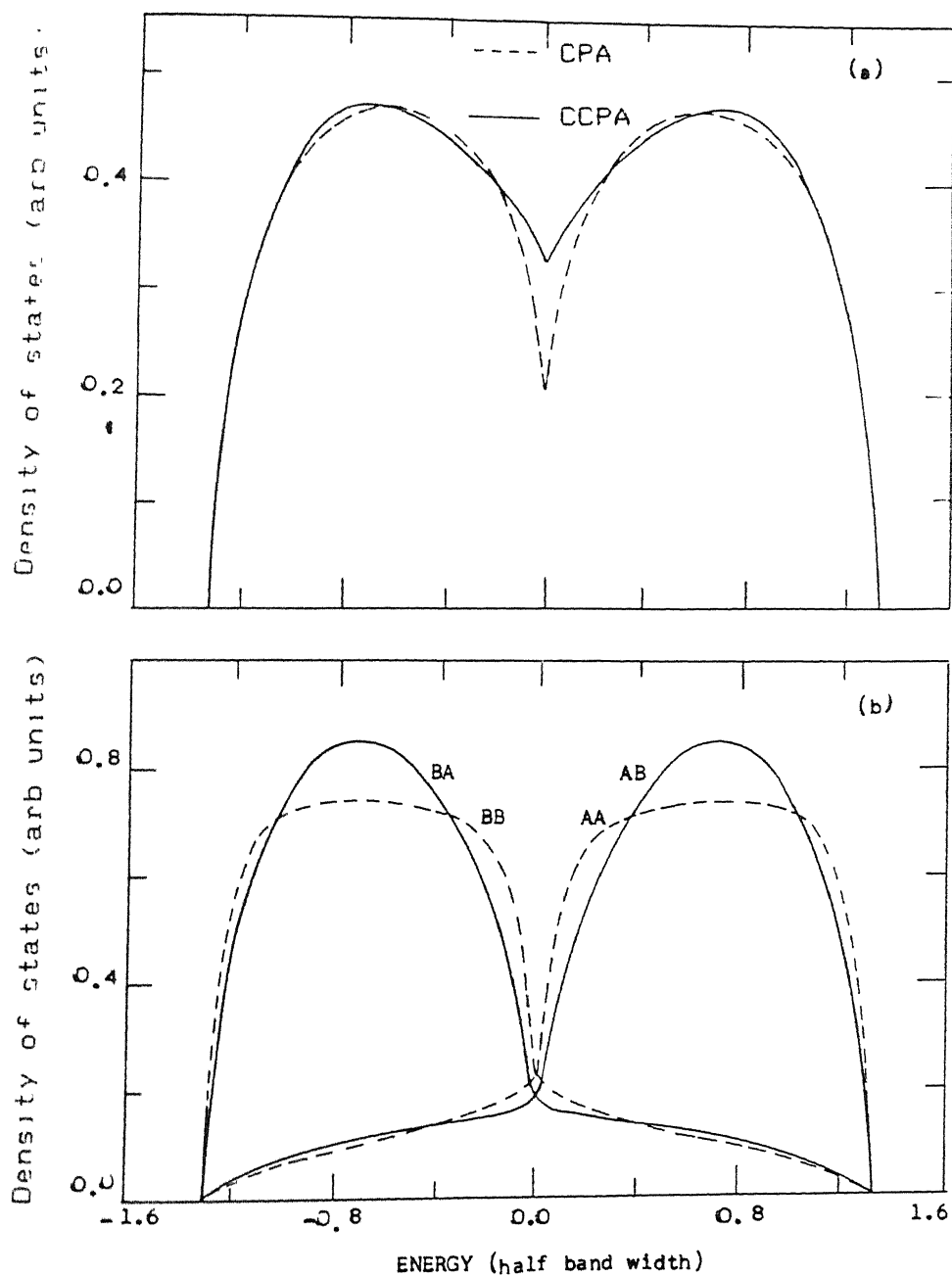


Figure 4.5 (a) The averaged density of states using the CPA (dashed curve) and the CCPA (solid curve) for parameters $K=10$, $\delta=1$ and $x=0.5$. (b) Local density of states for two impurities pairs embedded in the CPA medium for the same parameters. Solid curves correspond to BA and AB pairs while the dashed curves correspond to BB and AA pairs.

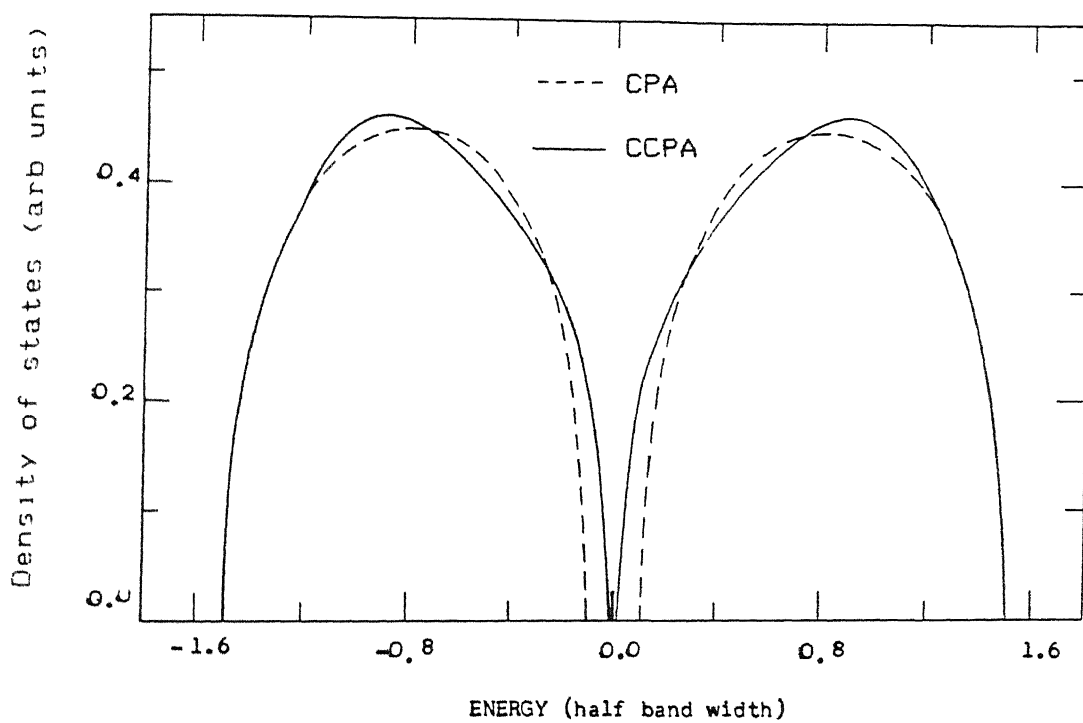


Figure 4.6 The averaged density of states using the CPA (dashed curve) and the CCPA (solid curve) for parameters $\kappa=10$, $\delta=1.4$ and $x=0.5$.

levels of AA impurity pairs which are at $E=0.64$ and 0.87 respectively.

Figure 4.5(a) shows the density of states curves for $\delta=1$ in the concentrated limit ($x=0.5$). We note that both the CPA as well as the CCPA density of states are smooth. This arises due to the following reasons : (i) The local density of states for the impurity pairs, as shown in figure 4.5(b), are smooth as compared to $K=2$. (ii) The local density of states peaks for (BA,AB) and (AB,AA) pairs are at about the same energies.

Figure 4.6 shows the density of states for $\delta=1.4$ and $x=0.5$. This again shows that the critical value of δ in the CCPA is greater than that in the CPA. It is 1.4 in the CCPA where as it is 1.2 in the CPA.

A contrast between $K=2$ and $K=10$ cases is worth noting. In the dilute limit, the minority band for $K=2$ (figure 4.1) breaks up into two sub-bands while for $K=10$ (figure 4.4) we have only one impurity band with some structures. The separation between the two impurity levels for $K=2$ case is much larger than that for $K=10$. This difference is due to the different values of hopping parameter $V = 0.5/\sqrt{K}$, in the two cases. For $K=10$ case it is much smaller compared to that for $K=2$. Thus in the concentrated limit, there is an appreciable difference in the CPA and CCPA density of states for $K=2$ compared to $K=10$ case. The difference between the CPA and CCPA density of states decreases as K increases and eventually

reduces to zero when K is very large (≈ 100). Note that in this limit, our model reduces to the semi-circular model⁵⁶ as shown in section 4.3.

Now we present the KKR-CCPA results for the s-phase-shift semicircular model. We have calculated the change in density of states (δDOS) with respect to the free electron gas within the CPA and CCPA. We have found that for the small λ , there is negligible difference in the δDOS between the CPA and CCPA, as was mentioned above for the Bethe lattice model with large K . This is because for large K (or small λ), CCPA equations for both models have one-to-one correspondence. But for large λ there is a visible difference between the δDOS in the CPA and CCPA as can be seen in figures 4.7(a) and 4.7(b). Figure 4.7(a) shows the change in the density of states (δDOS) using KKR-CPA and KKR-CCPA for same resonance half-widths ($\Gamma_A = \Gamma_B = 1$) while figure 4.7(b) is for different half-widths ($\Gamma_A = 1$, $\Gamma_B = 2$). Note that these results, in general, are also valid for the tight-binding semicircular model as is evident from Table 4.1.

As in the tight-binding case, to understand the structure in the KKR-CCPA density of states, we have to solve the two impurities problem. This requires a knowledge of the impurity wave functions², which are not available for the s-phase shift semicircular model. However, since we have already shown a one-to-one correspondence between the KKR-CCPA and the TB-CCPA

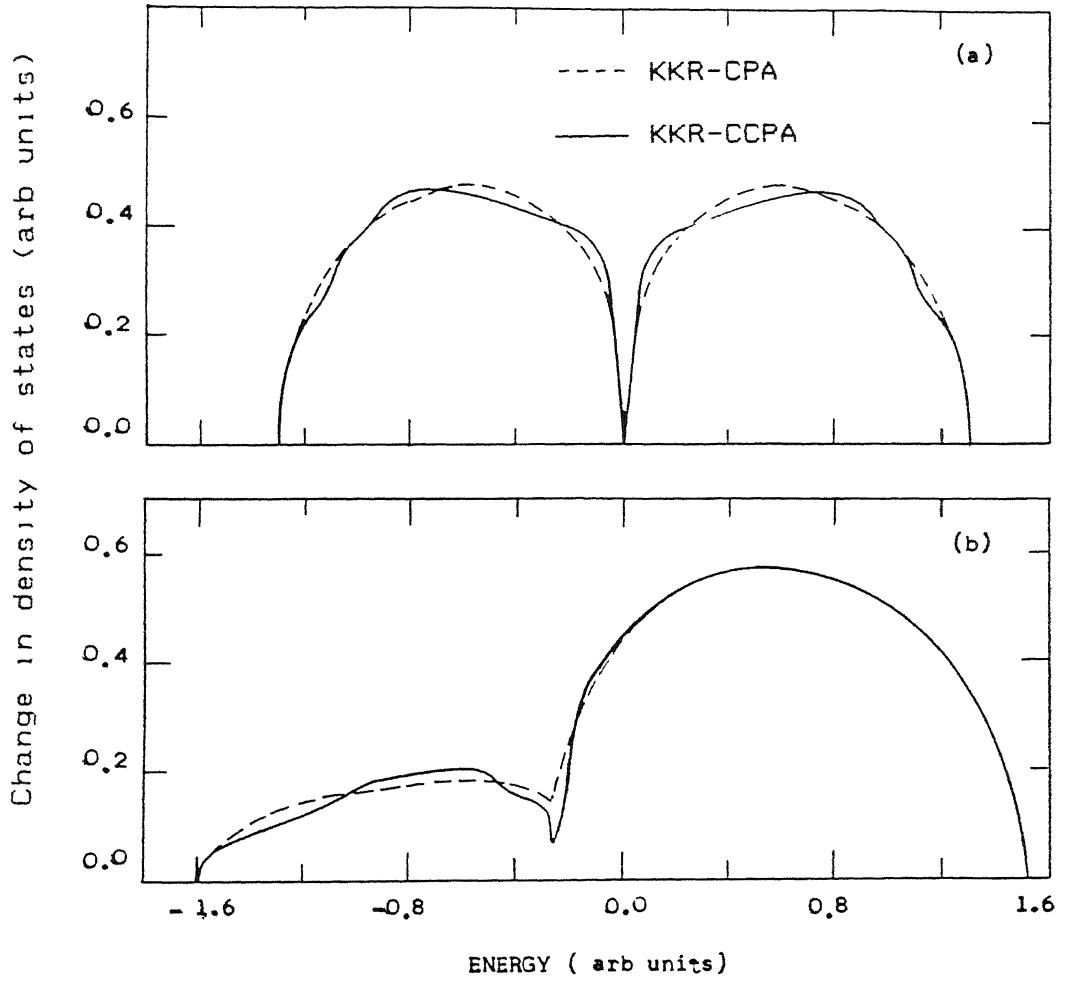


Figure 4.7 (a) The change in averaged density of states per atom using the KKR-CPA (dashed curve) and the KKR-CCPA (solid curve) for the parameters $E_A = -E_B = 0.5$, $\Gamma_A = 1$, $\Gamma_B = 1$, $\lambda = 2.5$ and $x = 0.5$. The energy is in arbitrary unit. (b) Same as in (a) but with parameters $E_A = -E_B = 0.5$, $\Gamma_A = 1$, $\Gamma_B = 2$, $\lambda = 2.5$ and $x = 0.8$.

equations, we expect that the main features of the TB model will be reflected in the KKR model, and hence, the structure in figure 4.7 can be related to the correlated scattering from clusters of atoms.

4.6 CONCLUSIONS

We have applied the KKR-CCPA formulation of chapter 3 to the s-phase-shift semicircular model, which has an analogue in the tight-binding framework. A one-to-one correspondence has been established between the KKR-CCPA equations for this model and the TB-CCPA equations for the analogous semicircular model. The TB-CCPA formulation (described in chapter 3) was then applied to the Bethe lattice model. We found that the difference in the CPA and CCPA density of states is appreciable only when the number of nearest neighbours Z is small and decreases as Z increases. Also, in the CPA, the minority band is smooth whereas in the CCPA it gains structure. The structure in the CCPA density of states is seen at energies close to the impurity levels. This clearly indicates that the structure appears due to the correlated scattering from the clusters embedded in an effective medium. For large value of Z , there is little difference in the CPA and the CCPA density of states for this model and the s-phase-shift semicircular model. This is expected because of their equivalence in this limit.

CHAPTER 5

SUMMARY AND CONCLUSIONS

In this thesis we have discussed and applied two methods for electronic structure calculation of disordered random alloys using muffin-tin potentials. The first method is the charge self-consistent KKR-CPA which treats disorder scattering in the single-site approximation and thus ignores the correlated scattering from clusters of atoms. The second method is the KKR-CCPA which is cluster generalization of the KKR-CPA method. The KKR-CCPA includes the correlated scattering from clusters of atoms, which may be important in systems showing clustering or ordering tendencies such as Cu-Ni, Cu-Pt and Cu-Pd or in magnetic alloys such as Ni-Cu and Fe-Ni in which the magnetic moment of an atom depends on the local environment of the atom.

The charge self-consistent KKR-CPA was applied to Nb-Mo system which is a classic bcc refractory alloy system. We have calculated self-consistent charge densities, self-consistent potentials, component density of states and density of states of Nb_xMo_y alloys for $x=0.25, 0.50$ and 0.75 . It has been found that the maximum difference in the Nb(Mo) valence charge densities in the alloy with respect to the pure Nb(Mo) is of

the order of 10% near the muffin-tin radius. Also, the maximum difference in the Nb(Mo) potentials in the alloy with respect to pure Nb(Mo) is of the order of 5% near the muffin-tin radius. These differences decrease with increasing concentration of Nb(Mo) in the alloy. A comparison of the results of the charge self-consistent KKR-CPA and Nb-based rigid band model shows that the charge self-consistent KKR-CPA density of states deviates from the rigid band model density of states in some energy range. We also found that there is an appreciable difference between the density of states calculated by using the charge self-consistent KKR-CPA method and non-charge self-consistent KKR-CPA methods^{35,36}. This shows that the density of states is very sensitive to the constituent potentials. We have found that charge self-consistent KKR-CPA density of states at Fermi energy (E_F) for different concentrations of alloys is in good agreement with the experimental results obtained by the analysis of specific heat data. We have also compared the results of component density of states calculated by using the charge self-consistent KKR-CPA method with the results of soft X-ray (emission and absorption) spectra for Nb_{0.5}Mo_{0.5} alloy. We have found that there is a good agreement between our results and experimental results. These results underline the importance of charge self-consistency in the KKR-CPA theory.

The KKR-CPA calculation can be improved by going beyond the single-site approximation and using the KKR-CCPA which has been formulated by us. In this formulation we have used the augmented space formalism which guarantees the herglotz properties of the averaged Green's function. The KKR-CCPA equations were derived by first noting a formal similarity between the multiple scattering equations of KKR theory and Green's function of tight-binding Hamiltonian. Therefore, we have first developed the tight-binding cluster-coherent-potential-approximation (TB-CCPA) formulation. We were able to refine the TB-CCPA method such that various quantities which were hitherto being calculated approximately are calculated exactly. In the tight-binding framework, we have formulated the two-impurity problem to calculate the local density of states on an impurity of two-impurity cluster. The KKR-CCPA equations were then derived by using the correspondence between the variables of KKR framework and tight-binding framework.

The KKR-CCPA theory was applied to the s-phase shift semicircular model, which has its analogue in the tight-binding semicircular model. We have compared the KKR-CCPA equations for the s-phase shift semicircular model and the TB-CCPA equations for the tight-binding semicircular model and a one-to-one correspondence between them has been established. We have also applied the TB-CCPA method to the Bethe lattice model. We have found that the difference in the TB-CPA density of states and

the TB-CCPA density of states is appreciable only when the number of nearest neighbours (Z) is small and decreases as Z increases. The minority band in the TB-CPA density of states is smooth and it gains structure in the TB-CCPA. The structure in the TB-CCPA density of states is seen at energies close to the two-impurity levels. This clearly indicates that the structure appears due to the correlated scattering from the clusters of atoms in the effective medium. For large Z , there is little difference in the coherent-potential-approximation density of states and the cluster-coherent-potential-approximation density of states for this model as well as the s -phase shift semicircular model. This is because for large Z the Bethe lattice model reduces in the semicircular model as shown in section 4.3.

In this work, we have applied the KKR-CCPA theory for two-atom clusters to a model case. The fully self-consistent KKR-CCPA theory has been developed by Razee et al.⁵³ in Green's function formalism. This theory can be applied to realistic alloy systems by taking 9-atom (bcc) and 13-atom (fcc) clusters. The short-range-order can also be treated within this theory and charge self-consistency can be obtained. Such calculations are in progress in our group.

The KKR-CPA calculation can be improved in many other ways. One should improve upon the local density approximation which we had used in our calculation. At present many workers

are engaged in this direction and have suggested various approximation such as gradient correction, GW approximation, weighted density (WD) approximation, and self-interaction corrected (SIC) approximation etc.^{15,57}. We feel that such approximations should be first tried and thoroughly tested on simple systems and pure metals before these could be applied to disordered alloys. The relativistic version of the KKR-CPA theory has been formulated by Staunton et al.⁵⁸ and can be used to improve our KKR-CPA results. However, such corrections in case of Nb-Mo alloys are supposed to be quite small. The other direction in which the theory for disordered alloys can be improved is by going beyond the muffin-tin approximation. The KKR-band theory for pure metals has been generalized to non-muffin-tin potentials by Brown and Ciftan⁵⁹, Gonis⁶⁰ and Faulkner⁶¹. However, their methods have convergence problems as discussed by Gonis and Faulkner. To our knowledge the KKR-CPA theory has not been formulated for non-muffin-tin potentials so far and is still an open problem.

REFERENCES

1. H. Ehrenreich and L. M. Schwartz, Solid State Physics 31, (1976).
2. J. S. Faulkner in Progress in Materials Science, ed. by T. Massalski (Pergamon, New York, 1982) vol. 27 ; J. S. Faulkner and G. M. Stocks, Phys. Rev. B21, 3222 (1980).
3. A. Bansil, Electronic Band Structure and its Applications, ed. M Yussouff, (Springer-Verlag, Berlin, 1987), p 273.
4. L. Nordheim, Ann. Phys. (Leipzig) 9, 607 and 641 (1931);
F. Bassani and D. Brust, Phys. Rev. 131, 1524 (1963);
H. Amar, K. H. Johnson, and C. B. Sommers, Phys. Rev., 153, 655 (1967); M. M. Pant and S. K. Joshi, Phys. Rev., 184, 635 (1969).
5. N. F. Mott and H. Jones, The Theory of the Properties of Metals and Alloys (Clarendon, Oxford, 1936);
J. Friedel, Nuovo Cimento suppl. 7, 287 (1958).
6. T. L. Loucks, Augmented Plane Wave Method, (Benjamin, New York, 1967).
7. V. L. Moruzzi, J. F. Janak and A. R. Williams, Calculated Electronic Properties of Metals (Pergamon, New York, 1978).
8. A. Bansil, L. M. Schwartz and H. Ehrenreich, Phys. Rev. B12, 2893 (1975).
9. A. Bansil, H. Ehrenreich, L. M. Schwartz and R. E. Watson, Phys. Rev. B9, 445 (1974).
10. H. Asonen, M. Lindroos, M. Pessa, R. Prasad, R. S. Rao, and A. Bansil, Phys. Rev. B25, 7075 (1982).
11. R. Prasad and A. Bansil, Phys. Rev. Letters, 48, 113 (1982).
12. R. S. Rao, A. Bansil, H. Asonen and M. Pessa, Phys. Rev. B29, 1713 (1984).
13. R. Prasad, S. C. Papadopoulos and A. Bansil, Phys. Rev. B23 2607 (1981).

14. R. Prasad, R. S. Rao and A. Bansil, in *Excitations in Disordered Systems*, ed. M. P. Thorpe (Plenum, New York, 1982).
15. P. Hohenberg and W. Kohn, *Phys. Rev.* 136, B 864 (1964).
S. Lundqvist and N. H. March, *Theory of the Inhomogeneous Electron Gas*, (Plenum, New York, 1983).; J. Callaway and N. H. March, *Solid State Physics*, 38, 135 (1984).
16. U. von Barth and L. Hedin, *J. Phys. C: Solid State Phys.* 5, 1629 (1972).
17. O. Gunnarsson and B. L. Lundqvist, *Phys. Rev.* B13, 4274 (1976).
18. S. H. Vosko and L. Wilk, *Phys. Rev. B* 22, 3812 (1980);
S. H. Vosko, L. Wilk and M. Nusair, *Can. J. Phys.* 58, 1200 (1980).
19. H. Wright, P. Weightman, P. T. Andrews, W. Folkerts, C. F. J. Elipse, G. A. Sawatzky, D. Norman and H. Padmore, *Phys. Rev.* B35, 519 (1987).
20. N. Stefanou, R. Zeller and P. H. Dederichs, *Solid State Commun.* 62, 735 (1987).
21. J. Banhart, W. Pfeiler and J. Voitlander, *Phys. Rev* B37, 6027 (1988).
22. R. Mills and P. Ratanavararaksa, *Phys. Rev.* B18, 5291 (1978).
23. A. Mookerjee, *J. Phys. C: Solid State Physics*, 6, L205, 1340 (1973).
24. L. J. Gray and T. Kaplan, *Phys. Rev.* B14, 3462 (1976);
L. J. Gray and T. Kaplan, *J. Phys. C: Solid State Physics* 9, L303, L483 (1976).
25. P. Soven, *Phys. Rev* B2, 4715 (1970).
26. S. S. Rajput, R. Prasad and A. Bansil (unpublished).
27. W. L. McMillan, *Phys. Rev.* 167, 331 (1968).
28. P. C. de Camargo, F. R. Brotzen and S. Steinemann, *J. Phys. F: Met. Phys.* 17, 1065 (1987).

29. E. S. Black, D. W. Lynch and C. G. Olson, Phys. Rev. B16, 2337 (1977).
30. E. Colavita, A. Franciosi, R. Rosei, and F. Sacchetti, Phys. Rev. B20, 4864 (1979).
31. C. R. Bull, J. H. Kaiser, A. Alam, N. Shiotani and R. N. West, Phys. Rev. B29, 6378 (1984).
32. J. H. Kaiser, P. A. Walters, C. R. Bull, A. Alam, R. N. West and N. Shiotani, J. Phys. F: Met. Phys. 17, 1243 (1987).
33. C. Colinet, A. Bessoud and A. Pasturel, J. Phys. F: Met. Phys. 18, 903 (1988).
34. V. Hadjicontis, C. Varotsos and K. Eftaxias, J. Phys. F: Met. Phys. 18, 1113 (1988).
35. E. S. Giuliano, R. Ruggeri, B. L. Gyorffy and G. M. Stocks, in Transition Metals, ed. M. J. G. Lee, J. M. Pertz and E. Fawcett, Institute of Physics Bristol and London, (1977), p 40.
36. E. Donato, E. S. Giuliano, R. Ruggeri and A. Stancanelli, Phys. Stat. Sol. (b) 95, K37 (1979).
37. $[B_q(x)]_{LL'} = A_{LL'} + i \times \delta_{LL'}$, where $A_{LL'}$ is the well-known structure function of band theory.
38. S. Kaprzyk and A. Bansil (unpublished).
39. H. Winter and G. M. Stocks, Phys. Rev. B27, 882 (1983);
G. Ries and H. Winter, J. Phys. F: Met. Phys. 9, 1589 (1979)
40. E. Donato, B. Ginatempo, E. S. Giuliano, R. Ruggeri and A. Stancanelli, Phys. Stat. Sol. (b) 110, 39 (1982).
41. R. Prasad and A. Bansil, Phys. Rev. B21, 496 (1980).
42. S. Kaprzyk and P. E. Mijnarends J. Phys. C: Solid State Phys. 19, 1283 (1986); S. Kaprzyk and A. Bansil (unpublished).
43. D. D. Johnson, F. J. Pinski and G. M. Stocks, Phys. Rev. B30, 5508 (1984).
44. R. Zeller, J. Dentz and P. A. Dederichs, Solid State Commun. 44, 993 (1982).
45. H. Akai and P. H. Dederichs, J. Phys. C: Solid State Physics 18, 2455 (1985).

46. A. Gonis , G. M. Stocks, W. H. Butler and H. Winter, Phys. Rev. B29, 555 (1984).
47. A. Mookerjee, J. Phys. C: Solid State Physics, 9, 1225 (1976); J. Phys. C: Solid State Phys. 19, 193, 275 (1986).
48. S. S. A. Razee, A. Mookerjee and R. Prasad (unpublished).
49. V. Kumar, A. Mookerjee and V. K. Srivastava, J. Phys. C: Solid State Physics, 15, 1939 (1982).
50. P. K. Thakur, A. Mookerjee and V. A. Singh, J. Phys. C: Solid State Physics, 17, 1523 (1987).
51. A. Mookerjee, J. Phys. F: Met. Phys., 17, 1511 (1987).
52. S. S. Rajput, S. S. A. Razee, R. Prasad and A. Mookerjee, J. Phys.: Condens. Matter 2, 2653 (1990).
53. S. S. A. Razee, S. S. Rajput, R. Prasad and A. Mookerjee, (unpublished).
54. A. Mookerjee and S. Bardhan, J. Phys.: Condens. Matter 1, 509 (1989); S. Bardhan and A. Mookerjee (unpublished); A. Mookerjee, Electronic Band Structure and its Applications, ed. M Yussouff (Springer-Verlag, Berlin, 1987), p 249.
55. E. N. Economou, Green's Function in Quantum Mechanics, (Springer-Verlag, Berlin, 1979), p 90.
56. B. Velicky, S. Kirkpatrick and H. Ehrenreich, Phys. Rev. 175, 747 (1968).
57. R. W. Godby, M. Schluter and L. J. Sham, Phys. Rev. B37, 10159 (1988); R. W. Godby and R. J. Needs, Phys. Rev. Letters, 62, 1169 (1989); R. O. Jones and O. Gunnarsson, Rev. of Modern Phys., 61, 689 (1989).
58. J. Staunton, B.L. Gyorffy and P. Weinberger, J. Phys. F: Met. Phys. 10, 2665 (1980).
59. R. G. Brown and M. Ciftan, Phys. Rev. B27, 4564 (1983); R. G. Brown and M. Ciftan, Phys. Rev. B33, 7937 (1986).
60. A. Gonis, Phys. Rev. B33, 5914 (1986).
61. J. S. Faulkner, Phys. Rev. B34, 5931 (1986); J. S. Faulkner Phys. Rev. B32, 1339 (1985).

PHY-1990-D-RAD-ELE